



Solid State Quantum Optics with a Quantum Dot in a Nano-Photonic Cavity

Catherine Louise Phillips

A thesis presented for the degree of
Doctor of Philosophy

Department of Physics and Astronomy
University of Sheffield

August 2020

Abstract

This thesis describes the first and second-order correlation measurements that were performed on a III-V self-assembled quantum dot weakly coupled to a H1 nanophotonic crystal cavity. The system has an exceptionally large Purcell factor, which enables new regimes of light-matter coupling to be explored. In particular, the Purcell effect enhances the radiative recombination rate by an unprecedented factor, allowing measurements to take advantage of the fast lifetime and broad, transform-limited linewidth of the excitons excited in the quantum dot. The main results of this thesis are presented in three chapters, which explore, respectively, the application of the system as a single-photon source, the interactions between the quantum dot excitons and their solid-state environment, and the effect of spectral filtering on resonance fluorescence photon statistics. None of these experiments would have been possible without the very large Purcell enhancement of the radiative emission from the quantum dot.

In the first set of experiments, the emission properties of the cavity-coupled quantum dot under π -pulsed resonant excitation were investigated. Hanbury Brown and Twiss second-order correlation measurements were used to measure the single-photon purity of the quantum dot emission. Hong-Ou-Mandel measurements were performed to investigate the indistinguishability of the single-photons produced.

The emission from the cavity-coupled dot was then investigated under continuous wave excitation. In the second set of experiments, first-order correlation measure-

Abstract

ments were made in conjunction with spectroscopic measurements to investigate the phonon sideband properties of the quantum dot, both under resonant and slightly detuned excitation.

In the final set of measurements, spectral filtering was used to alter the photon statistics observed when measuring the resonance fluorescence from the cavity-coupled quantum dot. Here, the effect of filtering in both the weak and strong driving regimes was investigated by filtering both above and below the linewidth of the quantum dot.

Acknowledgements

I would like to thank the many people of the LDS group at Sheffield who have helped me during the course of my PhD. In particular, my supervisor Mark Fox for his guidance and encouragement and Alistair Brash for being my lab hero and go-to question answerer with his encyclopedic paper knowledge. Also within LDS I would like to thank Ian Griffiths, Sam Sheldon and Andrew Foster for keeping me both happy and sane with their fun and interesting company. Thanks also go to Ed Clarke, Ben Royall and Rikki Coles for their sample growth, fabrication and optimisation, without which this thesis would not have been possible.

Outside of LDS I would like to thank our theory collaborators: Jake Iles-Smith, Dara McCutcheon and Ahsan Nazir, for adding mathematical understanding to our experiment results. Thanks also to Matt Mears, for putting up with me appearing at his office door since undergrad.

I would also like to thank my friends, especially Dave Brown and Lisa Alhadeff, for plentiful coffee, conversation and cake. Thanks must also go to my family, for their endless encouragement and optimism over many years.

Publications

Some of the results and figures presented here have appeared in the following publications:

A. Brash, F. Liu, J. O'Hara, L. M. P. P. Martins, R. J. Coles, **C. L. Phillips**, B. Royall, C. Bentham, I. Itskevich, L. R. Wilson, M. S. Skolnick, and A. M. Fox, "Bright and Coherent On-Chip Single Photons from a Very High Purcell Factor Photonic Crystal Cavity," in Conference on Lasers and Electro-Optics, OSA Technical Digest (Optical Society of America, 2017), paper FTu4E.5.

F. Liu, A. J. Brash, J. O'Hara, L. M. P. P. Martins, **C. L. Phillips**, R. J. Coles, B. Royall, E. Clarke, C. Bentham, N. Prtljaga, I. E. Itskevich, L. R. Wilson, M. S. Skolnick and A. M. Fox. "High Purcell factor generation of indistinguishable on-chip single photons." *Nature Nanotechnology* **13**, 835-840 (2018).

A. J. Brash, J. Iles-Smith, **C. L. Phillips**, D. P. S. McCutcheon, J. O'Hara, E. Clarke, B. Royall, L. R. Wilson, J. Mørk, M. S. Skolnick, A. M. Fox, and A. Nazir. "Light Scattering from Solid-State Quantum Emitters: Beyond the Atomic Picture." *Physical Review Letters* **123**, 167403 (2019).

A. J. Brash, J. Iles-Smith, **C. L. Phillips**, J. O'Hara, B. Royall, L. R. Wilson, M. S. Skolnick, A. M. Fox, D. P. S. McCutcheon, E. Clarke, J. Mørk, and A. Nazir, "Coherent scattering from quantum dots: beyond the atomic picture," in Conference

Publications

on Lasers and Electro-Optics, OSA Technical Digest (Optical Society of America, 2020), paper FW3C.5.

C. L. Phillips, A. J. Brash, D. P. S. McCutcheon, J. Iles-Smith, E. Clarke, B. Royall, M. S. Skolnick, A. M. Fox, and A. Nazir. "Photon Statistics of Filtered Resonance Fluorescence." *Physical Review Letters* **125**, 043603 (2020).

Contents

Abstract	iii
Acknowledgements	v
Publications	vii
1 Introduction	1
1.1 Motivation	1
1.2 Outline of this work	2
2 Background	5
2.1 Single Photon Sources	5
2.2 Quantum Dots	6
2.2.1 Quantum Wells, Wires and Dots	6
2.2.2 Self Assembled Quantum Dots	8
2.2.3 Electronic Structure of QD	11
2.3 QDs in Applied External Fields	16
2.3.1 Quantum-Confined Stark Effect	16
2.3.2 Optical Stark Effect	18
2.4 Interactions	20
2.4.1 Dephasing	20
2.4.2 Phonons	21
2.5 Cavities	23
2.5.1 Theory	23
	ix

Contents

2.5.2	Weak Coupling	25
2.5.3	Strong Coupling	26
2.5.4	Photonic Crystal Cavities and Waveguides	26
2.5.5	Other Types of Cavities	33
3	Experimental Methods	37
3.1	Introduction	37
3.2	Optical Table	38
3.3	Cryostat	39
3.4	Resonance Fluorescence	41
3.5	Excitation Lasers	43
3.5.1	Power Control	43
3.5.2	Pulsed: Coherent Mira 900F	44
3.5.3	CW: Toptica DL Pro	45
3.5.4	CW: M-Squared SOLSTIS	45
3.5.5	CW: Thorlabs LP808-SA60	45
3.5.6	Pulse Shaping	46
3.6	Detection Systems	48
3.7	Calibrating Excitation Power	50
3.7.1	Pulsed Pi power	51
3.7.2	CW Pi Power	54
4	Sample	57
4.1	Wafer	57
4.2	Design	59
4.3	Characterisation	61
5	Cavity-Coupled QD as a Single-Photon Source	67
5.1	Introduction	67
5.2	Second-Order Correlation Measurements	68
5.2.1	Hanbury Brown and Twiss	69

5.2.2	Hong-Ou-Mandel	72
5.3	Experiments	79
5.3.1	Method: Hanbury Brown and Twiss	79
5.3.2	Results: Hanbury Brown and Twiss	81
5.3.3	Method: Hong-Ou-Mandel	82
5.3.4	Results: Hong-Ou-Mandel	84
5.4	Conclusion	93
6	Phonon Effects on QD Emission	95
6.1	Introduction	95
6.2	Coherent Scattering	96
6.3	First-Order Correlation Measurements	101
6.3.1	Experimental Method	101
6.3.2	Results and Theory	105
6.4	Effect of Excitation Power on the Phonon Sideband	111
6.4.1	Experimental Method	111
6.4.2	Results and Theory	113
6.5	Phonon Effects in Detuned Coherent Scattering	115
6.5.1	Experimental Method	116
6.5.2	Results and Theory	117
6.6	Conclusion	124
7	Spectral Filtering Effects on QD Resonance Fluorescence	127
7.1	Introduction	127
7.2	Filtering QD emission	128
7.3	Weak Driving Regime	136
7.3.1	Experimental Method	138
7.3.2	Results and Theory	138
7.4	Strong Driving - Mollow Triplet Regime	145
7.4.1	Power Dependence at $\Gamma = 0.29\gamma$	147

Contents

7.4.2	Filter Bandwidth Dependence at $\Omega_R = 2\gamma$	150
7.5	Conclusion	153
8	Summary and Future Work	157
8.1	Summary	157
8.1.1	Cavity Coupled QD as a Single-Photon Source	157
8.1.2	Phonon Effects on QD Emission	158
8.1.3	Spectral Filtering Effects on QD Resonance Fluorescence	158
8.2	Future Work for the QD in a H1 Cavity	159
8.2.1	Improving the Excitation Pulse Shaping	159
8.2.2	Improving the H1 PhCC Sample	162
8.2.3	Homodyne Scheme for Measuring Antibunching and a Sub-natural Linewidth	163
8.3	Future Work - Related Areas	164
8.3.1	Telecom C-Band QDs	164
8.3.2	QD Spin in a Cavity for Photonic Cluster State Generation	165
8.3.3	QD Registration	166
	Acronyms	169

1 Introduction

1.1 Motivation

Optical quantum technologies use the quantum states of light to process and transmit information through the manipulation of quantum bits (qubits). Research into optical quantum technologies mainly falls into three categories: quantum communication [1, 2], quantum computation [3–5] and quantum metrology [6, 7]. The production of single-photon states of light are used as a building block in all three areas.

Quantum communication is the transfer of information between two parties using the quantum properties of light. This can be extended to quantum cryptography which uses the principles of quantum measurement, for example the no-cloning theorem that prevents the cloning of arbitrary unknown quantum states [8], to enable secure communication and detect the presence of eavesdroppers [1]. Control over the number of photons within the communication pulses is required for quantum cryptography, with single-photon Fock states being the basis on which many protocols are designed [1].

Quantum computers use qubits to perform operations. Quantum computing systems are designed to out-perform classical computing systems for solving certain mathematical problems [9–11] and for simulating quantum systems [3, 12]. For a system to have a quantum computing architecture it must meet the DiVincenzo criteria [13]. Single-photons are a possible source of qubits as they are easy to manipulate and allow encoding through different degrees of freedom including path, polarisation and

1 Introduction

time bin [14]. One scheme for quantum computing is referred to as linear optical quantum computing. Here, single photons are used along with beam splitters, phase shifters and single photon detectors [4].

Quantum metrology uses quantum processes such as entanglement to measure with a higher statistical precision than is possible using classical techniques [7]. Single-photon states can be used as measurement probes in these schemes [15, 16].

All of these optical quantum technologies require a source of controllable quantum photon states, in-particularly the ability to create single photons. Semiconductor quantum dots (QDs) are a solid-state system that can be used as a source of single-photons [17–19]. QDs can be incorporated into cavity structures to enhance their emission properties. One of the solid-state systems that can be used to achieve QD single-photon sources with enhanced emission properties are nano-photonic crystal cavities and waveguides [20, 21]. These structures can also be used for the routing and manipulation of the photons produced [22–24], making them a potential building block for “on-chip” quantum computing [25, 26].

In this thesis, the properties of a QD that is weakly coupled to a H1 photonic crystal cavity but with an extremely large Purcell factor of 43 ± 2 are investigated. This coupling enables a Purcell-shortened radiative lifetime of 22.7 ± 0.9 ps under resonant excitation of the QD’s neutral exciton, a property that is exploited throughout this thesis, allowing the exploration of regimes that otherwise would not be possible.

1.2 Outline of this work

This thesis looks at the properties of a cavity-coupled self-assembled quantum dot (SAQD), its single-photon properties, interaction with its solid state environment and how the photon statistics of the source can be manipulated.

In Chapter 2 an introduction to the concepts used throughout this thesis are presented. This background includes an introduction to the growth and properties of SAQDs, the effects of the environment on QD emission as well as the effects of optical cavities. Chapter 3 describes the basic experimental methods used throughout the experimental chapters. This includes a description of the resonance fluorescence (RF) set-up, the bath cryostat system, the excitation lasers and detection systems used. Along with details of the calibration methods used for defining the excitation power related to the state of the QD system. Chapter 4 contains the details of the QD sample used for the measurements in this thesis, including the composition of the semiconductor wafer and the fabrication method of the photonic crystal cavity structure. This chapter also includes a summary of the characterisation work that has previously been performed on the sample by other researchers.

In Chapter 5 the single-photon properties of the cavity-coupled QD are investigated under resonant pulsed excitation. Hanbury Brown and Twiss second-order correlation measurements are used to measure the antibunching, and Hong-Ou-Mandel second-order correlation measurements are performed to find the indistinguishability of the single-photons produced. The effect of the excitation pulse length compared to the QD lifetime is investigated under both measurement schemes along with an additional investigation into the effect of pulse separation on the photon indistinguishability.

In Chapter 6 the effect of the QD's environment on its coherently scattered emission is investigated to provide insight into the phonon interactions present in the system. First-order correlation measurements are used to investigate the phonon relaxation timescale. Spectroscopic measurements are used to investigate the effect of excitation power on the phonon properties. The effect of laser detuning on the coherent scattering is also investigated through first-order correlation measurements.

1 Introduction

In Chapter 7 the effect of spectrally filtering the collected RF emission on the measured photon statistics is investigated. By using filters of various bandwidths both above and below the natural linewidth of the QD a comprehensive picture of the effect on the photon statistics can be produced, including investigation in both the low power Rayleigh scattering regime and high power Mollow triplet regime.

Chapter 8 contains a summary of the experimental chapters and some possible directions for future work involving QDs in high Purcell factor cavities.

2 Background

2.1 Single Photon Sources

As was described in Chapter 1, single photon sources are a building block for many optical quantum technologies including optical quantum computing [3–5] and quantum cryptography [1, 2]. However, single-photons are also desirable for many other quantum-optics applications including boson sampling [27, 28], single-photon fast optical switching [29], photonic cluster state generation [30] and a quantum internet [2, 31, 32] to mention just a few.

All of the above uses for single-photons require certain properties from their single-photon source (SPS). They need to be bright, pure, on-demand and indistinguishable [33, 34]. For a SPS to be bright it is optimal for it to be excited preferentially to an optically-bright state with a short emitter lifetime. This allows the emitter to be re-excited at a fast rate and so produce photons with a high repetition rate. To be bright, measurements of SPS also require a high collection efficiency [35–37]. The purity of a SPS involves measuring the photon statistics of the emission. Purity is defined as the probability that the output of the SPS comprises single photons, rather than multi-photon emission. On-demand is the probability that an input will create the desired output, i.e. that every excitation event results in a single photon being emitted rather than no emission or multi-photon emission. Indistinguishability, also known as visibility, is the probability that the single photons emitted are identical to each other.

In this thesis a self-assembled quantum dot in a nano-photonic crystal cavity is investigated as a single-photon source.

2.2 Quantum Dots

In this section an introduction to quantum dots is given, including the formation mechanism of self-assembled quantum dots and their electronic structure.

2.2.1 Quantum Wells, Wires and Dots

Electron waves in semiconductors can be characterised by their de Broglie wavelength:

$$\lambda_D \sim \frac{h}{\sqrt{m_e^* k_B T}}, \quad (2.1)$$

where h is Planck's constant, m_e^* is the effective mass of the electron, k_B is the Boltzmann constant and T is the temperature. In a bulk semiconductor crystal, where all of the dimensions (x, y and z) are longer than the λ_D of the electron it is free to travel in any dimension. However, it is possible to create structures where some or all of the dimensions are comparable to λ_D . This quantises the electron's motion within those dimensions, confining its travel.

Figure 2.1 shows different confinement shapes where one or more dimensions have been reduced to be comparable to λ_D . A system with confinement in one dimension (e.g. x -direction) allows the electron to travel freely in the other two dimensions. This system is known as a quantum well. Confinement in two dimensions (e.g. x and y -directions) allows free movement in one dimension and is known as a quantum wire. A quantum dot (QD) confines the electron in all three dimensions. It therefore acts as a three-dimensional potential well with quantised electron motion in all three directions.

Figure 2.1 also shows how the confinement shape of the structure affects the density of states $D(E)$ function of electrons in the conduction band of a semiconductor. Here, E_g is the semiconductor bandgap. With each successive degree of confinement, the band edge is shifted by the quantum confinement energy. This applies to the

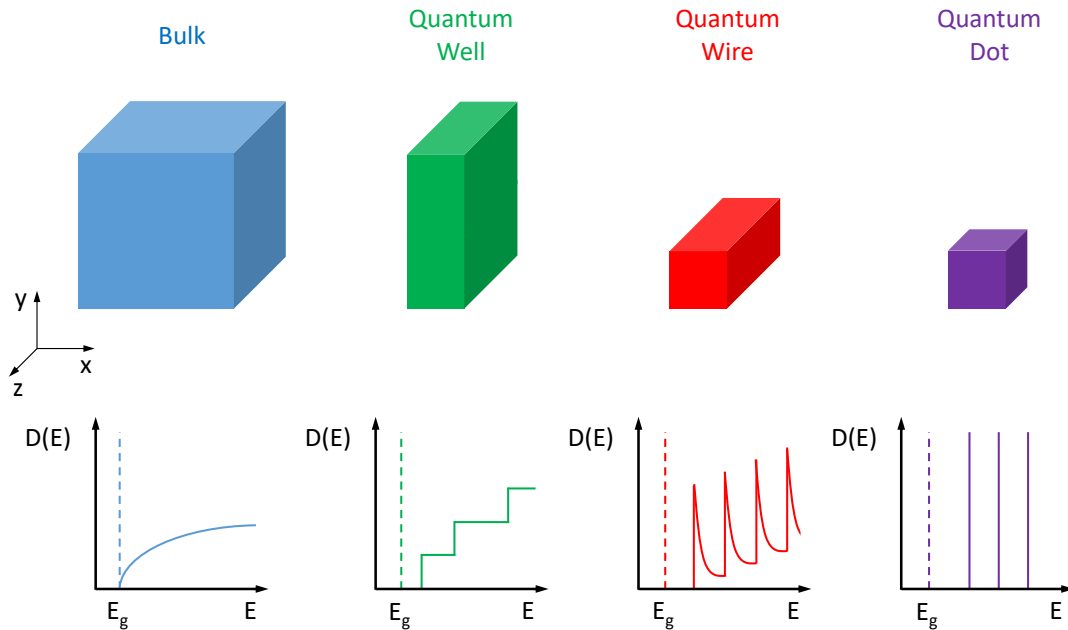


Figure 2.1: Representation of a bulk semiconductor as well as a quantum well, wire and dot. The density of states $D(E)$ of electrons in the conduction band is altered for each confinement, where E_g is the semiconductor band gap.

holes in the semiconductor valence band as well as to the electrons in the conduction band, further increasing the effective bandgap of the quantised semiconductor structure. It can be seen that for QDs the density of states has the form of δ -functions with no continuous energy bands. This gives quantum dots a level structure with discrete energies, leading to their description as “artificial atoms”. This level structure will be discussed during this chapter along with how it can be manipulated.

The de Broglie wavelength can be used as a first approximation of confinement. However, real systems are more complicated. For example, for a QD laser the confinement is given by the separation of the electron and hole states. If the energy separation of the states is greater than the confinement energy then they are not confined. An-

2 Background

other way to model whether a particle or quasi-particle is confined by a QD is to use the Bohr radius. Significant confinement requires the Bohr radius of the quasi-particle to be comparable to the dimensions of the QD. For example, an exciton is a quasi-particle formed by an electron and hole that are a bound pair through Coulomb interaction. The Bohr radius (r) is given by:

$$r = \epsilon \left(\frac{m}{\mu} \right) a_0, \quad (2.2)$$

where ϵ is the dielectric constant, given by the square of the refractive index (n), a_0 is the Bohr radius, m is the mass of the electron and μ is the reduced mass of the exciton. The reduced mass is given by:

$$\mu = \frac{m_e m_{hh}}{m_e + m_{hh}}, \quad (2.3)$$

where m_e and m_{hh} are the effective masses of the electron and hole, respectively. For GaAs, $n = 3.45$, $m_e = 0.067m$ and $m_{hh} = 0.51m$. When combined with $a_0 = 5.29 \times 10^{-11}$ m and $m = 9.11 \times 10^{-31}$ kg the Bohr radius of the exciton is found to be ~ 11 nm. Therefore, a QD requires a radius on the order of 11 nm to show exciton confinement. Excitons in QDs can be used as a basis for a single-photon source and will be discussed in more detail in Section 2.2.3.

2.2.2 Self Assembled Quantum Dots

Quantum dots come in many forms. The first QDs where the quantum confinement of carriers was observed were microscopic crystals of CuCl grown within a glass matrix [38]. Since then, other methods of creating QDs including colloidal [39], droplet epitaxy [40] and self-assembled Stranski-Krastanow growth [41, 42] have emerged. This thesis will focus on self-assembled quantum dots (SAQDs) grown using the “bottom-up” Stranski-Krastanow regime method [42].

Stranski-Krastanow QDs

Stranski-Krastanow (SK) QDs are self-organising and are commonly known as self-assembled quantum dots (SAQDs). The growth method of SK QDs is shown in Figure 2.2. QD growth in the SK regime involves deposition of a thin, two-dimensional

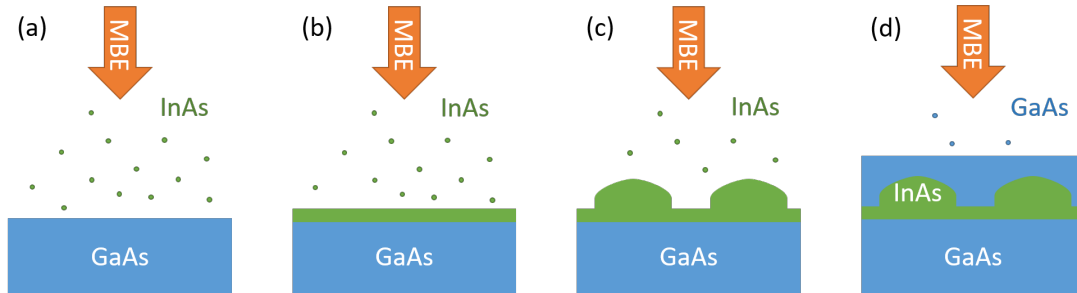


Figure 2.2: Growth of self-assembled QDs in the Stranski-Krastanow regime: (a) InAs deposited on a GaAs substrate by MBE. (b) A thin layer of InAs builds up on the GaAs. The strain in the InAs layer is high due to the difference in unit cell size between the GaAs and InAs. (c) When the InAs reaches a critical thickness it begins to form 3D “islands” on the 2D substrate to reduce the total energy of the InAs. These islands are QDs. A thin “wetting” layer remains between the QDs and the GaAs substrate. (d) To prevent oxidation the QDs are capped with GaAs.

(2D), layer of semiconductor crystal by molecular beam epitaxy (MBE) or metal-organic vapour-phase epitaxy (MOVPE) (also known as metal-organic chemical vapour deposition (MOCVD)) [43–46]. This layer is deposited on top of a semiconductor crystal substrate which has a different lattice constant. For example, when growing InAs on GaAs (Fig. 2.2(a-b)) there is a 7% difference in lattice constant [47]. When the InAs layer is thin, its lattice constant compresses to match that of the GaAs. As the deposition continues, layer by layer, there is a build-up in the strain InAs due to the lattice compression [48]. When the top layer reaches the critical thickness, the crystal surface splits into microscopic “islands” (QDs), transitioning from a 2D to a 3D structure, in order to reduce the strain in the growth layer (Fig. 2.2(c)). The increase in the surface energy caused by the dislocations is smaller than the reduction to the internal strain that this process generates. A thin “wetting” layer remains between the QDs and the growth substrate.

2 Background

QDs grown in the SK regime are commonly used in quantum optics measurements as they can be incorporated into structures by overgrowing (capping) the strained layer with a different semiconductor (Fig. 2.2(d)). As well as preventing oxidation, capping enables the production of integrated photonic nanostructures through the production of diodes and optical cavities above and below the QD layer. When the cap is grown, mixing can occur between the cap and the QDs. For example, growing GaAs on InAs QDs can lead to InGaAs QDs. QDs grown using this method have also been shown to have good optical properties, e.g. narrow linewidths of the zero phonon line (ZPL) [49], which, when combined with photonic structures, makes them ideal candidates for qubits and single-photon sources.

QD Positioning

SAQDs grown in the SK regime are scattered randomly on the semiconductor substrate. However, photonic nanostructures, some of which are discussed in Section 2.5, require precise placement of the structure around the QD. Therefore, many photonic devices are fabricated per QD wafer, to increase the probability that a randomly positioned SAQD will be optimally aligned. This can lead to a large number of “waste” structures that do not contain optimally positioned QDs being produced and so time needs to be spent on characterising the structures before measurements can be performed.

One possible solution to this is through the site-controlled growth of QDs. There are many ways of trying to control the lateral position of QD nucleation [50]. For example, one method involves the patterning of the semiconductor substrate surface with differently shaped pits including pyramidal [51, 52] and round pits [53–55] to encourage the nucleation of QDs in predefined positions.

Another possible solution is the registration of QDs before the photonic structures are fabricated. One way to register the position and emission wavelength of QDs in-

volves using scanning microscopic photoluminescence (μ -PL) spectroscopy [56] and mapping the emission against markers patterned on the sample's surface. Another method involves an imaging set-up where the QDs in the sample are excited with above-band excitation using LED illumination and the QD emission is imaged on a CCD camera. Filters used between the sample and the camera can be used to define the emission bandwidth of the QDs that are mapped. Again, markers patterned on the sample surface are used to map the positions of the QD emission [57–59].

2.2.3 Electronic Structure of QD

Band Structure

At 4.2 K the bandgap (E_g) of GaAs is 1.52 eV [60]. When introducing an InGaAs QD to the bulk semiconductor the reduced E_g of the InGaAs leads to a 3D confinement of carriers. The E_g of the QD depends on the ratio of Gallium to Indium present, with higher proportions of Indium leading to a smaller E_g [61]. Figure 2.3 shows the modification to the semiconductor bandgap caused by the presence of InGaAs QD within bulk GaAs. The energy difference between the s -shell and p -shell of the electrons in the conduction band is greater than that of the hole bands, as is the offset of the conduction and valence bands [48]. The confinement energy of the carriers is temperature dependent. At 4.2 K, the thermal energy of the carriers ($k_B T$) is ~ 0.36 meV, much smaller than the spacing of the electron and hole energy levels. At room temperature, $k_B T$ is ~ 25 meV, and the energy levels are therefore effectively no longer discrete.

The bandstructure of a III-V semiconductor is shown in Figure 2.4. It shows that the conduction band (purple) is inhabited by electrons and the valence band (blue) by holes but whereas the conduction band contains only one band, the valence band contains three. To explain this difference the total angular momentum of the electrons and holes has to be considered.

2 Background

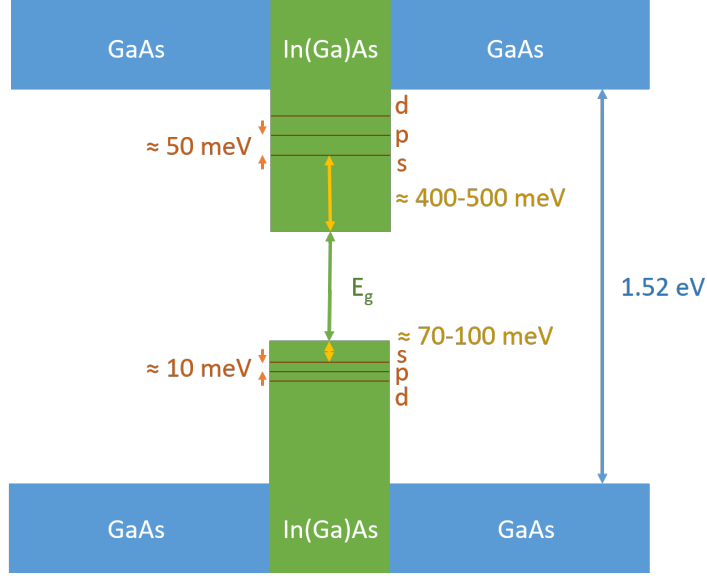


Figure 2.3: Bandgap diagram of an InGaAs QD within bulk GaAs. At 4.2 K the E_g of GaAs is 1.52 eV [60]. The E_g of the InGaAs QD is smaller and its exact value depends on the ratio of Ga:In within the QD, the higher the proportion of In the smaller the value of E_g [61]. The energy difference between the s -shell and p -shell for the electrons in the conduction band is larger than the energy difference of the hole shells in the valence band, as is the offset of the bands [48].

The total angular momentum (\mathbf{J}) is given by:

$$\mathbf{J} = \mathbf{L} + \mathbf{S}, \quad (2.4)$$

where \mathbf{L} is the orbital angular momentum and \mathbf{S} is the spin angular momentum. The eigen values of the angular momentum (J) are given by $|l - s| \leq j \leq l + s$ [62]. The conduction band of a bulk III-V semiconductor has similar properties to the s -shell of atomic physics. This means that it has an orbital angular momentum of $l = 0$. As electrons are elementary particles and fermions, they have a spin angular momentum s of $1/2$. Looking at the total angular momentum in the z -axis leads to $J_z = \pm 1/2$ to allow for the two possible spin configurations of the electron, spin up and spin down.

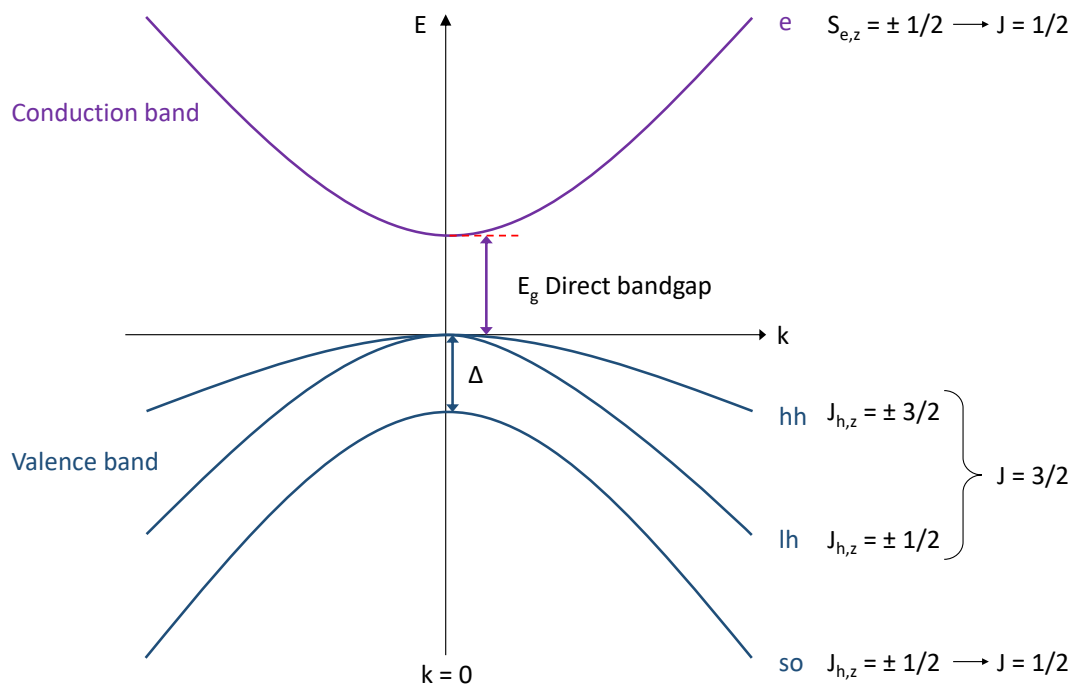


Figure 2.4: Band structure of a typical, direct bandgap, bulk III-V semiconductor showing both the conduction and valence bands. Electrons are found in the conduction band (purple) which contains one band and is separated from the valence band by the bandgap (E_g). The holes in the valence band (blue) are split into three bands, the heavy hole band (hh), light hole band (lh) and split-off band (so). The so band is split from the hh and lh bands by the spin-orbit splitting Δ . At $k = 0$ the hh and lh bands are degenerate but split with increasing k .

The valence band of III-V semiconductors has predominantly p -shell properties with some d -shell properties. The p -shell properties lead to an orbital angular momentum of $l = 1$. Combining this with the spin of the holes ($s = 1/2$) means the valence band is split into two states with $j = 3/2$ and $j = 1/2$. Again, these states can be projected into the z -axis creating one state with $J_z = -3/2, -1/2, 1/2, 3/2$ and a second state with $J_z = -1/2, 1/2$. The two states are separated by an energy difference of Δ which is the

2 Background

spin-orbit splitting. For GaAs $\Delta \approx 0.3$ eV [62]. The $J = 3/2$ state is further split into two bands, one being the heavy hole (hh) band with $J_z = \pm 3/2$ and the light hole (lh) band with $J_z = \pm 1/2$. As is shown in Figure 2.4 for a bulk semiconductor the light hole and heavy hole bands are degenerate at $k=0$. However, for QDs that lack symmetry, for example SAQDs, strain removes the degeneracy, leading to a splitting of the bands of ~ 30 -300 meV [63, 64] with the light hole band being found at higher energies. This splitting of the hole bands means that the light holes can be neglected when modelling the lowest energy states of the QD, giving QDs a lowest energy state with the properties of the s -shell electron and heavy holes.

Excitons

Excitons are created when an electron is excited out of the valence band into the conduction band, leaving a positively charged hole quasi-particle behind. If the excitation energy is small, then the electron remains confined within the QD and the two oppositely charged particles can become a bound electron-hole pair through the Coulomb interaction. This quasi-particle is known as an exciton (X). As the exciton consists of a negatively charged electron and positive hole then its overall charge is neutral. Recombination of the electron and hole results in the emission of a photon.

One property of excitons is a doublet formed in the emission spectrum where each peak of the doublet has the opposite linear polarisation. This is termed fine-structure splitting (FSS) and is undesirable for photon entanglement experiments [65, 66]. The origin of the FSS can be found in the angular momentum of the electron and hole that the exciton comprises. The angular momentum of the exciton states is described in the z -direction by:

$$m = S_{e,z} + J_{h,z} = \pm 1, \pm 2. \quad (2.5)$$

Here the electron spin is $S_{e,z} = \pm 1/2$ and the heavy hole spin is $J_{h,z} = \pm 3/2$. The $m = \pm 1$ states are optically active, unlike the $m = \pm 2$ states which are referred to as dark excitons. Fine-structure splitting (FSS) occurs in asymmetric QDs. The asymmetry of the QD means that the confinement potential of the electron and hole within the QD

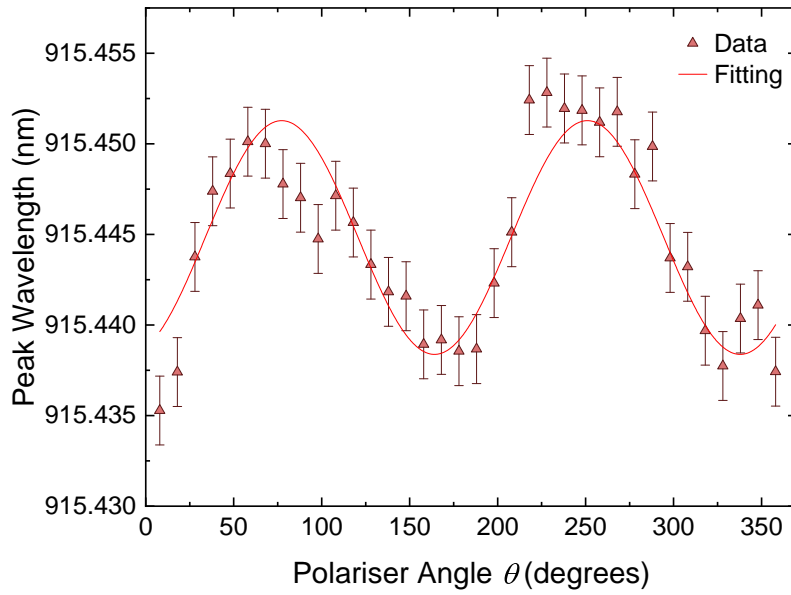


Figure 2.5: An example of the fine-structure splitting measurement for a neutral exciton. The FSS is measured by rotating a linear polariser in the collection path and recording the intensity of the neutral exciton peak. Here, the QD used is the sample that is described in Chapter 4, showing a FSS of 0.013 nm (19 μeV).

plane is not symmetric and results in an exchange energy splitting of the $|m| = 1$ exciton states creating a doublet. The split states are linear combinations of the $m = \pm 1$ exciton states and this mixing results in linear polarisation of the QD emission from each state [67]. The two components of the FSS doublet are polarised along the principle axes of the QD potential [68].

FSS can be resolved by using linearly polarised detection as the excitons emit photons with orthogonal polarisation. An example of this measurement is shown in Figure 2.5. Here, a QD is excited above band and spectra of the exciton emission are taken as a function of the collection polarisation angle. When the wavelength of the exciton emission is plotted against the polarisation angle, the splitting of the doublet

2 Background

is seen as an oscillation of the emission wavelength. The amplitude of the oscillation gives the **FSS**, in Figure 2.5 the splitting is 0.013 nm (19 μeV). The example used here is the **FSS** measurement for the **QD** sample used in this thesis, the sample will be discussed in more detail in Chapter 4. **FSS** can be used to show the charge characteristics of the **QD** transitions. The neutral exciton shows **FSS** whereas the positive and negative trions, quasi-particles comprising two holes and an electron or two electrons and a hole respectively, do not show **FSS**.

Different methods have been used to try to reduce the **FSS** seen in **QDs**, including through the use of applied electric fields [69], strain [70], magnetic fields [65] and localised annealing [71]. **QDs** grown in nanowires have also been used to reduce **FSS** due to their high symmetry [72].

2.3 QDs in Applied External Fields

Experimentally, different external fields can be applied to **QDs** and are used to change their emission properties and behaviour. This section will discuss the effects of applying electrical and optical fields.

2.3.1 Quantum-Confined Stark Effect

The wavelength of photons emitted by the exciton depends on the energy difference between the electron and hole when they recombine. The energy difference can be modified by applying a direct current (**DC**) electric field across the **QD**, modifying the band structure. An illustration of this modification is shown in Figure 2.6. The exciton is still confined to the **QD** due to the reduced band gap of the **InGaAs** compared to that of the **GaAs**. The applied **DC** field modifies the shape of the bands, altering the band structure which brings the electron and hole closer together in energy and in doing so reduces the energy of the photon that is emitted when the exciton recombines. This modification is known as the quantum-confined Stark effect (**QCSE**).

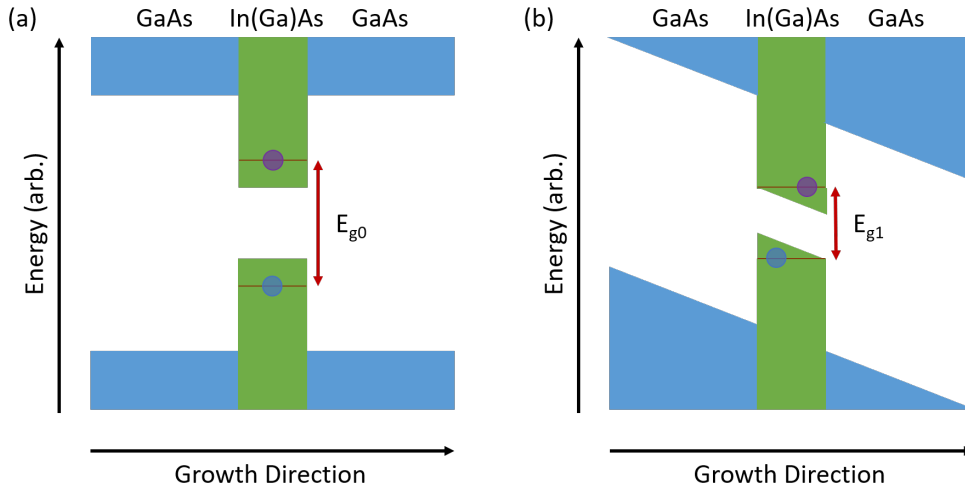


Figure 2.6: An illustration of the band structure of a QD: (a) No electric field is applied to the QD, giving an exciton emission energy of E_{g0} . (b) Application of a DC electric field to the QD modifies the band structure, causing a reduction in the energy of the exciton from E_{g0} to E_{g1} and so shifting its emission wavelength.

The shift of the emission energy (ΔE_{QCSE}) is defined as a function of the applied DC electric field and is described by:

$$\Delta E_{QCSE} = pF + \beta F^2, \quad (2.6)$$

where F is the strength of the applied DC field, p is the electric dipole moment of the QD and β is the polarisability [73, 74].

When a high DC electric field is applied the carriers can be swept out of the QD, preventing the exciton from forming. Embedding the QDs within a quantum well creates potential barriers that prevent carriers from tunnelling out when a high electric field is applied. This can increase the potential tuning range of the QD emission through the QCSE. For example, embedding InGaAs QDs within an AlGaAs/GaAs/AlGaAs quantum well has shown a tuning range for the exciton emission energy of 25 meV [75]. In the absence of barriers, the tuning range of the emission is limited to a few hundred picometers [76].

2 Background

QCSE tuning of QDs has numerous practical uses. These include tuning QDs into resonance with cavity structures, moving QDs into and out of resonance with excitation lasers, which is used to evaluate the emission signal to the background laser, and to perform differential measurements. The QCSE can also be used to tune QDs into resonance with each other. Tuning multiple QDs into resonance within the same nanophotonic structure requires split contact diodes where different DC field strengths can be applied to different parts of the device. These methods make use of the large energy shift possible when using vertical DC electric fields as the orientation of the QD dipole is in the z growth direction. Vertical DC fields can be applied through the use of diode structures where doped semiconductor layers are grown above and below the QD layer. The QCSE can also be utilised when applying lateral DC electric fields to the QD. One use for lateral DC fields is for tuning QD FSS. The effect of lateral fields on the FSS has been shown for QDs that are not built into photonic structures [69, 77, 78]. Work on applying lateral fields to photonic structures such as waveguides has also been progressing [79].

2.3.2 Optical Stark Effect

An alternating current (AC) electric field can also be applied to QDs, for example through the oscillating electric field of a laser. When an atom is excited with a high intensity laser, at resonance or close to resonance with its transition, then the “bare” states of the atom are “dressed” by the oscillating optical field. The dressed states are split by the Rabi frequency (Ω_R). A QD can be described as a “artificial-atom” due to the quantisation of its states and so QDs also experience splitting in the strong driving regime. This behaviour is known as the AC Stark effect [47, 80].

QDs are often modelled as a two-level emitter (TLE). For a TLE, the strong driving regime occurs when the strong resonant excitation has a Rabi frequency larger than the natural linewidth of the exciton ($\Omega_R^2 \gg \frac{1}{T_1 T_2}$), where T_1 is the emitter lifetime and

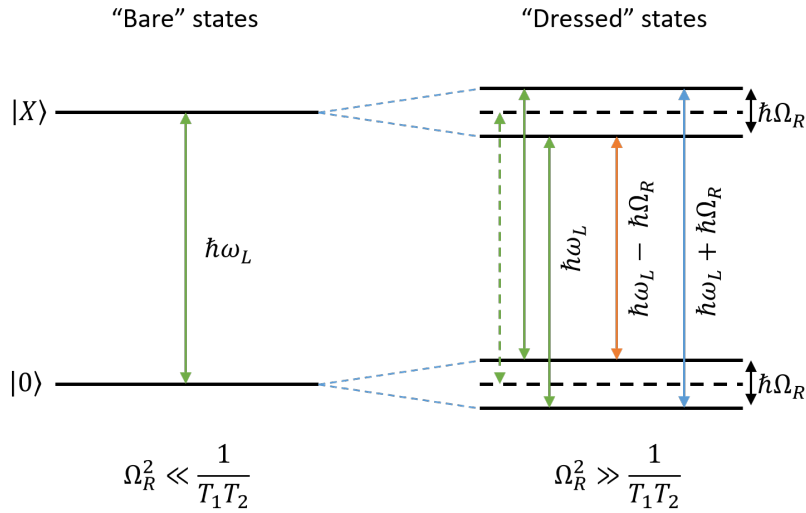


Figure 2.7: An illustration of the dressing of the “bare” states of the exciton transition through the application of a high power laser field. The “dressed” states lead to four possible transitions of which two are degenerate, leading to the three peaks observed in a Mollow triplet spectra. Here, Ω_R is the Rabi frequency, T_1 is the emitter lifetime, T_2 is the coherence time and $\hbar\omega_L$ is the transition energy.

T_2 is the coherence time, both of which are discussed in more detail in Section 2.4.1. Here, the two-level picture breaks down and is replaced by a dressed states approach [81], as shown in Figure 2.7. Two of the transitions (green) are degenerate, leading to the production of the Mollow triplet. The central peak (green) is termed the Rayleigh peak and the two sidebands (orange/blue) are separated from the central peak by $\pm\Omega_R$. If the driving laser is not resonant with the TLE then Ω_R is modified to become the generalised Rabi frequency: $\Omega = \sqrt{\Omega_0^2 + \Delta^2}$, where Ω_0 is the bare Rabi frequency and Δ is the detuning of the laser from the QD transition [82].

2.4 Interactions

This section describes some of the effects that QDs experience through interactions with their solid-state environment.

2.4.1 Dephasing

SAQD comprise many atoms and are embedded within bulk semiconductor material. This environment leads to dephasing of the excited state of the QD. Throughout this thesis the excited state being described is the exciton state. Dephasing of the exciton state originates from processes such as interactions with the bulk lattice, as well as effects due to the movement of carriers in and around the QD, amongst others. Dephasing can be split into three types: T_1 , T_2 , and T_2^* .

T_2 is termed the transverse relaxation time and describes how long the state remains coherent. The T_2 dephasing rate depends on both T_1 and T_2^* through the relationship:

$$\frac{1}{T_2} = \frac{1}{2T_1} + \frac{1}{T_2^*}. \quad (2.7)$$

T_1 is termed longitudinal relaxation and accounts for the loss of coherence determined by population decay from the excited state to the ground state. Population decay can occur due to spontaneous radiative decays such as the recombination of an exciton. Non-radiative processes such as the tunnelling of carriers out of the QD also contribute to T_1 [83]. T_2^* is the “pure dephasing” time and changes the coherence of the state without changing the population. In QDs “pure dephasing” mainly occurs from interactions with the lattice through phonons; dephasing caused by phonons is temperature dependent and can be reduced by cooling the QD system [47, 84]. In the absence of phonon or carrier interactions and in the absence of non-radiative recombination channels, then the dephasing time of the QD exciton is limited by radiative decay of the upper level ($T_2^* \gg T_1$) and so is termed as being lifetime-limited, $T_2 = 2T_1$ [47, 83, 85].

2.4.2 Phonons

As SAQDs are grown within bulk semiconductor crystals, there is coupling between the QD and the vibrational phonon modes of the host lattice. Phonons can be split into two categories; Longitudinal Optical (LO) phonons and Longitudinal Acoustic (LA) phonons.

LO phonons have discrete energies. This property leads to the observation of “phonon replicas” [86–88]. For InGaAs QDs the “phonon replica” peaks have been observed in spectra to be negatively detuned by ~ 36 meV away from the exciton emission of the QD [89]. This is comparable to the LO phonon energy of bulk GaAs which is 36.59 meV [89, 90]. The discrete LO phonons also allow quasi-excitation of the QD, exciting at integer multiples of the LO energy to positive detunings [91–93]. LO phonons will not be investigated in this thesis.

LA phonons have a continuous energy distribution of a few meV rather than discrete energies [94]. The presence of LA phonons in the emission spectra of QDs is observed as a broad phonon sideband (PSB) around a narrow zero-phonon line (ZPL). A model of the resonance fluorescence (RF) emission for the QD described in Chapter 4 is shown in Figure 2.8, a semi-log plot is used as the PSB has a small RF contribution compared to the ZPL. The PSB forms when a QD relaxes from its excited ($|X\rangle$) to its ground ($|0\rangle$) state. The ground state can be modelled as a manifold of phonon states and so the system can relax into any of these states via spontaneous emission of a photon and then reaches the ground state through the absorption or emission of a phonon. The combined energy of the phonon and photon sum to a level in the manifold. The manifold is generated by displacement of the ions in the lattice when the charge configuration of the QD changes, for example during the creation of an exciton [94, 95]. The asymmetry of the PSB occurs as at ~ 4 K there is a higher probability of emitting a phonon than absorbing one. These LA phonon properties will be discussed in more detail in Chapter 6.

2 Background

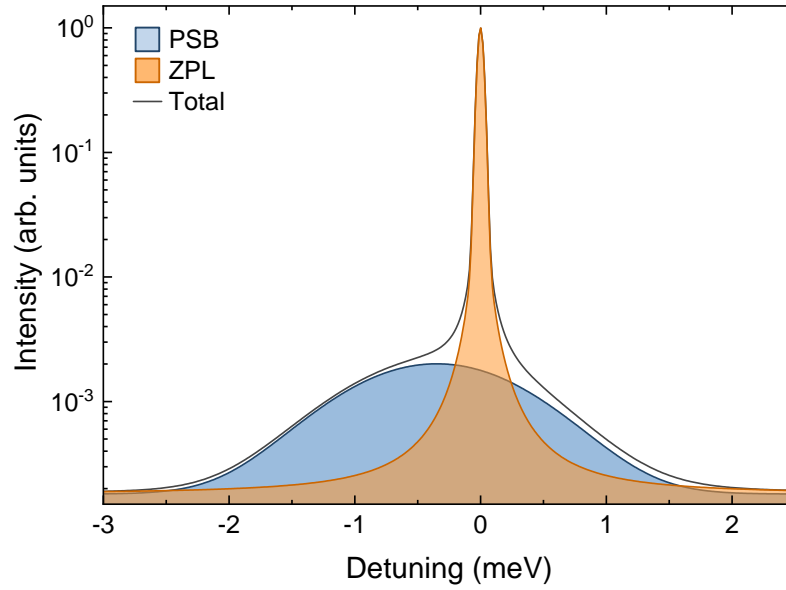


Figure 2.8: A theoretical model of the resonant fluorescence emission from the neutral exciton of an InGaAs QD described in Chapter 4 at ~ 4 K. The spectra shows the narrow ZPL (orange) and the broad asymmetric PSB (blue) components of the total spectra (black line).

For QDs, LA phonons have been shown to be a major source of dephasing [96–98]. LA phonons lead to “pure dephasing” by providing incoherent alternative relaxation paths. For example, when optically driving a QD with a pulsed laser, the laser couples the ground states of the QD and the exciton states to form optically dressed states that are split by the Rabi frequency (Figure 2.7). Emission and absorption of LA phonons with energy equal to the Rabi splitting can result in relaxation between the dressed states, leading to pure dephasing [98]. They also have a strong temperature dependence [94, 98, 99], increasingly broadening linewidths and enhancing dephasing effects with higher temperatures. Due to this, QD measurements are usually performed at ~ 4 K to minimise LA phonon effects. The PSB can be undesirable as it reduces the indistinguishability of the photons produced by a QD. Hence, methods

to remove the PSB emission from QD spectra have been developed including the use of spectral filters applied to the emission or using cavities to enhance the ZPL emission [95, 100]. Both filters and cavities improve the indistinguishability but can limit the efficiency of the QD device.

As well as LA phonons there are also Transverse Acoustic (TA) phonons. The carrier-phonon interaction that TA phonons originate from is Coulomb interaction with the piezoelectric field, generated by shear crystal deformation. In InGaAs QD systems this effect is weak [101–103]. Therefore, TA phonons are not considered in this thesis.

2.5 Cavities

Optical cavities can be used to modify the emission properties of QDs. This section will describe cavity theory, the weak and strong coupling regimes, as well as a discussion of some of the cavity structures that are used in QD quantum optics.

2.5.1 Theory

A simple cavity can be visualised as two highly reflective mirrors separated by a distance (L_{cav}), as shown in Figure 2.9(a). Light is confined to the plane of the cavity, forming standing waves between the two mirrors. Dependent of the length of the cavity some frequencies of light constructively interfere while others destructively interfere. Constructive interference forms resonant cavity modes for light with frequency ω_{cav} . Destructive interference causes the suppression of other frequencies.

An ideal cavity has no losses. A real optical cavity, however, has losses due to the mirrors not being perfect reflectors. This allows leakage of light from the cavity, defined as the photon loss rate, κ . Photon loss from the cavity leads to a broadening of the cavity mode linewidth ($\Delta\omega$). This broadening is often described through use of

2 Background

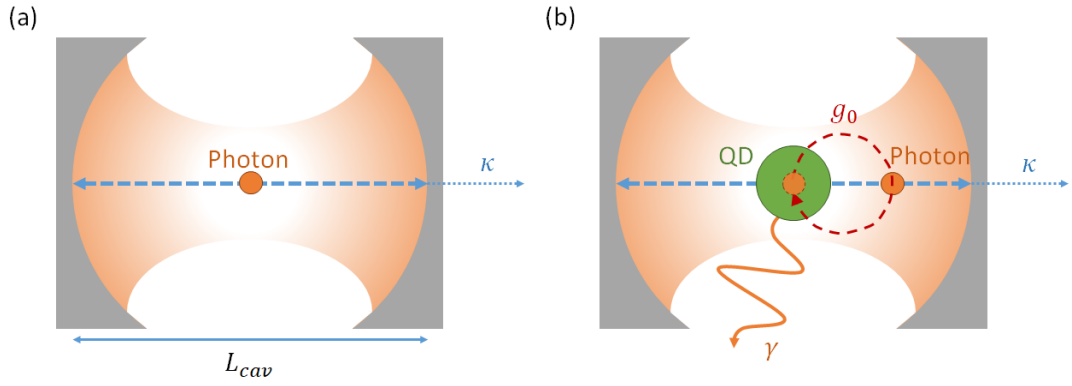


Figure 2.9: Schematic of a simple cavity: (a) The photons are confined between two mirrors with the field focussed in the centre of the cavity. As the mirrors are not perfect reflectors some photons are lost from the cavity given by the rate κ . (b) Cavities can be constructed around QDs. The coupling strength between the cavity photons and the QD is given by the emitter-photon coupling rate g_0 . The decay and dephasing rate of the QD is given by γ .

the cavity quality factor, Q , where:

$$Q = \frac{\omega_{cav}}{\Delta\omega}. \quad (2.8)$$

A large Q -factor cavity indicates a longer photon containment time and lower photon leakage.

Q describes the spectral quality of the cavity; spatial quality is described by the mode volume V_m . The mode volume is defined as the integral of the normalised electric field energy density over the volume of the cavity. V_m is often given in units of cubic wavelength, $(\lambda/n)^3$.

Cavities can be built around QD emitters, shown schematically in Figure 2.9(b), altering their emission properties. The interaction between the QD and the cavity requires the QD emitter to have both spectral and spatial overlap with the cavity. The strength

of the QD-cavity interaction is defined using the emitter-photon coupling rate, g_0 :

$$g_0 = \left(\frac{\mu^2 \omega}{2\epsilon_0 \hbar V_m} \right)^{1/2}, \quad (2.9)$$

where μ is the dipole moment of the QD and ϵ_0 is the permittivity of free space. The emitter-photon coupling rate can be used to define different operating regimes for a QD in an optical cavity.

2.5.2 Weak Coupling

Weak coupling occurs when:

$$g_0 \ll \kappa, \gamma, \quad (2.10)$$

where the interaction between the QD and the cavity is dominated by incoherent decay process such as cavity losses (κ) and the decay and dephasing of the QD (γ). In the weak coupling regime, the emission from the QD is irreversible as the photon that is emitted escapes from the cavity but the emission rate of the QD is affected by the cavity. The modification to the QD emission rate is defined by the Purcell effect [104] which can either enhance the rate of spontaneous emission or suppress it depending on the detuning between the QD and the cavity. The Purcell factor (F_P) is determined by the properties of the cavity along with the spectral and spatial overlap of the cavity mode and the QD emission. F_P is defined as [47, 105]:

$$F_P = \frac{T_1'}{T_1} = \frac{3Q}{4\pi^2 V_m} \frac{\omega_{cav}^2}{4Q^2(\omega - \omega_{cav})^2 + \omega_{cav}^2} \epsilon^2, \quad (2.11)$$

where T_1 is the radiative lifetime, T_1' is the radiative lifetime in the absence of a cavity, Q is the quality factor of the cavity and V_m is the mode volume in units of (λ/n) . The Lorentzian part of Equation 2.11 gives the spectral lineshape of the cavity where ω is the angular frequency of the emitter and ω_{cav} is the cavity resonance. The spatial overlap between the emitter and the cavity mode is described by the normalised dipole orientation factor $\epsilon = \frac{|\vec{\mu} \cdot \vec{E}(\vec{r}_0)|}{|\vec{\mu}| |\vec{E}_{max}|}$ where $\vec{\mu}$ represents the transition dipole moment, $\vec{E}(\vec{r}_0)$ the electric field at the QD position and \vec{E}_{max} is the maximum electric field. To maximise the transition dipole moment, and so the coupling between the

2 Background

QD and the cavity, the electric field and the QD dipole moment need to be orientated parallel to each other. When the QD emission is resonant with the centre of the cavity mode, F_P can be simplified to:

$$F_P = \frac{3Q}{4\pi^2 V_m} \left(\frac{\lambda_c}{n} \right)^3, \quad (2.12)$$

where λ_c is the cavity wavelength and n is the refractive index of the cavity medium. Purcell factors greater than one indicate an enhancement of the spontaneous emission rate. A high Purcell factor, giving a shortened T_1 , can lead to lifetime-limited coherence of $T_2 = 2T_1$ [106]. A Purcell factor of less than one leads to suppression of the spontaneous emission by the cavity [47].

2.5.3 Strong Coupling

Strong coupling occurs when [106, 107]:

$$16g_0^2 > (2\kappa - \gamma_1)^2, \quad (2.13)$$

where $\hbar g_0$ is the QD-cavity coupling strength, $2\hbar\kappa$ describes the cavity linewidth and $\hbar\gamma_1$ is the QD natural linewidth. In the strong coupling regime, photons emitted by the QD can be reabsorbed by the QD before leaving the cavity. These oscillations of the photons between the exciton state of the QD and the cavity are known as vacuum Rabi oscillations [108, 109] and are described by the Jaynes-Cummings model [110] for a TLE when using quantised excitation with small photon numbers.

The QD-cavity system described in this thesis operates in the weak coupling regime.

2.5.4 Photonic Crystal Cavities and Waveguides

Cavity structures used to enhance the QD light-matter interaction strength are commonly referred to as micro- or nano-cavities, dependent on the scale of the structure, particularly on its mode volume. An example of a family of nano-cavity structures

used with integrated SAQDs are photonic crystal cavities (PhCC). The photonic structure used throughout this thesis is a PhCC.

The photonic crystal (PhC) as used in this work is created within a thin GaAs membrane (which in later experiments contains InGaAs QDs). The suspended membrane is created by chemically etching a sacrificial layer below the thin GaAs layer (discussed later in Section 4.2). The difference in refractive index between the GaAs and the surrounding air on the upper and lower faces of the structure provides confinement of light within the membrane due to total internal reflection.

Etching periodic cylindrical holes in the semiconductor membrane results in a periodic modulation of the refractive index, with $n_{air} = 1$ and $n_{GaAs} = 3.4$, which can be used to control the propagation of light in the plane of the membrane. Figure 2.10(a) shows a photonic crystal with a triangular lattice of air holes where the lattice constant is a . The lattice can be characterised using its photonic band structure, in a manner analogous to the electronic band structure of a semiconductor crystal lattice. For a triangular lattice the reciprocal lattice has a hexagonal Brillouin zone, as shown in Figure 2.10(b), where the high symmetry points are labelled Γ , M and K. Figure 2.10(c) shows the photonic band structure of the triangular PhC modelled using MPB (MIT Photonic Bands [111]) by Andrew Foster. MPB uses Maxwell's equations to calculate band structures and dispersion relations in periodic dielectric structures. In addition to depending on the lattice constant a , the resulting band structure also depends on the thickness of the simulated lattice (t) and the radius of the etched cylinders (r), both of which are defined in terms of a . For Figure 2.10(c), $t = 0.71a$ and $r = 0.31a$. The simulation also requires the refractive index (n) of the semiconductor, in this case $n = 3.4$ was used.

In Figure 2.10(c) the black line marks the light line. This denotes the boundary below which the modes are confined within the PhC membrane by total internal reflection.

2 Background

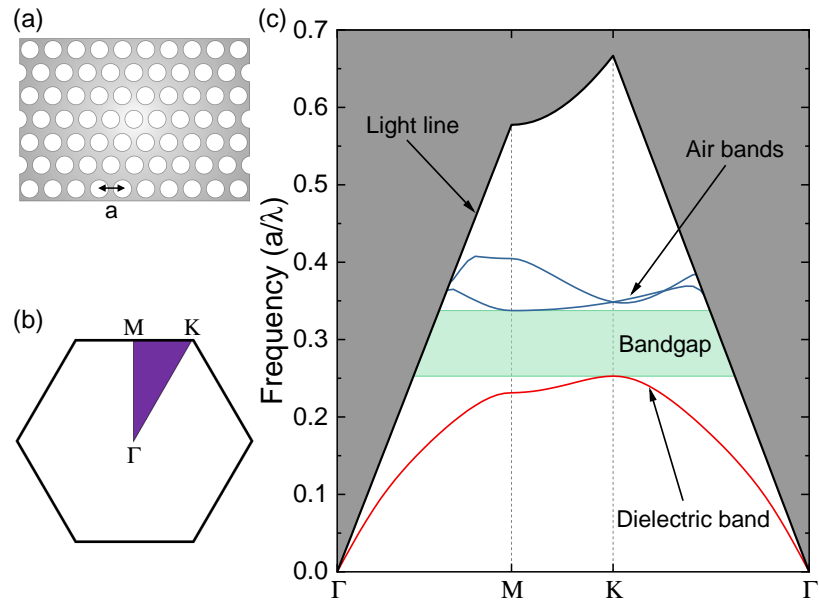


Figure 2.10: Triangular lattice photonic crystal: (a) A triangular lattice of cylinders (with period a and cylinder radius r) is etched through a thin dielectric membrane (with thickness t), creating a suspended 2D PhC. (b) The Brillouin zone of a triangular lattice in reciprocal space, with points of high symmetry labelled Γ , M and K. (c) Bandstructure of the triangular PhC for TE modes, simulated using MPB. A photonic bandgap (green) can be seen between bands that represent optical states which are confined within the PhC membrane (red/blue). Here, the parameters used are $r = 0.31a$, $t = 0.71a$ and a refractive index of 3.4. The band structure was simulated by Andrew Foster.

Above this line (grey region) any modes leak out of the PhC. The red and blue bands shown lie within the light line and so can propagate through the PhC membrane [112]. The red line is termed a dielectric band. For this band the electric field is concentrated within the dielectric of the lattice. The blue bands are termed air bands. Here, the electric field is concentrated within the etched holes of the lattice. The lattice of periodic refractive indexes generates a photonic band gap (green) where the

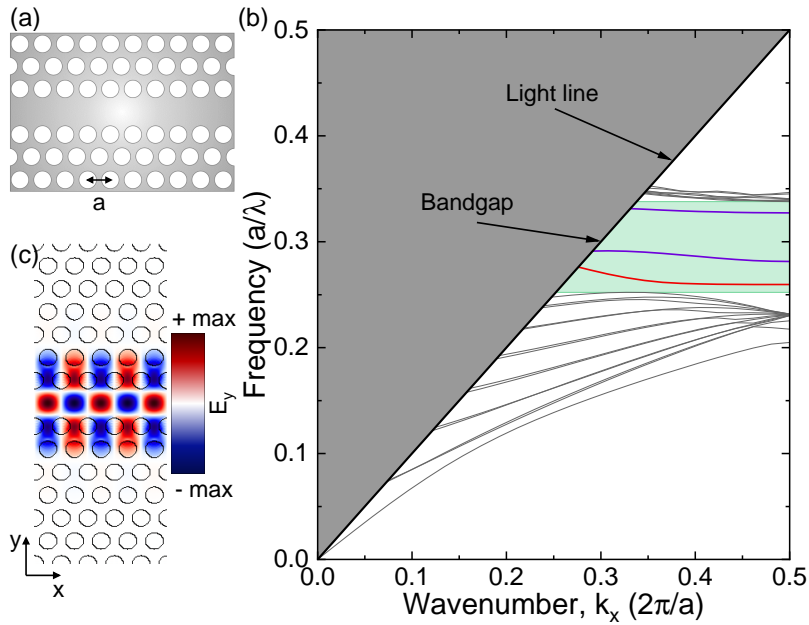


Figure 2.11: W1 waveguide: (a) Schematic of a W1 PhC waveguide, in which a single row of cylinders is left unetched in a 2D triangular lattice. (b) MPB simulation of the TE mode bandstructure of the W1 waveguide. Note that k_x lies along the waveguide. The photonic bandgap (green) now contains modes (red/purple) that are confined to the waveguide. The simulation uses the same parameters as Figure 2.10. (c) Simulated electric field profile (E_y component) in the plane of the PhC membrane, for the lowest confined mode (red line in (b)). Simulations of the bandstructure and electric field confinement were performed by Andrew Foster.

propagation of light is forbidden [113–115]. Tuning the wavelengths of this bandgap is possible by manipulating one or more properties of the lattice, such as the period. The photonic bandgap acts as a mirror for light with a wavelength which falls within it.

Waveguide and cavity structures can be created by introducing defects into the PhC lattice, for instance by leaving one or more of the cylindrical holes unetched. Omit-

2 Background

ting a complete row of cylinders, known as a line defect, allows a waveguide to be formed. Figure 2.11(a) shows a schematic of a W1 waveguide where a single row of cylinders is left unetched. The dispersion of the waveguide is modelled in MPB using the same parameters as in Figure 2.10. The resulting dispersion diagram for a waveguide along the k_x direction is shown in Figure 2.11(b).

The diagonal line in Figure 2.11(b) is the light line, above which (grey region) light leaks from the upper and lower surfaces of the semiconductor membrane. Below this line the band structure shows the bands that are confined within the PhC. When simulating a defect structure it is necessary to use a projected band structure. The bands of the PhC are projected along the direction of the W1 waveguide (k_x direction), forming the boundaries of the membrane band continuum [116]. As in Figure 2.10(c), Figure 2.11(b) shows a bandgap (green) between the upper and lower continuum bands. However, the difference here is that there are three additional modes within the bandgap. These are guided modes which are confined within the W1 waveguide, as can be shown by visualising the electric field profile of each mode. For instance, in Figure 2.11(c), the simulated E_y component of the electric field for the lowest frequency confined mode (red line in Figure 2.11(b)) is plotted. The field is clearly localised within the defect which forms the waveguide.

The gradient of the confined modes in Figure 2.11(b) is related to the group velocity of the mode, and is highly frequency dependent. For the lowest frequency guided mode it can be seen that closer to the light line the gradient is steep, signifying that this is a fast light region. Closer to the edge of the Brillouin zone the gradient reduces, indicating that the mode has a lower group velocity. This is termed the slow light effect and can be used to enhance the emission rate from QDs via the Purcell effect [117–119].

Introducing a line defect in the PhC, as discussed above, created a waveguide, with

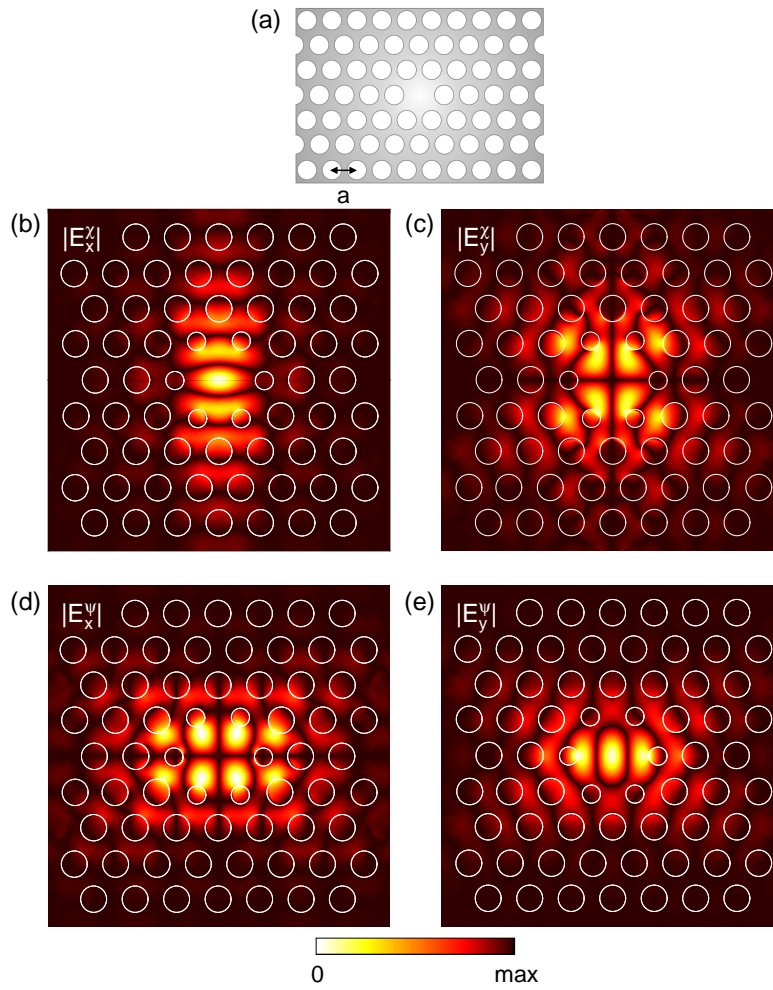


Figure 2.12: H1 PhCC: (a) Schematic of a triangular lattice of cylinders etched through a semiconductor membrane, with one cylinder omitted, forming a H1 PhCC. (b)-(e) Results of FDTD simulations showing the position-dependent electric field components for the two orthogonal fundamental modes of the H1 PhCC, labelled χ and ψ . (b) $|E_x^\chi|$ and (c) $|E_y^\chi|$ show the cavity $|E_x|$ and $|E_y|$ electric field components, respectively, for the χ mode. (d) $|E_x^\psi|$ and (e) $|E_y^\psi|$ show the cavity $|E_x|$ and $|E_y|$ electric field components, respectively, for the ψ mode. The H1 cavity uses the same parameters as the triangular lattice PhC from Figure 2.10 and was simulated by Andrew Foster.

2 Background

light only able to propagate in a single direction. If instead a point defect is introduced within the PhC, full confinement of the light can be achieved, creating a photonic crystal cavity (PhCC). A common example of such a cavity in quantum optics research is the H1 PhCC. This is formed when single cylinder in a triangular lattice remains unetched, as shown in Figure 2.12(a). The H1 cavity supports two orthogonal and degenerate fundamental cavity modes which are labelled here χ and ψ . Figures 2.12(b-e) show the simulated E_x and E_y electric field spatial profiles for these modes. The profiles were obtained using finite-difference time-domain (FDTD) simulations, with the same parameters for lattice period, membrane thickness, and refractive index as used for the triangular lattice PhC in Figure 2.10. The $|E_x^\chi|$ and $|E_y^\psi|$ fields have anti-nodes at the cavity centre, whilst nodes are seen for the orthogonal components $|E_x^\psi|$ and $|E_y^\chi|$. This means that the cavity modes have orthogonal linear polarisations at the cavity centre. This linear polarisation allows independent excitation of a single mode using an appropriately orientated dipole at the cavity centre, which is how the field profiles were obtained using FDTD. The χ -mode is the cavity mode that is excited with an x -dipole in the centre of the H1 cavity. The ψ -mode is excited with a y -dipole in the centre of the cavity [120]. However, away from the centre of the cavity the field has contributions from both E_x and E_y , and is therefore no longer linearly polarised.

To maximise the cavity Q -factor, the radius and position of the etched cylinders closest to the defect can be modified, as shown by the overlaid lattice in Figure 2.12(b-e). By altering only the etched cylinders nearest to the defect, a Q -factor of 30,000 can be obtained by simulation [121, 122]. Achieving the maximum Purcell factor for a QD embedded in such a cavity requires both spectral and spatial overlap between the QD and the cavity mode. Spatial overlap is achieved when the QD is located in a region of high electric field strength. Typically, the cavity centre allows the strongest coupling [122]. As the electric field extends beyond the cavity in Figures 2.12(b) and (e), W1 waveguides can be coupled to the χ and ψ cavity modes, allowing routing

of photons away from the cavity [121]. A H1 PhCC structure is used throughout this thesis and is discussed in more detail in Chapter 4.

Another common type of PhCC are L3 cavities. These are formed where a row of three cylinders in a triangular-lattice PhC remains unetched. Like H1 cavities, L3 cavities can also be coupled to W1 waveguides and various methods exist for optimising these nano-cavities to improve their Q -factors and waveguide coupling. These methods include modifying the radius and separation of the etched cylinders closest to the cavity and the distances between the cavities and waveguides [120, 123, 124]. Coupling QDs to PhCCs allows manipulation of their emission properties and waveguides can be used for “on-chip” routing of both excitation lasers and the QD emission for quantum-optics measurements.

2.5.5 Other Types of Cavities

Another example of where PhCs can be used to create cavity structures are nanobeam cavities, Figure 2.13(a). A nanobeam cavity is created by etching cylinders into a nanobeam waveguide to create two distributed Bragg reflector (DBR) mirrors with a cavity between them [125–127]. The properties of the cavity can be tuned by changing the number, separation and radius of the etched cylinders as well as the width of the central unetched region that constitutes the cavity. The waveguide cavity structure is also useful for routing both excitation lasers and emitted photons around nanophotonic structures.

DBR mirrors can also be produced by layering semiconductor materials with different refractive indexes. This is the principle used in the creation of micropillar cavities, Figure 2.13(b). Micropillars can be created by growing alternating layers of GaAs and AlAs to create DBR mirrors either side of a SAQD layer. The semiconductor wafer is then etched to create micropillars. The DBR mirrors create confinement in the vertical direction. In the horizontal direction confinement is achieved by total internal reflec-

2 Background

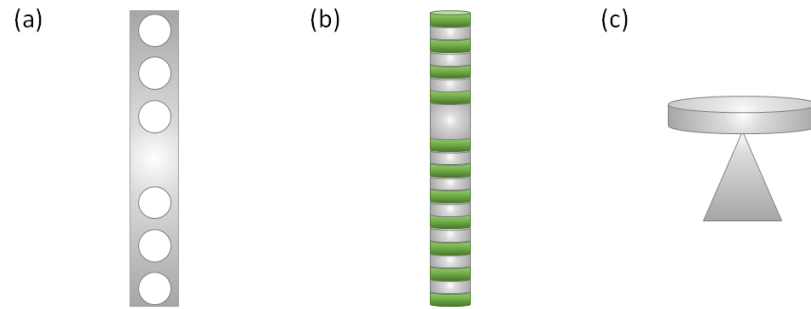


Figure 2.13: Schematics of cavities that can be created around SAQDs. (a) A nanobeam PhCC is created by leaving a cylinder unetched from the periodic lattice. This cavity is a 2D structure. (b) A micropillar cavity is a 3D structure where confinement is created using multilayered DBR mirrors either side of the QD layer. Fewer DBR repetitions are used above the cavity to enhance vertical emission. (c) A microdisk cavity comprises a disk of semiconductor containing QDs which is supported by a pedestal. Total internal reflection supports whispering gallery modes, creating a high Q cavity.

tion, caused by the difference in refractive index between the semiconductor cavity and the surrounding air. Micropillars can achieve very high coupling efficiencies vertically for both the excitation laser and the QD emission by having a higher number of DBR layers below the cavity than above, funnelling the emitted light out of the top of the micropillar. This efficient coupling has also been shown with cavities that have high Q -factors [128–130]. A disadvantage of this system, however, is that they are difficult to incorporate into photonic circuits and the “on-chip” photon routing that the PhC geometry is well suited for.

Another type of high Q cavity used with SAQDs are microdisk cavities. These cavities are created by etching a disk of semiconductor material that is held above a substrate on a pedestal, as shown in Figure 2.13(c). Light is trapped within the cavity in all three dimensions by total internal reflection, creating whispering gallery

modes. However, microdisks have a large mode volume which reduces the possible Purcell factor despite their high Q -factors [131–133]. Also, like micropillars, their QD emission cannot be routed “on-chip” to perform in-situ quantum-optics experiments.

The QD investigated in this thesis is coupled to a H1 PhCC. The QD experiences a high Purcell factor of 43, leading to a fast emitter lifetime and a broad, transform-limited linewidth. W1 waveguides are used for “on-chip” routing of the photons emitted by the QD. The sample used is discussed in more detail in Chapter 4.

3 Experimental Methods

In this chapter the experimental methods used to set-up the quantum-optics measurements described in this thesis are discussed. Details of the individual quantum-optics measurements are discussed within their relevant chapters. All of the following measurements were performed on [InGaAs QDs](#) held at cryogenic temperatures.

3.1 Introduction

In this chapter there is a discussion of the laboratory equipment that was aligned, optimised and used in all of the following measurements by Catherine Phillips and Alistair Brash, unless otherwise specified. This discussion includes details of the optical table (Section [3.2](#)) where all of the excitation lasers, interferometers and most of the detectors that are used in the following measurements are mounted and aligned. Along with the liquid [He](#) bath cryostat (Section [3.3](#)) that holds the [QD](#) sample at 4.2 K and the resonance fluorescence ([RF](#)) set-up (Section [3.4](#)) that is used to excite the [QD](#) sample. Resonance fluorescence was used in all of the experiments described in this thesis.

This chapter also describes the different pulsed and continuous wave ([CW](#)) lasers (Section [3.5](#)) used to excite the [QD](#) sample and calibrate measurement set-ups. This description includes the power control utilised for the pulsed and [CW](#) lasers and the 4f pulse shapers used to modify the output of the pulsed laser. Section [3.6](#) discusses the photon detection systems used in the following experiments. These include single-photon detectors that allow for timing information about the photons

3 Experimental Methods

emitted by the QD to be measured and a spectrometer which measures the spectral properties of the QD emission. Section 3.7 discusses the calibration methods for the excitation power experienced by the QD under both types of laser excitation.

3.2 Optical Table

All the excitation lasers, interferometers, optical filters and most of the detectors used during the following measurements are built on an optical table. The optical table is actively stabilised using pneumatic legs that are supplied with compressed air. In addition to the vibrational stability provided by the pneumatic legs, the components mounted on the optical table are also kept thermally stable through the use of high-density foam walls and covers. The covers also reduce the amount of stray light that reaches the experiments and detectors, reducing background dark counts. Within the covers, additional black hardboard dividers (Thorlabs) are used to create enclosures around the high-power pulsed laser and its pump laser, as well as around the spectrometer and interferometers to further reduce stray light detection.

The optical table has a modular design where the individual experimental components, for example the interferometers and lasers, all have separate single-mode fibre inputs and outputs. Having separate fibre paths for each piece of equipment allows the routing of the excitation lasers and the collected sample emission through different measurement and calibration schemes. For example, either the sample emission or an excitation laser can be directed through an interferometer to a detector by changing one fibre connection. This increases the scope of possible measurements and allows for easier characterisation of measurement equipment than if the optical paths are fixed. Where possible, the single-mode optical fibres are attached to the table to increase stability and reduce possible polarisation drifts from fibre movement during measurements. The high-density foam covers also aid this by reducing air movement over the optical table. Using optical fibres to connect equipment rather

than free-space optics can lead to losses from coupling light to and from the fibres. Loss also occurs where different fibres are connected. To avoid this loss, the ends of the fibres are cleaned when any connection is changed. Building the smaller set-ups such as fibre-based Mach-Zehnder interferometers and etalon filters on separate breadboards on the main optical table also allows them to be moved between labs.

3.3 Cryostat

All of the following measurements were performed with the sample held in a liquid helium bath cryostat. The bath cryostat allows long-term positional stability as opposed to flow cryostat systems. A schematic of the cryostat system is shown in Figure 3.1. The cryostat is filled with ~ 90 litres of liquid He which is kept under back pressure. The He gas that boils off is collected and recycled centrally using a He recovery system and liquefier. The cryostat level is topped up every two weeks to keep the sample at ~ 4.2 K. The cryostat is mounted on passive isolators to provide vibrational isolation for the cryostat and sample.

Within the cryostat is an insert tube 1.4 m in length and 10 cm in diameter. A cage system (Thorlabs) is used to hold the sample inside the insert tube. The sample is mounted on an x, y, z piezo stack to allow manipulation of the sample position relative to the excitation laser beam. Between the sample and the piezo stack is a heater and temperature probe so that temperature dependent measurements can be performed. This capability was not used for any of the measurements in this thesis which were all performed at ~ 4.2 K. Above the sample the cage system holds an aspheric lens (Edmund Optics) with a focal length of 4.51 mm that focuses the laser excitation on to the sample. The lens has a diameter of 6.33 mm and a numerical aperture (NA) of 0.55. The resulting focused laser spot has a FWHM of ~ 1.8 μm at a wavelength of 950 nm. A high NA lens with a short focal length is used to increase the collection efficiency and resolution of the set-up. A window at the top of the insert tube al-

3 Experimental Methods

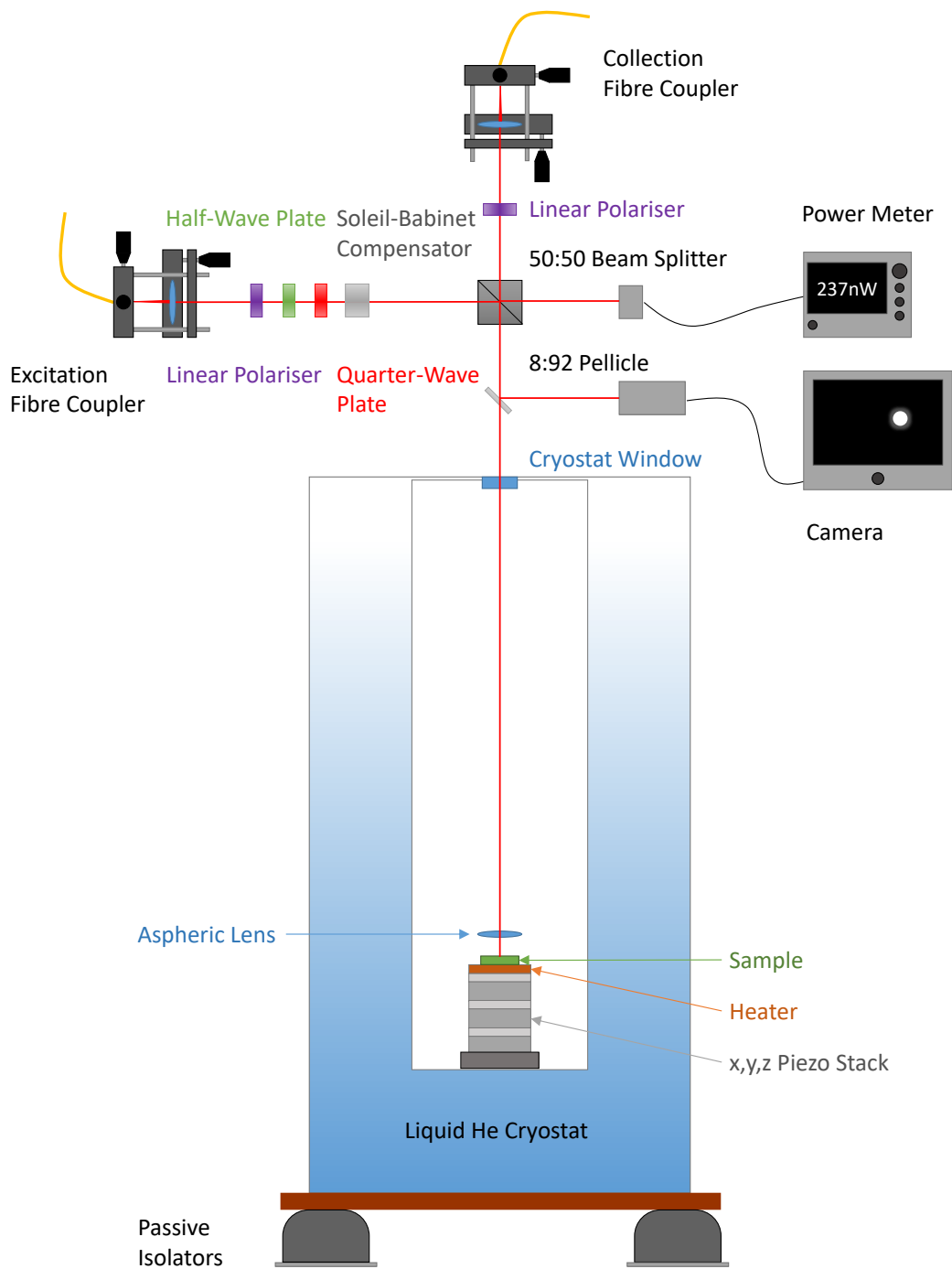


Figure 3.1: Schematic of the liquid He bath cryostat, including excitation and collection optics used for resonance fluorescence. The sample is mounted on an x,y,z piezo stack to allow for sample positioning. Passive isolators are used to provide vibrational isolation for the cryostat.

lows optical access to the sample. The cage system that holds the sample also allows alignment with the optical breadboard that is mounted above the cryostat and holds the excitation and collection optics, shown above the cryostat in Figure 3.1. Before the insert tube is loaded into the cryostat it is pumped down to high vacuum. A small amount of He gas ($\sim 10 \text{ cm}^3$) is then admitted in to the insert tube to act as an exchange gas and allow thermal contact between the sample and the bath cryostat.

3.4 Resonance Fluorescence

Figure 3.1 shows a schematic of the optics used to perform resonance fluorescence (RF) measurements on the sample. The excitation laser is routed from the optical table to the cryostat-mounted breadboard using a single-mode optical fibre. A single-mode fibre is also used for the collection path. Using optical fibre for the excitation and collection paths allows the use of different lasers from the optical table to excite the sample without realignment. The fibre collection path, from above the cryostat, also allows the routing of the collected photons to different detection schemes on the optical table. Single-mode optical fibres are used as their small core allows focusing to a diffraction limited laser spot, creating spatially well-defined excitation and collection spots when focussed onto the sample. The small, well-defined excitation and collection spots allow the measurement of micro-photoluminescence (μ -PL) rather than macro-PL, enabling the collection of μ -PL or RF from a single QD rather than from the QD ensemble. Free space or multi-mode fibre collection has a higher collection efficiency. However, without the use of a pin hole in the collection path to remove light that is unfocused or reflected from the sample at a wide angle the collection would be macro-PL. The small core of the single-mode fibre acts as a pin hole.

The excitation and collection paths can be independently adjusted allowing separate excitation and collection positions on the sample. Ideally, the single-mode fibres and the aspheric lens above the sample in the cryostat would be numerical aperture (NA)

3 *Experimental Methods*

matched to increase the collection efficiency, as a mismatch in the NA can result in under or overfilling the lenses and the single-mode fibre core. However, for historical reasons, here the lens in the cryostat is not NA matched to the single-mode fibres. For the sample lens in the cryostat an aspheric lens is used to reduce the spherical aberration that occurs when the beam is not centred on the optical axis of the lens. Non-centred beams can occur as the independent excitation and collection paths allows the beams to be offset from each other at the sample. Spherical aberration would reduce the efficiency of the coupling back into the single-mode fibre and would also affect the imaging of the sample.

The 8:92 pellicle beam splitter is mounted on a flip mount so that it can be moved in or out of the beam path. The pellicle diverts 8% of the beam to a camera, allowing viewing of the sample using the laser reflected from the sample surface. The camera is used for aligning the sample's excitation or collection by routing the laser through the excitation or collection paths respectively. The pellicle is removed from the beam path during measurements. A white-light source cannot be used to view the sample as the optics are optimised for infra-red wavelengths and so the white-light is not focused onto the sample. This results in the collected reflection being very weak.

A cross-polarisation measurement scheme is used to suppress the laser that is scattered from the surface of the sample. The linear polariser mounted in the excitation path remains stationary while the linear polariser in the collection path is rotated until the orientation of the linear polarisation is matched to the desired sample emission. The half-wave plate and quarter-wave plate, mounted on Newport "Agilis piezo motor rotation stages", are then rotated to minimise the laser back reflection by rotating the excitation polarisation to be orthogonal to the collection polariser. The Soleil-Babinet Compensator is used to correct for birefringence through the optics and from the surface of the sample to further improve the laser suppression. The suppression of the reflected laser also has a dependence on the laser bandwidth. Continuous

wave (CW) lasers have a narrow bandwidth and this allows greater suppression to be achieved than the broadband pulsed laser emission. This is due to the birefringence of the optics on the breadboard and sample stick as well as from the surface of the sample, leading to wavelength-dependant laser suppression. Spectral filters can be used to reduce the amount of background laser collected.

3.5 Excitation Lasers

This section contains details of the excitation lasers used for the quantum-optics experiments in this thesis.

3.5.1 Power Control

A half-wave plate and variable neutral-density (ND) filter are mounted before the excitation lasers are coupled into the single-mode fibre that routes them up to the sample breadboard. The half-wave plate is used to maximise the transmission through the fibre, correcting for any changes of polarisation that occur from bending the fibre. The variable ND filter is used to control the laser power that enters the fibre. On the breadboard, the power is monitored using a power meter mounted behind a 50:50 beam splitter. Half of the laser power is directed to the sample the other half is monitored by the power meter. For pulsed and CW lasers, two different types of ND filters are used. The excitation power of the pulsed laser remains stable for long periods of time, allowing multi-day measurements to be performed with few corrections to excitation power drift. This stability allows the use of gradient ND filters mounted on rotation stages. The ND filter can be moved remotely during an experiment to correct for slight drifts of the power. These ND filters can also be used to measure power dependences, either by rotating the filter by set amounts and recording the power or by manually rotating the filter until the required power is achieved.

For CW driving a different power stabilisation technique is used. During measurements the CW power is much more sensitive to laboratory conditions and can drift

3 Experimental Methods

as the laser warms up or if the laser wavelength shifts slightly, particularly when using tunable CW lasers. Also, the CW power can jump when performing wavelength dependent measurements and so a stabilisation method with a rapid response time is required. For this a *p-i-d* method was developed by Dr Alistair Brash, Dr Tillmann Godde and Lisa Scaife. The power at the breadboard is measured using a Newport “2936-R optical power meter”. As well as being able to connect to the computer for remote power monitoring, the power meter has a 250 kHz analogue output, where the voltage is proportional to the power detected. This voltage is monitored by a Arduino Uno microcontroller board which has the *p-i-d* program loaded. The Arduino supplies a voltage to a Thorlabs “Electronic variable optical attenuator” (VOA) which the CW laser passes through while on the optical table, before being coupled to the excitation fibre. The VOA adjusts the power transmitted as a function of the voltage applied to it. The *p-i-d* routine mounted on the Arduino adjusts the output voltage until the voltage measured from the power meter agrees with the voltage expected for the desired power. This voltage is determined using a relationship calculated from a calibration measurement performed during the initial set-up of the *p-i-d* program.

3.5.2 Pulsed: Coherent Mira 900F

The pulsed laser used for the following experiments is the Coherent Mira 900F. This is a Ti:Sapphire (Ti:S) mode-locked pulsed laser where the pulses have a full-width half maximum (FWHM) of $\Delta t \sim 100$ fs. The Ti:S is pumped by a Verdi G10 high-power optically-pumped semiconductor laser which has a 10 W, $\lambda = 532 \pm 2$ nm CW output. The Verdi G10 and the Ti:S crystal of the Mira are cooled with a closed-loop de-ionised water chiller to 17°C. The Mira also has a dry nitrogen purge line to prevent adsorption from water in the atmosphere between 920 and 980 nm. The Mira can tune from 700 - 1000 nm and is mode-locked using Kerr Lens Mode-Locking [134]. The laser pulses have a separation of 13.2 ns and a repetition rate of 76 MHz. After the Mira on the optical table there is a glass slide that diverts part of the beam to a laser spectrometer, along with the internal photodiode of the laser this is used to

ensure that the laser is pulsing at the required wavelength.

3.5.3 CW: Toptica DL Pro

The Toptica DL Pro is a continuous wave (CW) tunable single-mode diode laser. A semiconductor diode laser is routed through an external high-finesse grating cavity in the Littrow configuration. The first-order beam from the grating is reflected back into the laser diode to create the external cavity. The wavelength of the laser is coarsely tuned by adjusting the angle of the diffraction grating. Fine tuning is then achieved by changing the length of the external cavity through the use of a piezo actuator that holds the grating, changing the current through the laser diode or changing the temperature of the diode. A combination of all three methods can be used to tune the laser to a precision of 0.001 nm. The Toptica DL Pro has a tuning range of 910 - 985 nm and a bandwidth of ~ 10 neV. An external wave meter is used to monitor the emitted wavelength.

3.5.4 CW: M-Squared SOLSTIS

The M-Squared SOLSTIS is a CW tunable single-mode Ti:S laser. The M-Squared is cooled with a closed-loop de-ionised water chiller to 20 °C. The Ti:S crystal is pumped by a 7 W Lighthouse Photonics Sprout-G which is a diode-pumped solid-state laser that emits at 532 nm. The tuning range of the M-Squared is 700-1000 nm. The wavelength is controlled using a computer interface which uses an external wavemeter and *p-i-d* to tune and stabilise the wavelength. Remote computer control makes the M-Squared an ideal laser for wavelength dependence measurements that involve repeated tuning of the excitation laser wavelength and also for single wavelength experiments that require long measurements without wavelength drifts.

3.5.5 CW: Thorlabs LP808-SA60

The Thorlabs LP808-SA60 is a $\lambda = 808$ nm diode laser that is used for non-resonant excitation of the sample. The diode is mounted in a Thorlabs LDM21 thermoelectri-

3 Experimental Methods

cally (TE)-cooled mount which keeps the diode at 25°C, stabilising the wavelength of the diode. The laser diode emits into free-space and passes through a variable wave plate and a variable ND filter before being coupled into a single-mode fibre. The wave plate and ND filter allow control over the laser power that reaches the sample.

3.5.6 Pulse Shaping

Pulse shaping allows fine control over the centre wavelength and pulse length of the pulses produced by the Mira Ti:S laser. After the pulses leave the laser they pass through a pair of 4f pulse shapers, the schematics of which are shown in Figure 3.2. The pulse shapers are used to convert the ~ 100 fs pulses into longer pulses with a length of $\sim 1 - 15$ ps. Increasing the length of the pulses narrows them spectrally so that they can be used to address individual QD transitions. The 1200 l mm^{-1} diffraction grating splits the pulsed laser emission into its spectral components. A plano-convex lens, situated at one focal length (f) beyond the grating, then focuses the spectrally diverging pulse. An adjustable mechanical slit is mounted in the Fourier plane, one focal length after the lens. In the Fourier plane each horizontal position corresponds to a different optical frequency. Therefore, the slit can be used to transmit a narrow range of the possible frequencies and so reduce the bandwidth of the pulse, increasing the temporal length. A second plano-convex lens and diffraction grating, located at f and $2f$ beyond the Fourier plane respectively, are used to recombine the spectrally separated components of the pulse. The pulsed laser is then coupled into single-mode fibres. The adjustable slit is mounted on a motorised translation stage which also allows the centre wavelength of the shaped pulses to be modified.

As can be seen in Figure 3.2 there are two separate pulse shapers. The laser is split between the two pulse shapers using a half-wave plate and a polarising beam splitter. This allows for the creation of pump and probe pulses with different pulse durations, centre wavelengths and powers. One pulse shaper includes a delay stage so that the relative time between two pulses can be modified. The length of the pulses can

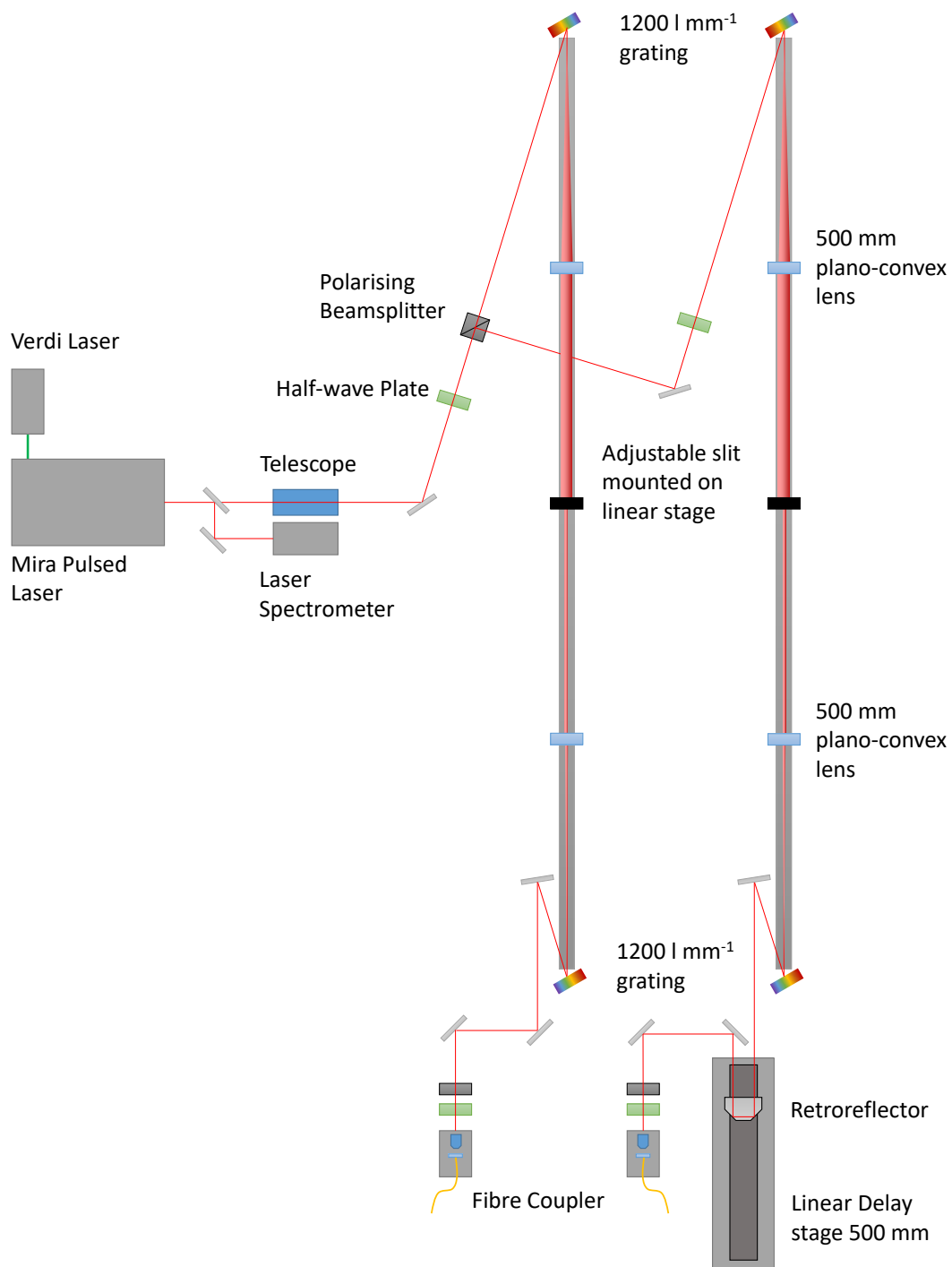


Figure 3.2: Schematic of the 4f pulse shapers used to convert ~ 100 fs laser pulses into ~ 1 -15 ps pulses with a tunable central wavelength.

3 Experimental Methods

be found using two methods. Longer pulses can be attenuated and imaged on the spectrometer. The spectrum can then be fitted and the **FWHM** can be converted into a temporal pulse length. An autocorrelator (APE Mini) can be used to measure the length of the unshaped pulse when the adjustable slit has been removed from the pulse shaper. The autocorrelator is used as the unshaped pulses are spectrally too broad for measurement using the spectrometer.

3.6 Detection Systems

The photon emission from the lasers and from the sample needs to be detected and analysed. The main detection systems used in the experiments throughout this thesis are single-photon avalanche diodes (**SPADs**), superconducting nanowire single-photon detectors (**SNSPDs**) and spectrometers. Both **SPADs** and **SNSPDs** detect single photons and can be used in time and correlation measurements when linked with a time-correlated single-photon counting (**TCSPC**) module. However, unless spectral filtering is used before the detectors, they are unable to provide any frequency information about the detected photons. The spectral properties of the emitted photons are measured through use of a **CCD** camera mounted to a spectrometer.

SPADs use silicon avalanche photodiodes to detect single photons. However, **SPADs** differ from standard avalanche photodiodes (**APDs**). Both **APDs** and **SPADs** are p-n diodes that operate in reverse bias. **APDs** operate below the breakdown voltage of the diode. Therefore, a photon input creates a voltage output that scales linearly with the intensity of the input. **SPADs** operate above the breakdown voltage. This means that they are unstable so a single photon input can trigger a breakdown event, producing a large voltage signal. This property means that **SPADs** operate in “Geiger” mode and are used as counters, whereas **APDs** can be used to measure intensity. The voltage pulse output of the **SPAD** is passed to a Stanford Research Systems SR400 gated photon counter or a Becker & Hickl SPC-130EM **TCSPC** module to be recorded. The

SR400 is used for photon counting and time-binning detection signals. The Becker & Hickl is used for time-binning and correlation measurements.

SNSPDs are also used as single-photon counters. The operation principle of a **SNSPD** is the change in resistivity that occurs when a photon reaches the nanowire detector. The optical fibre input is seated above a superconducting nanowire that meanders back and forth, creating the equivalent of a large detection surface area. The nanowire is held at 2.5 K by a liquid helium continuous flow cryostat system. The low temperature is achieved through use of a lambda point refrigerator by pumping on the liquid helium reservoir within the detector. The **He** reservoir is replenished from a liquid **He** dewar that the detector is mounted above. A constant current is then applied to the nanowire. When a single photon is absorbed in the nanowire, the conditions required for superconductivity are broken, creating a voltage pulse. In experiments the voltage pulse is passed to a **TCSPC** to be recorded.

The spectrometer used is a 0.75 m single grating Princeton Acton SP2750, the schematic of which is shown in Figure 3.3. The separated spectrum is measured on a liquid nitrogen cooled **CCD** (Princeton PyLoN 400BR) which operates at -120°C . The spectrometer has three different diffraction gratings: a 600 l mm^{-1} , 1200 l mm^{-1} and a 1800 l mm^{-1} . In the following measurements only the 1200 l mm^{-1} grating is used, due to its higher efficiency at $\sim 900\text{ nm}$ compared to the 1800 l mm^{-1} grating. The 1200 l mm^{-1} grating gives a spectrometer resolution of $\sim 30\text{ }\mu\text{eV}$. The wavelengths of the spectra measured by the spectrometer are calibrated through use of a Neon-Argon lamp. The spectrometer can also be used as a spectral filter. A movable diverting mirror before the **CCD** allows the spectrally separated emission to be directed out of a slit in the side of the spectrometer where it can then be recoupled into a single-mode fibre. As a spectral filter, the spectrometer has a bandwidth of $\sim 97\text{ }\mu\text{eV}$, dependent on the width of the exit slit and the coupling back into the fibre.

3 Experimental Methods

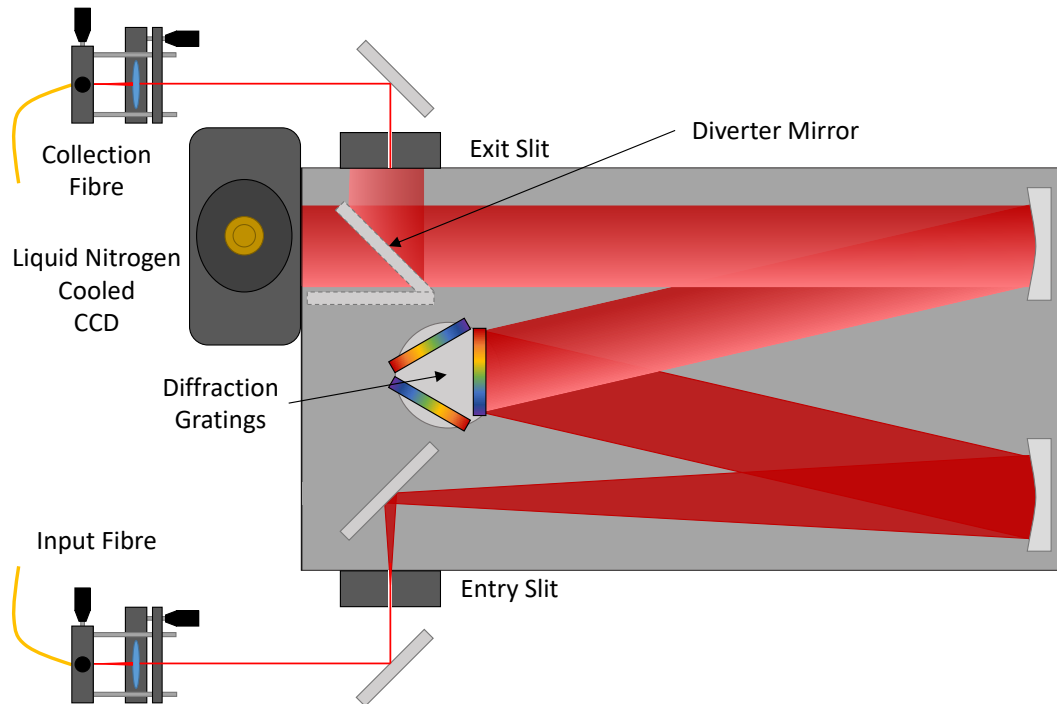


Figure 3.3: Schematic of 0.75 m Princeton Spectrometer. The diffraction grating turret contains three gratings: 600 l mm^{-1} , 1200 l mm^{-1} , and 1800 l mm^{-1} . For the following experiments only the 1200 l mm^{-1} grating is used. The separated spectrum is recorded by a liquid nitrogen cooled CCD. A diverting mirror before the CCD allows the spectrometer to also be used as a spectral filter by directing the beam out of the spectrometer where it can then be fibre coupled.

3.7 Calibrating Excitation Power

When running quantum-optics measurements, it is important to be able to calibrate the laser excitation power with the state of the QD system. This section describes the calibration methods used under both pulsed and CW excitation schemes.

3.7.1 Pulsed Pi power

Pulsed excitation power is calibrated by measuring Rabi rotations to find π -power. Rabi rotations are used to calibrate the excitation power that is required for the population of the QD to be found in the excited exciton state after the application of a laser pulse. Exciting a transition with strong CW excitation causes the population to oscillate between the ground ($|0\rangle$) and excited ($|X\rangle$) state at the Rabi frequency (Ω_R). This is called Rabi flopping and leads to the probability of finding the QD in the $|0\rangle$ or $|X\rangle$ state being given by [47]:

$$\begin{aligned} |c_0(t)|^2 &= \cos^2(\Omega_R t/2), \\ |c_X(t)|^2 &= \sin^2(\Omega_R t/2). \end{aligned} \quad (3.1)$$

As the population is time dependent, if the excitation laser ends at a time multiple of $n\pi/\Omega_R$ where n is an odd integer then the population will be in the $|X\rangle$ state. If n is an even integer, then the population is in the $|0\rangle$ state. This process can therefore be applied to pulsed driving of the transition where the length of the excitation pulse determines the final state of the population after the application of the pulse. However, the Rabi frequency depends on the strength of the applied pulse. Therefore, the final population after the pulse depends on both the Rabi energy and the pulse length. It is useful to define the excitation by the pulse area (Θ):

$$\Theta = \int_{-\infty}^{+\infty} \Omega_R(t) dt, \quad (3.2)$$

to relate both the length of the pulse and the rabi frequency. Here the pulse area is a dimensionless parameter defined in terms of π .

Experimentally, it is easier to adjust the power of the laser pulses than the pulse length. π -power is therefore found by measuring a power dependence of the RF. When a pulse with an area of π is applied, the QD is promoted to the $|X\rangle$ state if it started in the $|0\rangle$ state. The QD then decays back to the ground state via radiative

3 Experimental Methods

decay. If the QD starts in the $|0\rangle$ state and interacts with a 2π pulse, then the population will be rotated to the $|X\rangle$ state and back to the $|0\rangle$ state by the pulse. As the QD ends in the $|0\rangle$ state, there is no radiative decay of the population, and so no RF is detected. This creates an oscillating emission signal which continues with increasing pulse area. This is known as a Rabi rotation and has been observed for QDs in different systems [135–138]. An example of a Rabi rotation measured using the QD sample described in Chapter 4, with the associated π -pulses labelled, is shown in Figure 3.4.

To determine the π -power of the system, the QD is excited resonant to the neutral exciton using the shaped pulses from the Mira Ti:S laser. The QD emission is then detected on either the spectrometer or on a SPAD. The excitation laser power is increased in increments and at each new power a spectrum or the emission intensity is recorded. To analyse the spectra from the spectrometer, the intensity recorded at the wavelength corresponding to the exciton peak is extracted and plotted against the excitation power. The data includes a background from the reflected excitation laser which increases linearly with excitation power. To remove this, the data is fitted with a linear fit. The gradient of the fit is used to remove the background and the data is replotted against the square root of the excitation power. An example of a Rabi rotation measured using this method can be seen in Figure 3.4, the peaks and troughs have been labelled with their corresponding π values.

A similar method is used when measuring Rabi rotations using a SPAD. However, as SPADs do not record any spectral information, the QD emission is filtered around the zero-phonon line (ZPL) to remove the excitation laser when using short pulses, as well as to remove emission from other transitions. The same method of applying a linear background is used to analyse the Rabi rotation. To improve the accuracy of the measured π -power, these measurements can also be performed using a differential measurement scheme. After each spectra or intensity is recorded, a different bias is applied to the sample to move the neutral exciton transition out of resonance

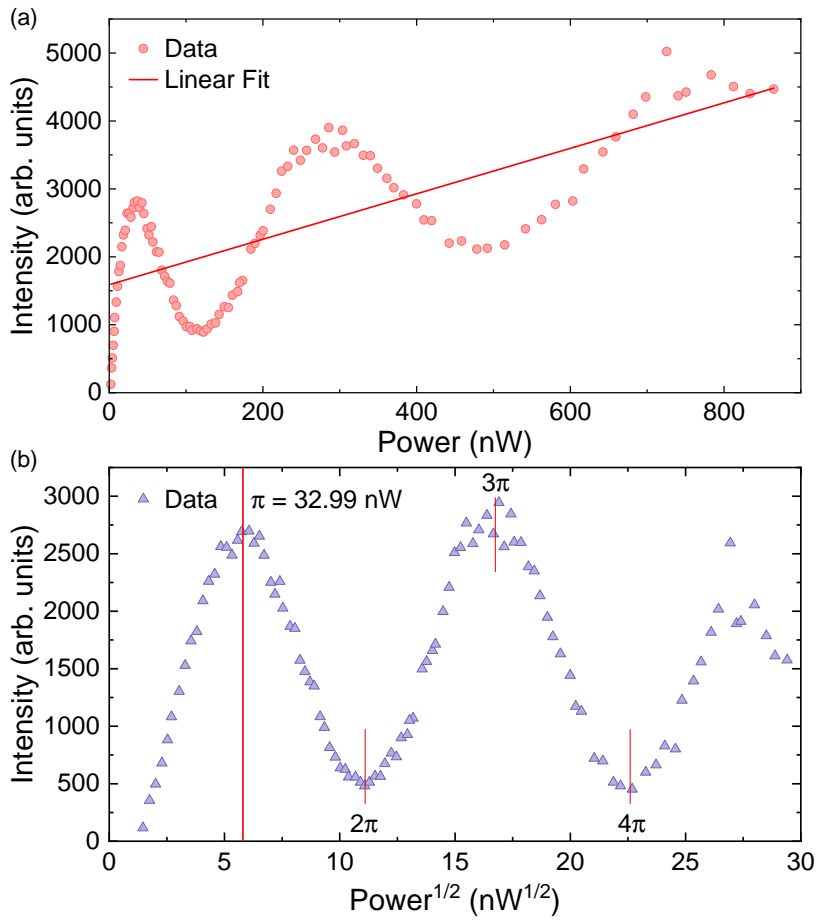


Figure 3.4: An example of a Rabi rotation measured to calibrate the pulsed excitation power. (a) Here, the spectrometer is used to measure the intensity of the unfiltered neutral exciton peak against excitation power. A linear background that increases with increasing excitation power is fitted to the data. (b) The gradient of the linear background is used to remove the laser background and the data is replotted against the square root of the excitation power. The peaks and troughs have been labelled with their corresponding π values.

3 Experimental Methods

with the excitation laser. A background spectra or emission measurement is then recorded. By subtracting the background away from the resonant data, the increasing background from the emission laser can be removed from the Rabi rotation data.

As well as being used as a method to calibrate excitation power, Rabi rotations can also be used when optimising the alignment of the system. A high π -power indicates that the laser is not well coupled to the QD system, whereas a low collected emission intensity at π -power is an indication that the emission collection path is not well aligned.

Recently, Monte Carlo simulations of two-level emitters (TLE) investigating the effect of multi-photon emission when using long pulses (relative to T_1) have shown that the maximum RF intensity occurs at a pulse area slightly higher than π [139, 140]. The multi-photon emission can also cause an increase in the RF emission of the 3π peak above that of the π peak [139].

3.7.2 CW Pi Power

Calibrating the CW excitation laser power utilises the Mollow triplet splitting caused by the dressing of the levels by the laser. As described in Section 2.3.2, when driving a TLE resonant to the neutral exciton transition, the “bare” ground and excited states become “dressed” and split by $\hbar\Omega_R$. This leads to four possible energy transitions. However, as two of the transitions are degenerate a Mollow triplet forms with the side peaks separated from the central peak by $\hbar\Omega_R$. An example of a Mollow triplet measured (black line) at an excitation power of 10 μW is shown in the inset of Figure 3.5.

To calibrate the CW excitation power a power dependence of the Mollow triplet is measured. As Ω_R is increased, the side peaks move further away from the central peak. The three peaks of the Mollow spectra at each power are fitted with Voigt func-

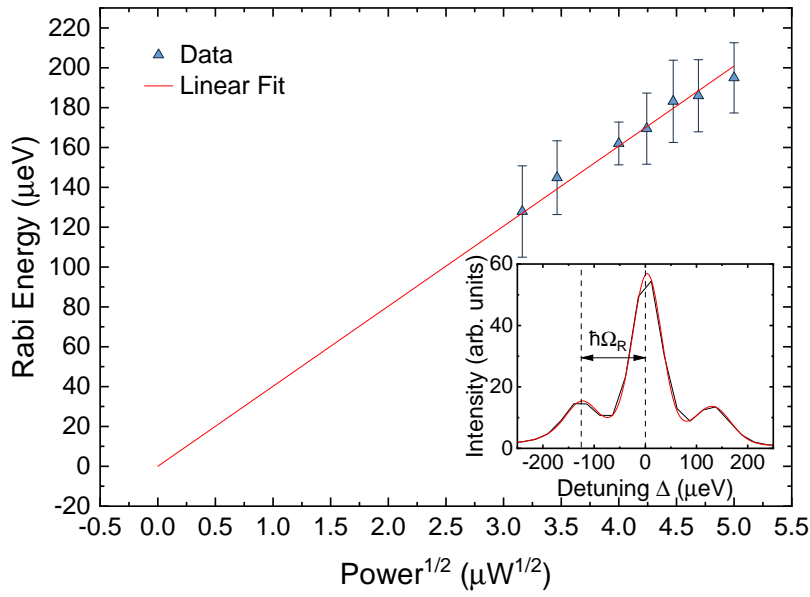


Figure 3.5: An example of a **CW** excitation power calibration measurement. The Rabi energy is measured as a function of the square root of the excitation power by fitting Mollow triplet spectra. By applying a linear fit, the **CW** excitation power required for a desired Rabi energy can be calculated and vice versa. *Inset:* Mollow triplet spectrum (black) measured at an excitation power of 10 μW, fitted (red) using a multiple peak Voigt function.

tions using a multiple peak fit, as shown by the red line in the inset of Figure 3.5. The difference between the side peaks and the central peak is found and converted from nanometres to electron volts. The excitation laser intensity has a square dependence to the triplet separation as the electric field increases in proportion to the intensity squared. By plotting the splitting against the square root of the power, as shown in Figure 3.5, a linear dependence can be fitted. The linear fit is constrained to pass through the origin, as the Rabi energy is zero when no field is applied, and can then be used to find the Rabi power of any applied **CW** laser power and vice versa.

4 Sample

This chapter contains the details of the sample used for the measurements in this thesis, including the composition of the semiconductor wafer and the fabrication method of the photonic crystal structure. In addition, there is a summary of the previous characterisation work performed on the sample.

4.1 Wafer

The sample used has **InGaAs QDs** grown within a *p-i-n* diode wafer. The construction of the wafer is shown in Figure 4.1. The wafer used was part of the VN2668 wafer grown by Dr Edmund Clarke at the EPSRC National Epitaxy Facility at the University of Sheffield. Self-assembled **InGaAs QDs** are grown on a **GaAs** substrate via **MBE** using the Stranski-Krastanow method described in Section 2.2.2. The **QDs** were grown using the In-flush technique that allows the control of the **QD** height [141]. For VN2668 the **QDs** were capped with 2.5 nm of **GaAs** before the In-flush, setting their height to this value. Tunnelling electron microscope (TEM) work carried out by Dr Maxime Hugues on similar In-flush **QD** wafers indicates a **QD** diameter of 15-20 nm.

The **QD** layer is surrounded, above and below, by undoped 50 nm thick **AlGaAs** tunnelling barriers. The barriers reduce the ease with which charges can tunnel into or out of the **QD** layer, increasing the stability of the charge environment and so allowing a large **QCSE** tuning range of the **QD** emission [75, 142]. Either side of the barriered **QDs** are the doped semiconductor layers that form the *p-i-n* diode. The top

4 Sample

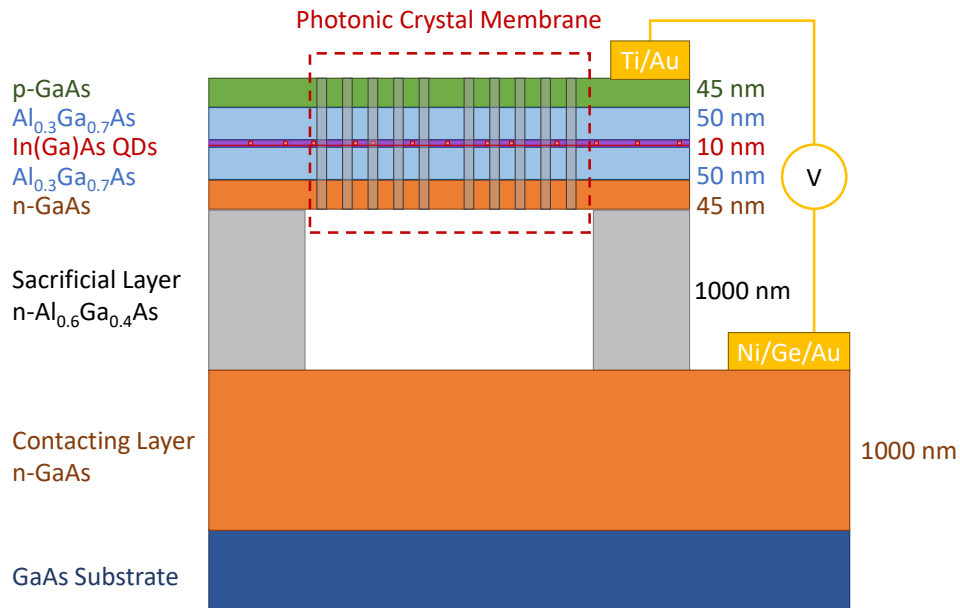


Figure 4.1: Schematic cross-section of the QD semiconductor wafer. The sample uses a *p-i-n* diode design, incorporating AlGaAs barriers for charge stability and an increased QCSE tuning range.

layer is GaAs *p*-doped with Beryllium whereas the bottom layer is GaAs *n*-doped with Silicon. Both of these doped layers are 45 nm thick.

Beneath the diode is a 1 μm thick sacrificial layer of *n*-doped AlGaAs. This layer is selectively removed during sample fabrication to leave a free-standing structure that is supported from the edges. Below the sacrificial layer there is a 1 μm thick contacting layer made of *n*-doped GaAs. The contacting layer and the *p*-doped GaAs layer at the top of the diode are connected via Gold bond wires to connections on the sample holder, allowing a voltage to be applied to the diode. The wafer was grown from the bottom up via MBE on a GaAs substrate.

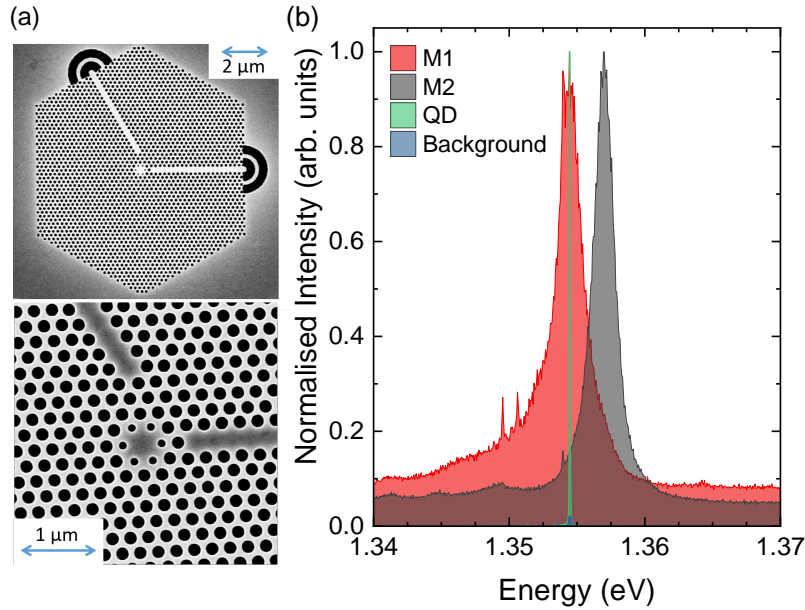


Figure 4.2: (a) SEM images of the sample used in this thesis, showing a H1 PhCC with coupled W1 waveguides. The SEM images were taken by Dr Ben Royall. (b) The H1 cavity displays two orthogonally polarised linear modes, labelled M1 and M2, measured using above-band excitation. RF is used to acquire a spectrum of the QD (green) that is used throughout this thesis, along with the background suppression possible (blue) using the cross-polarisation method described in Section 3.4.

4.2 Design

The photonic crystal structure fabricated on this wafer was a H1 PhCC with two coupled W1 waveguides. Scanning electron microscope (SEM) images of the complete cavity structure are shown in Figure 4.2(a). Before fabrication the structure design was optimised by Dr Rikki Coles [113, 121].

The SEM images of the cavity show that the ring of etched cylinders closest to the cavity have a reduced radius and are displaced when compared to the remainder of the PhC lattice. These modifications are used to improve the Q -factor of the cavity [122].

4 Sample

A pair of etched cylinders above and below the cavity are shifted with respect to the PhC to lift the degeneracy of the cavity modes [143]. The sample design is also optimised so that each W1 waveguide couples to one of the orthogonal linearly polarised cavity modes [121]. The two modes of the cavity are shown in Figure 4.2(b) labelled M1 and M2. To measure the cavity modes the sample is excited above the cavity using above-band excitation from the Thorlabs 808 nm CW laser. The emission, also collected from above the cavity, is maximised for each mode by rotating the linear polariser in the collection path. The collection polarisations used to measure each mode in Figure 4.2 are orthogonal. By fitting the cavity modes with Lorentzian peaks the Q -factors of the modes can be evaluated using Equation 2.8. These are found to be 539 and 764 for the M1 and M2 modes, respectively. These values are smaller than the Q -factors predicted using finite-difference-time-domain (FDTD) computational methods when optimising the H1 PhCC structure which predicted a Q -factor of 30,000 and a mode volume (V_m) of $0.39(\lambda/n)^3$ [121, 122]. However, the simulated Q -factor does not include coupling to the W1 waveguides.

To measure the coupling efficiency of the cavity modes to the W1 waveguides the sample also included H1 cavity structures without waveguides. When the sample was initially characterised the Q -factors of H1 cavities without waveguides were also measured. These were found to have a typical Q of 2400. Therefore, they also have a much lower Q than was simulated, indicating that the low Q comes from imperfect fabrication or absorption from the Beryllium doping in the wafer [121, 143], rather than just increased coupling of the cavity to the waveguides. By comparing the H1 cavities with and without W1 waveguides the coupling efficiency into the waveguides was found to be $\sim 36\%$ which is also lower than the simulated 89% [121].

By coupling to separate cavity modes, the two W1 waveguides can be used to selectively excite or collect from a single cavity mode. Previous work with this sample

has demonstrated their use for exciton spin readout [121] and for the routing of single photons [142]. At the end of the waveguides Bragg ($\lambda/2n$) grating out-couplers [144, 145] are used to direct the emission from the waveguides vertically so it can be collected using the optical set-up described in Section 3.4. Light can also be collected from above the cavity where FDTD simulations show that the majority of the light is emitted into an angle of less than 20° , allowing collection by the 0.55 NA cryostat lens.

To fabricate the sample the PhC structure was defined on the wafer using Electron Beam Lithography (EBL) and then etched using Inductively Coupled Plasma (ICP). After etching, the sacrificial AlGaAs layer beneath the device is removed using 40% Hydrofluoric Acid (HF). As is shown schematically in Figure 4.1, removing the sacrificial layer leaves the PhCC structure as a suspended membrane supported from the edges. The sample was fabricated by Dr Ben Royall at the EPSRC National Epitaxy Facility at the University of Sheffield. The PhCC structures are fabricated within diodes with 20 structures per diode. The sample is mounted on a TO-5 header to provide the electrical connections necessary within the cryostat.

4.3 Characterisation

All of the experimental work in this thesis was performed using a single cavity-coupled QD. Figure 4.2(b) shows an RF spectrum of the neutral exciton transition of the QD (green) along with an example of the laser background suppression (blue) possible using the RF set-up described in Section 3.4. The background suppression is measured by changing the bias applied to the *p-i-n* diode and so moving the QD out resonance with the excitation laser by the QCSE.

The tuning range of the QD neutral exciton emission achieved by the QCSE is shown in Figure 4.3. Here, the sample is excited using an above-band CW laser and spectra are recorded and plotted as a function of applied bias. Whereas in Figure 4.2(b) the

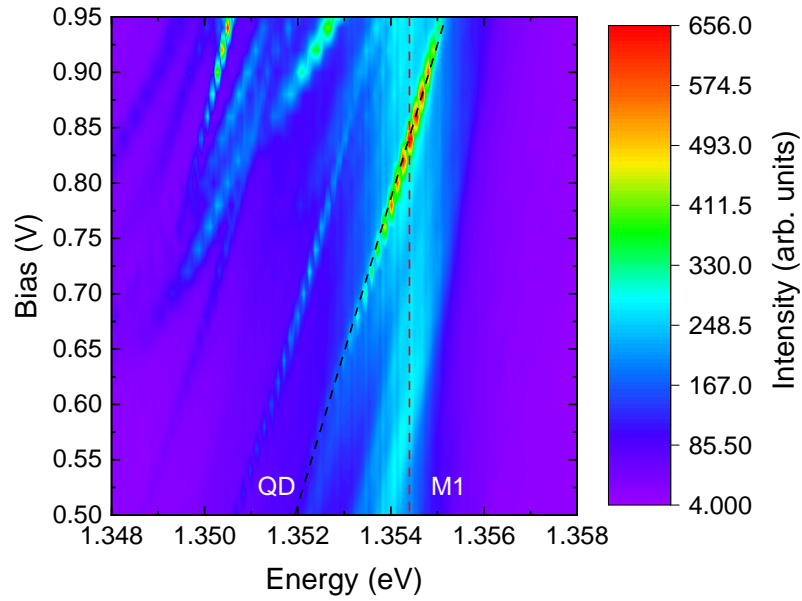


Figure 4.3: Bias dependent measurement using above band CW excitation. Spectra of the μ -PL at each applied bias are recorded. The dashed lines are a guide to the eye for the neutral exciton emission (black) and the M1 cavity mode (red). The measurement was performed by Dr Alistair Brash.

sample was saturated by the above-band excitation laser, here the sample is excited at lower powers, so that the QD emission can be resolved. The dashed black line follows the QD neutral exciton emission as it is tuned across the M1 cavity mode (red dashed). As the exciton crosses the cavity mode an enhancement of the emission is observed, due to the Purcell effect, showing that the exciton transition is weakly coupled to the M1 mode of the cavity. The observed enhancement of the emission occurs as the Purcell effect shortens the lifetime (T_1) of the exciton emission, allowing a faster re-excitation rate. A strong Purcell effect is observed despite the low Q -factor of 539 measured for the M1 cavity mode as it retains a small mode volume of $0.63(\lambda/n)^3$. The mode volume was calculated from FDTD simulations using parameters from the fabricated sample, rather than the ideal mode volume calculated for the optimised H1 PhCC [106, 121]. The measurement shown in Figure 4.3 was performed by Dr Alistair Brash.

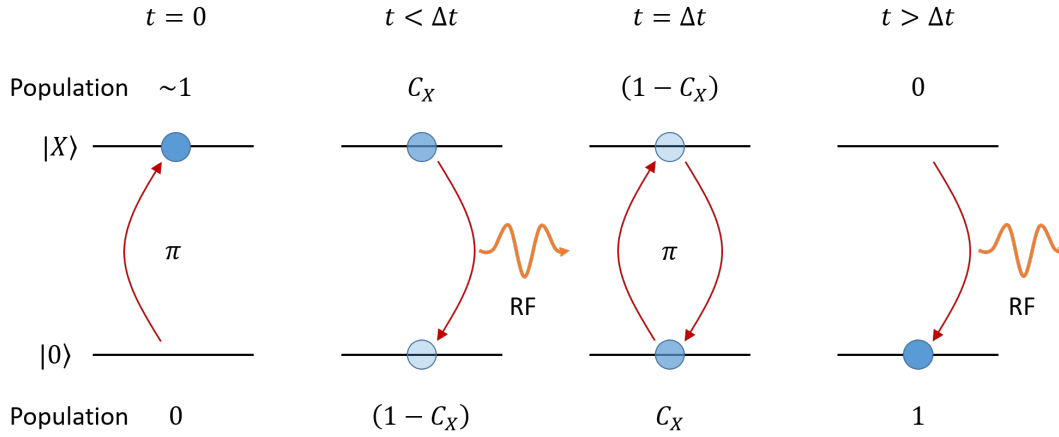


Figure 4.4: Illustration of the double π -pulse resonance fluorescence technique used for high resolution lifetime measurements.

The Purcell factor (F_p) for the cavity coupled QD was calculated by measuring the exciton T_1 along with the radiative lifetime of the QD ensemble (T_1') on the wafer away from the cavity and using Equation 2.11. However, the enhancement of the exciton T_1 meant that it was unresolvable on the fastest single-photon avalanche diode (SPAD) available. To achieve higher timing resolutions, a double π -pulse resonance fluorescence (DPRF) method was developed by Dr Alistair Brash, Dr Luis Martins and Dr Feng Liu. This method relies on the properties of π -pulses which are discussed in Section 3.7.1.

Figure 4.4 illustrates the principle of the DPRF technique. The exciton transition is treated as a two-level emitter (TLE) with its starting population in the ground state ($|0\rangle$). At $t = 0$, the application of a π -pulse drives the population to the excited state ($|X\rangle$), leaving $|X\rangle$ with a population of ~ 1 . After the first π -pulse the population of $|X\rangle$ can decay by spontaneous emission, emitting an RF signal. Therefore, at $t > 0$, the populations of $|X\rangle$ and $|0\rangle$ can be defined as C_X and $(1 - C_X)$ respectively. A second π -pulse is then applied to the system at $t = \Delta t$, exchanging the $|0\rangle$ and $|X\rangle$ popula-

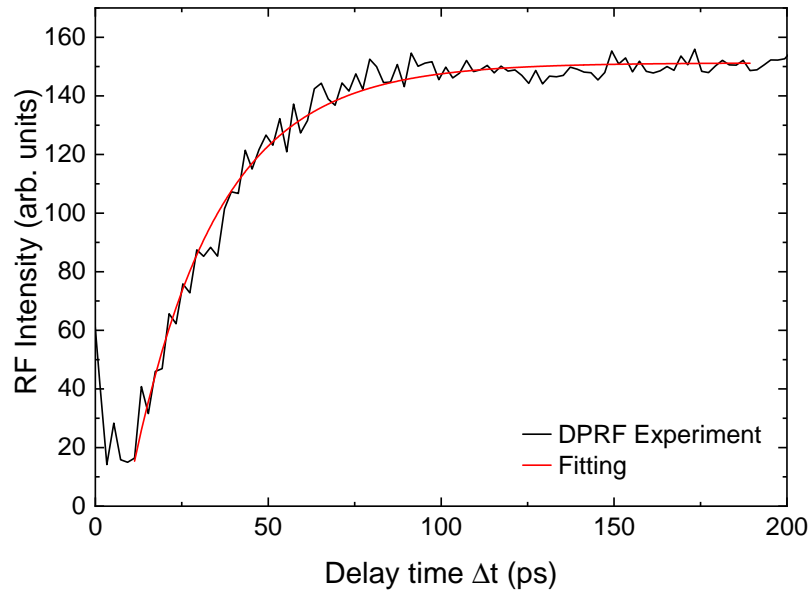


Figure 4.5: Double π -pulse resonance fluorescence results (black) where the RF intensity is a function of the delay between the two π -pulses. The curve is fitted (red) with an exponential function to give the radiative lifetime of the neutral exciton. These measurements were performed by Dr Feng Liu, Dr Alistair Brash and Dr Luis Martins.

tions. The $|X\rangle$ population can then decay again via spontaneous emission emitting a second RF signal. For both relaxation events, the emitted RF signal is proportional to $(1 - C_X)$. After the TLE has relaxed back to $|0\rangle$, the pulse cycle is repeated. The RF is recorded over many pulse cycles as the population change is a probabilistic event.

By changing the time between the π -pulses (Δt), the change in RF intensity can be mapped out in time, the results of which are shown in Figure 4.5. An exponential increase in the RF is seen, until the signal saturates at $\Delta t \gg T_1$. This increase can be explained by considering the system at the two limits of Δt . When $\Delta t \ll T_1$, $(1 - C_X)$ is small due to the low probability that there has been any spontaneous emission. The small $(1 - C_X)$ leads to a weak RF signal. In simple terms, the first π -pulse inverts the

system, and the second returns it to the ground state before spontaneous emission has occurred. Hence, no photons are emitted. At $\Delta t \gg T_1$, $(1 - C_X)$ tends to 1 as the majority of the population will have decayed from the $|X\rangle$ state. The second π -pulse returns this population to $|X\rangle$, allowing a second decay of the large $(1 - C_X)$ population and so leading to a strong RF signal being measured. By fitting an exponential to the DPRF curve, T_1 is found to be 22.7 ± 0.9 ps, implying a Purcell factor of 43 ± 2 when Equation 2.11 is used with the $T_1' = 971 \pm 15$ ps measured for the QD ensemble. A more detailed description of this method and results can be found in Liu et al. [106] and the PhD thesis of Dr John O'Hara [139].

To show that the transition being studied is the neutral exciton, fine-structure splitting (FSS) of the state is measured. The FSS is measured by exciting the QD with above-band CW excitation and the QD emission is tuned, by the QCSE, to lie between the two cavity modes. The linear polariser in the collection path is rotated in 10° steps, with spectra being taken at each step. The resulting spectra are fitted with Gaussians to find the central wavelength of the emission and plotted against the angle of the collection polariser. The resulting FSS is plotted in Figure 2.5, showing a splitting of 0.013 nm (19 μ eV).

5 Cavity-Coupled QD as a Single-Photon Source

This work was included in the following publication:

Feng Liu, Alistair J. Brash, John O'Hara, Luis M. P. P. Martins, **Catherine L. Phillips**, Rikki J. Coles, Benjamin Royall, Edmund Clarke, Christopher Bentham, Nikola Prtljaga, Igor E. Itskevich, Luke R. Wilson, Maurice S. Skolnick and A. Mark Fox. "High Purcell factor generation of indistinguishable on-chip single photons." *Nature Nanotechnology* **13**, 835-840 (2018).

Hanbury Brown and Twiss and Hong-Ou-Mandel second-order correlation measurements were set up and carried out by Catherine Phillips and Alistair Brash. Master-equation modelling of multi-photon emission was performed by John O'Hara.

5.1 Introduction

Single photons are desirable for many quantum-optics applications including boson sampling [27, 28], single-photon fast optical switching [29], photonic cluster state generation [30, 146], a quantum internet [2, 31, 32], optical quantum computing [4] and quantum cryptography [2] to mention just a few. All of these uses for single-photons require certain properties from their single-photon source (SPS). They need to be bright, pure, on-demand and indistinguishable [33, 34]. A SPS that is bright has a short emitter lifetime and so can be re-excited at a fast rate. To be bright they also require a high collection efficiency. The purity of a SPS involves measuring the pho-

5 Cavity-Coupled QD as a Single-Photon Source

ton statistics of the emission. Purity is defined as the probability that the output comprises single photons rather than multi-photon emission. On-demand is the probability that an input will create the desired output, i.e. that every excitation event results in a single photon being emitted rather than no emission or multi-photon emission. Indistinguishability, also known as visibility, is the probability that the single photons emitted are identical to each other.

In this chapter the purity and indistinguishability of the single-photon emission from a QD in an H1 PhCC is investigated using second-order correlation measurements. Hanbury Brown and Twiss measurements are used to investigate the single-photon purity of the emission from the neutral exciton of the QD and Hong-Ou-Mandel experiments are used to investigate the indistinguishability of the single-photons produced. These measurements are performed under pulsed excitation where the QD is excited resonantly using a π -pulse, as required for optimal on-demand operation. The effect of pulse length is also investigated, using a pulse width that is relatively long compared to the T_1 of the QD and a pulse width that is much shorter.

5.2 Second-Order Correlation Measurements

Correlation function measurements can be used to classify the temporal coherence properties of an emitter and its photon statistics [47]. The first-order correlation function ($g^{(1)}(t)$) is so named as it quantifies the properties of the first power of the electric field through field-field correlations. The second-order correlation function ($g^{(2)}(t)$) quantifies intensity-intensity correlations, intensity being the square of the electric field. This Chapter will discuss second-order correlations. First-order correlations will be discussed in more detail in Chapter 6. Second-order correlation ($g^{(2)}(t)$) measurements are used to measure the photon statistics of light emission. They are also used to measure the indistinguishability of the photons produced. Both of these properties are important for SPSs and are quantified using Hanbury Brown

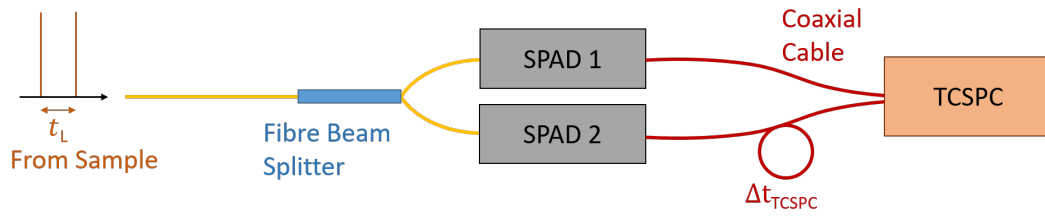


Figure 5.1: Schematic of the fibre-based set-up used for Hanbury Brown and Twiss measurements: yellow lines - optical fibres, red lines - coaxial electrical cables. A 50:50 fibre beam splitter is used to split the QD emission equally to two single-photon avalanche diodes (SPADs) which are connected to a time-correlated single-photon counting module (TCSPC). The electrical delay (Δt_{TCSPC}) centres the time-zero of the TCSPC correlation scan in the centre of the measurement window.

and Twiss (HBT) and Hong-Ou-Mandel (HOM) measurements, respectively. The details of these measurements are discussed in this section.

5.2.1 Hanbury Brown and Twiss

The Hanbury Brown and Twiss (HBT) experiment is a $g^{(2)}(t)$ correlation measurement that is used to measure photon statistics [147]. The experimental set-up for a fibre-based HBT measurement is shown in Figure 5.1. Collected emission from the sample passes through a 50:50 fibre beam splitter onto two single-photon avalanche diodes (SPADs). The SPADs are connected by coaxial cables to a time-correlated single-photon counting module (TCSPC). The TCSPC time tags detection events from the SPADs using a reversed start-stop configuration. The TCSPC has two channels: “CFD” and “Sync”. When a detection start-event occurs on the “CFD” channel the TCSPC starts measuring time. The timer stops either when a detection stop-event occurs on the “Sync” channel or if the time period becomes longer than the range of the TCSPC’s internal Time-to-Amplitude Converter (TAC). In the first case the arrival time of the second photon is plotted on a histogram, in its associated time bin, and the

5 Cavity-Coupled QD as a Single-Photon Source




$g_{HBT}^{(2)}(0)$	Photon statistics	Photon distribution (\longrightarrow time)
> 1	Bunched	
1	Coherent (random)	
< 1	Antibunched	

Table 5.1: Definition of the photon statistics of light with respect to $g_{HBT}^{(2)}(0)$. The photon distribution shows examples of photon streams in time that would create the associated photon statistics.

TCSPC's internal clock is reset to begin measuring again with the next "CFD" trigger. In the second scenario, the internal clock is reset and waits for the next trigger. Extra electrical delay (Δt_{TCSPC}) is added before the "Sync" channel to centre time-zero in the TAC window. Time-zero is used to define the time where the added delay means that for the TCSPC it is the equivalent of looking at both SPADs simultaneously. For example, if a 5 ns delay is added to "Sync" then a photon detection stop-event occurring at 5 ns on that channel would have originated from the same photon pulse start-event that triggered the "CFD" counter 5 ns previously, this is known as a coincidence event. One metre of coaxial cable is equivalent to about a 5 ns time delay.

Figure 5.2 shows an illustration of the results for HBTs where the sample is excited by a pulsed laser. The time-zero peak is centred in the measurement window and each of the correlation peaks are separated by the pulse separation of the laser (t_L), arbitrarily chosen here to be 10 ns. Considering the photons emitted from a source, in this case a QD, their emission statistics can be split into three categories: bunched, coherent and antibunched. These statistics are shown in Table 5.1. The $g_{HBT}^{(2)}(0)$ for pulsed excitation is calculated from the area of the $g_{HBT}^{(2)}(t)$ correlation peak (A_{t0}) at time-zero (Fig. 5.2 - green/purple/grey) normalised to the averaged area of the surrounding peaks (A_{mean}) in the HBT (Fig. 5.2 - blue) using:

$$g^{(2)}(0) = \frac{A_{t0}}{A_{mean}}. \quad (5.1)$$

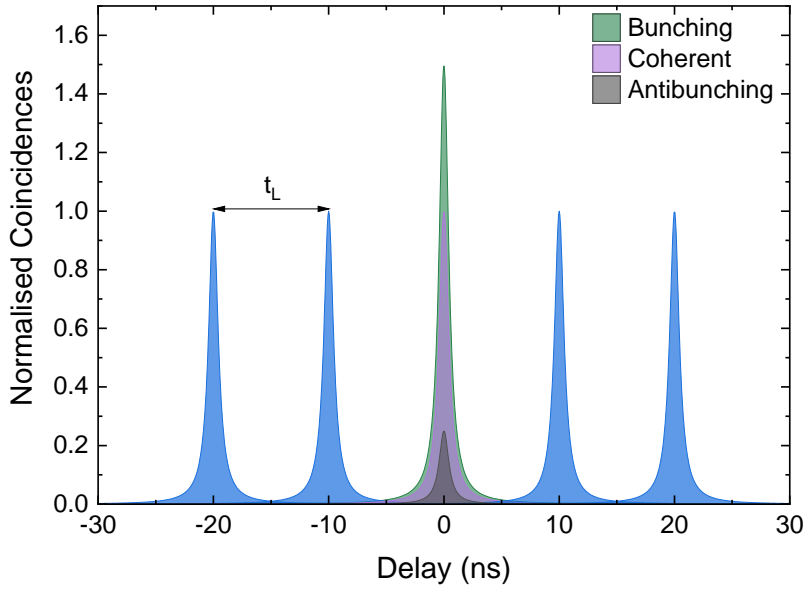


Figure 5.2: Illustration of pulsed excitation HBTs where t_L is the separation of the excitation laser pulses, here chosen arbitrarily to be 10 ns. The centre peak is time-zero. The area of this peak, normalised to the averaged areas of the surrounding (blue) peaks, gives $g_{HBT}^{(2)}(0)$. The illustration shows examples of HBT results for bunched photon statistics (green) where the $g_{HBT}^{(2)}(0) > 1$, coherent statistics (purple) where $g_{HBT}^{(2)}(0) = 1$ and antibunched statistics (grey) where $g_{HBT}^{(2)}(0) < 1$.

Bunched photon statistics, defined as $g_{HBT}^{(2)}(0) > 1$, is where the photons are emitted in groups (bunches). This means that, when one SPAD has been triggered, it is more likely that a second photon will be detected in a short time window than at a long time [47]. This leads to a peak above the coherent background level in HBT measurements, shown in green on Figure 5.2.

Coherent (random) photon statistics occur when the photons from the source are emitted randomly in time. Lasers are an example of coherent light sources. For a coherent light source $g_{HBT}^{(2)}(t) = 1$ at all values of time (t), as when measuring a HBT

5 Cavity-Coupled QD as a Single-Photon Source

there is an equal chance of detecting a coincidence at any time delay between the two detectors [47]. This is shown in purple on Figure 5.2, where the area of the time-zero coincidence peak has the same area as the surrounding coincidence peaks.

Antibunched photon statistics are seen when the source emits photons one at a time with a time separation of $\sim t_L$ between them, i.e. up to one photon is produced per excitation event. This is seen as $g_{HBT}^{(2)}(0) < 1$. If a single photon passes through a 50:50 beam splitter it can only take one path or the other. Therefore, when comparing detection events for both SPADs at the same time, a single photon cannot create a coincidence event. A source that produced only single photons would have a $g_{HBT}^{(2)}(0)$ of zero with the single-photon purity of the source being given by $1 - g_{HBT}^{(2)}(0)$. Figure 5.2 shows an antibunching peak in grey where the $g_{HBT}^{(2)}(0) = 0.25$. Therefore, the single-photon purity is 75%.

5.2.2 Hong-Ou-Mandel

The Hong-Ou-Mandel (HOM) second-order correlation measurement ($g_{HOM}^{(2)}(t)$) [148] is used to measure the indistinguishability of single photons produced. This is also known as the “Visibility” of the SPS. The HOM measurement has been used to show strong photon indistinguishability for QDs embedded in micro and nano-cavities [149–152]. Here, HOM measurements are made using a fibre-based Mach-Zehnder interferometer, the schematic of which is shown in Figure 5.3.

Each cycle of the experiment involves excitation by two π -pulses separated by $\Delta\tau$. This produces two photons separated by $\Delta\tau$ which then pass through a 50:50 fibre beam splitter. After the beam splitter the interferometer comprises a path where the polarisation of the photon can be modified and a path with an increased path length of Δt . The polarisation is controlled through use of a Phoenix Photonics “Electronic in-line fibre polarisation controller” which can move the polarisation to any point on the Poincare sphere by heating the optical fibre. The difference in path length is

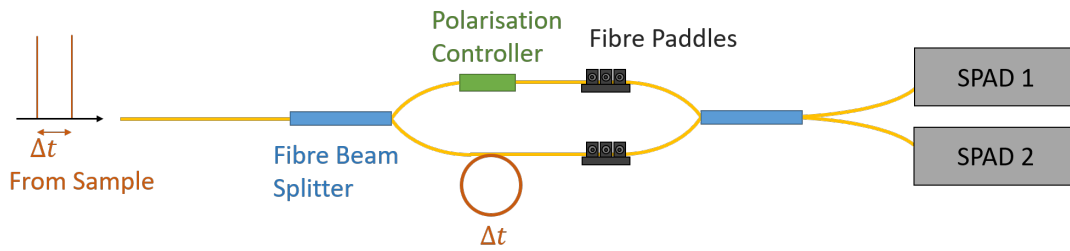


Figure 5.3: Schematic of the fibre-based Mach-Zehnder interferometer used for Hong-Ou-Mandel measurements. A 50:50 fibre beam splitter is used to separate the emission equally down both arms of the interferometer. One arm has an electrical polarisation controller, the other a fixed fibre delay (Δt) that matches the separation of the excitation pulses. The fibre paddles allow the polarisation of both arms to be identical at the second 50:50 fibre beam splitter where the emission is then split onto two SPADs. As in Figure 5.1 both SPADs are connected to a TCSPC and an electrical delay of Δt_{TCSPC} is added to one path.

achieved by increasing the length of fibre used on the opposite side of the interferometer to the polarisation controller.

The two paths of the interferometer then converge at a second 50:50 fibre beam splitter. Here, if two photons arrive with temporally overlapping wavepackets and are indistinguishable from each other, then they must take the same path out of the beam splitter [153]. This can be understood by considering Figure 5.4. Here, photons reflect off a 50:50 beam splitter which has a higher refractive index ($n = n_2$) than the surrounding medium ($n = n_1$). When light reflects from the surface of a medium with a higher refractive index it gains a π phase shift.

Before the beam splitter the state of the system can be written as $|1_A 1_B\rangle$ where one photon is incident on each port of the beam splitter, A and B. The state of the system

5 Cavity-Coupled QD as a Single-Photon Source

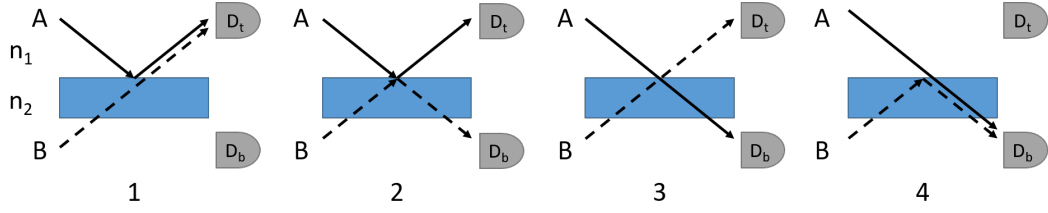


Figure 5.4: Diagram of the four different outcomes after two photons, incident on ports A and B, traverse a 50:50 beam splitter with $n_2 > n_1$. The output of each scenario is recorded on two detectors D_t and D_b .

after the beam splitter is a superposition of the four different possible paths:

$$1 + 2 + 3 + 4. \quad (5.2)$$

The four possible cases can be written in terms of each outcome by picturing two detectors to the right of the beam splitters in Figure 5.4, one above the beam splitter (D_t) and one below the beam splitter (D_b). Recording the possible amplitude (number of photons) and phase of the photons at each detector allows the superposition to be written as [154]:

$$|1_A 1_B\rangle = \frac{1}{\sqrt{2}}(-|2_t 0_b\rangle - |1_t 1_b\rangle + |1_t 1_b\rangle + |0_t 2_b\rangle).$$

The change in phase of the photon which follows the solid line in case 1 and case 2, due to $n_1 < n_2$, leads to the negative sign in each case. Significantly, cases 2 and 3 cancel in the case of indistinguishable photons, a manifestation of quantum interference. The final output state is therefore given by the superposition of cases 1 and 4, where both photons leave through one side of the beam splitter or the other. The bunching of the photons in either output path is the key characteristic of the HOM effect.

After the beam splitter are two SPADs. As for the HBT measurements, the SPADs are connected to a TCSPC to record coincidence counts from the two detectors. If two indistinguishable photons exit through the same port of the second beam splitter then no coincidence is counted at time-zero.

Indistinguishable photons only occur at the second beam splitter of the interferometer when both of the arms are co-polarised (\parallel) with respect to each other. Maximum distinguishability occurs when the two arms are cross-polarised (\perp). Indistinguishability (Equation 5.3) is given by the fraction of the area of the indistinguishable coincidence counts (A_{\perp}) at time-zero compared to the area of the distinguishable coincidence counts (A_{\parallel}) at time-zero:

$$V = \frac{A_{\perp} - A_{\parallel}}{A_{\perp}}. \quad (5.3)$$

Maximum indistinguishability would occur when no coincidence counts are recorded at time-zero for a co-polarised interferometer. This would give a visibility of 1 (100%).

As the Mach-Zehnder interferometer used for the [HOM](#) measurements is fibre-based, fibre paddles are used to co-polarise the two arms when initialising the interferometer. This then allows the electronic polarisation controller to change the polarisation between co and cross-polarised with an extinction ratio of $99.99 \pm 0.01\%$. The co-polarisation is achieved by connecting one of the exit fibres from the second fibre beam splitter to a fibre-to-fibre u-bench, which adds a short free-space path between two optical fibres, before the fibre-coupled [SPAD](#). A rotatable linear polariser is mounted within the u-bench. An attenuated single mode [CW](#) laser with the same wavelength as the exciton emission from the [QD](#) is connected to the input of the interferometer. The time-delay arm of the interferometer is disconnected.

The linear polariser is then used to minimise the counts on the [SPAD](#) in the connected arm. Fibre paddles comprise three sections which are set with quarter-wave plate, half-wave plate and quarter-wave plate configurations, respectively. Used in conjunction with the polarisation controller, they further minimise the counts in the connected arm. This arm is then disconnected and the opposite arm of the interferometer is connected. The corresponding fibre paddles are used to minimise the [SPAD](#) signal without changing the angle of the linear polariser in the u-bench. When the

5 Cavity-Coupled QD as a Single-Photon Source

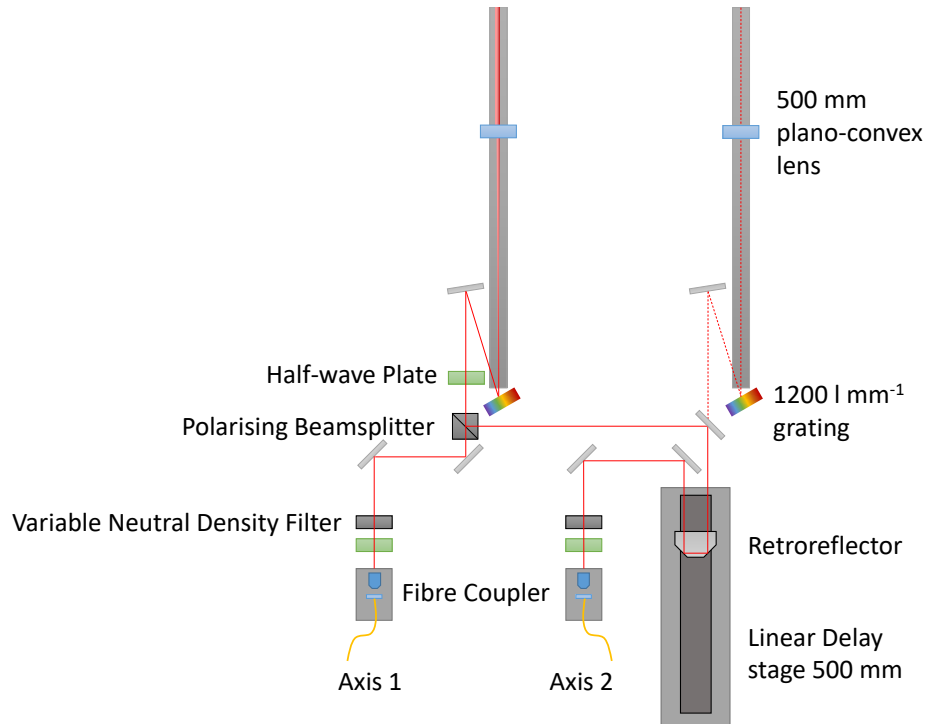


Figure 5.5: Schematic of the modified 4f pulse shaper used to perform HOM measurements. Identically shaped excitation laser pulses, separated by a time delay (Δt), are produced through the use of a polarising beam splitter after one of the pulse shapers. The second pulse shaper (dashed line) is not used.

transmission through the linear polariser of both arms is minimised, the two arms of the interferometer are now co-polarised. The values for the polarisation controller are noted and the delay-line arm is then disconnected again. Using only the polarisation controller, the transmission through the linear polariser is maximised, giving the polarisation controller values required for the two arms of the interferometer to be cross-polarised.

The sample is excited using the Mira Ti:S pulsed laser. The Ti:S has a 13 ns pulse separation (t_L). For consecutive photons to reach the second beam splitter simulta-

5.2 Second-Order Correlation Measurements

neously, the time delay (Δt) used in the Mach-Zehnder interferometer should be the same as the time delay between photons emitted from the sample. To change the time delay between the excitation laser pulses, the pulse shaping set-up shown in Figure 3.2 was modified to that of Figure 5.5. Here, all of the laser power travels through one pulse shaper by the rotation of the half-wave plate mounted in front of a polarising beam splitter before the pulse shapers, shown in Figure 3.2. Then, by using a second half-wave plate and polarising beam splitter after the pulse shaper, half of the beam is split and aligned through a free-space delay stage before being fibre coupled. Splitting the beam after the pulse shaper rather than before ensures that the shape of the two excitation pulses should be identical. The two excitation fibres (labelled Axis 1 and Axis 2 in Fig. 5.5) are then combined using a fibre beam splitter before travelling to the sample. Each laser pulse emitted now travels to the sample as two pulses separated by a time Δt , defined by the position of the linear delay stage.

The Δt of the Mach-Zehnder interferometer is created by adding an extra length of optical fibre to one arm. Two methods are used to find the position for the free-space delay stage so that the laser pulses also have a splitting of Δt . The first method involves measuring the arrival time of laser pulses at a SPAD after the Mach-Zehnder interferometer, bypassing the sample, using one axis of the pulse shaper at a time. The TCSPC is triggered each time the laser emits a pulse, through the use of the laser photodiode, and is set to “stop” when it receives a signal from the SPAD. This is a similar set-up to that of a lifetime measurement. Two peaks build up on the TCSPC histogram, one for each path through the interferometer with the two peaks separated by Δt . This is measured separately for both laser axes. For the free-space delay path of Axis 2 to match Δt , the Axis 1 laser pulse that travels down the delayed path in the interferometer and the Axis 2 laser pulse that travels down the short path of the interferometer should both reach the SPAD at the same time after the TCSPC has been triggered. The distance that the free-space delay stage needs to be moved can be calculated from the time difference between these two peaks. An example of this

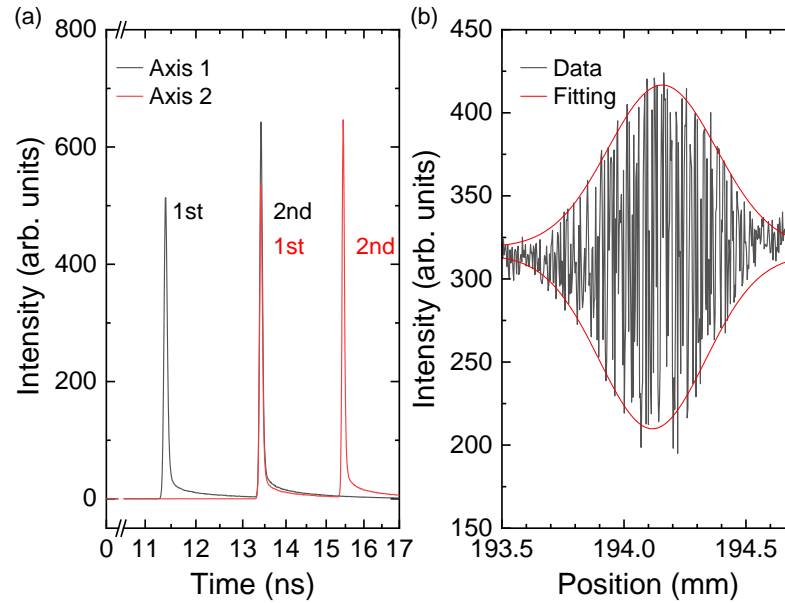


Figure 5.6: Setting the Δt of the linear delay stage in Axis 2: (a) Method 1: Using each laser axis in turn, through the interferometer to one SPAD. The laser photodiode is used to trigger the SPAD. The Axis 1 (black) peak through the delayed side of the interferometer (labelled 2nd) has the same time position as the Axis 2 (red) peak through the short side of the interferometer (labelled 1st) when the Δt of the interferometer and Axis 2 are identical. (b) Method 2: Interferometric measurements can also be used to find the Δt position of Axis 2 with higher time resolution. Both axes pass through the interferometer onto a SPAD. Maximum interference between the pulses, and so maximum intensity, occurs where the pulses arrive simultaneously at the second beam splitter of the interferometer.

measurement where the correct delay path length has been found is shown in Figure 5.6(a).

The second method to find the Δt position for Axis 2 is to use interferometry between the two laser pulses. This method has a higher time resolution as it is not sensitive to

the timing jitter of the detectors used. For this measurement, a single SPAD is again used after the Mach-Zehnder interferometer. Each laser axis is set to the same power and both are connected to the interferometer using a fibre beam splitter, bypassing the sample. The free-space delay stage in Axis 2 is then stepped and at each step the SPAD records the laser intensity. When the laser pulses from Axis 1 and 2 overlap, interference fringes are seen in the recorded intensity. By fitting the fringe envelope, the central position of the envelope with maximum interference can be found, giving a precise stage position for Δt . An example of the interference fringes seen is shown in Figure 5.6(b).

Method 2 is best used in conjunction with method 1 as there are multiple stage positions that can cause the laser pulses to overlap, but only one where the Δt of the stage is the same as the Δt of the interferometer. As very small steps of the delay stage (~ 0.003 mm) are needed to resolve the fringes, the first method can be used to find the rough position for the delay stage so that a high-resolution measurement can be made. Depending on the Δt required, it can be that the delay required for Δt cannot be reached over the length of the free-space delay stage. This can be rectified by adding additional optical delay fibre to Axis 1 or 2 before the sample if Δt is too short or long for the delay stage respectively.

5.3 Experiments

This section discusses the specifics of the methods used for the HBT and HOM $g^{(2)}(t)$ measurements along with their respective results.

5.3.1 Method: Hanbury Brown and Twiss

The sample is excited, resonant to the QD neutral exciton transition, above the cavity by a π -pulse. The method for calibrating π -power for pulsed excitation is described in Section 3.7.1. The emission is collected from an out-coupler using the cross-polarised

5 Cavity-Coupled QD as a Single-Photon Source

RF method described in Section 3.4. The collected emission passes through a fibre beam splitter to two SPADs that are connected by coaxial cables to a time correlated single-photon counting module (TCSPC), as shown in Figure 5.1.

The Mira Ti:S pulsed laser is used to excite the QD with a pulse separation (t_L) of 13 ns. Two different laser pulse lengths (τ_L) were used for the HBT measurements: 13 ps and 2.4 ps. The collected emission signal from using the 13 ps excitation pulse is unfiltered and has a signal-to-background ratio of $\sim 20:1$. As the 2.4 ps pulse is spectrally broader, the collected emission is filtered, centred on the QDs zero-phonon line (ZPL), using the spectrometer as a grating filter with a bandwidth FWHM of 96 μeV . Filtering eliminates the residual broadband scatter of the laser from the surface of the sample and a signal-to-background ratio of $\sim 50:1$ can be achieved. The filtering is necessary due to the out-of-plane excitation and collection geometry and the short waveguides of 5 μm in length, meaning that the excitation and collection spots are only 5 μm apart. This filtering would not be necessary for on-chip experiments as the background arises from scattering from the surface of the sample and is not coupled into the waveguide. HBT measurements were performed using SPADs with a quantum efficiency of $\sim 43\%$ at the cavity wavelength of ~ 915 nm. The $\tau_L = 13$ ps measurements were made using SPADs and photon counting card (TCSPC) with a combined IRF that is Gaussian in shape with a FWHM of ~ 860 ps. The $\tau_L = 2.4$ ps measurements were made with newer SPADs that have an IRF of ~ 340 ps when combined with the TCSPC.

The TCSPC is configured with a 50 ns delay window which corresponds to a histogram bin width of 48.9 ps. A 25 ns delay (5 m of coaxial cable) is added to one SPAD to centre the time-zero peak in the measurement window. The electrical delay can be checked by splitting the electrical signal from one SPAD so that both the short coaxial cable and delayed coaxial cable are connected to the same SPAD. Running a HBT in this set-up will result in strong coincidence peak at time-zero as the TCSPC

is triggering and stopping from the same SPAD signal separated at the TCSPC by the difference in length of the two coaxial cables. The length of the electrical delay can then be adjusted to centre time-zero in the centre of the measurement window.

The HBT measurements were repeated in cycles of 15 minutes. Due to the low count rate of $\sim 0.8\text{-}7$ kHz per channel on the TCSPC, the measurements were often run overnight. Using 15 minute cycles allowed the signal to background to be monitored and allowed for the removal of cycles where there had been time-dependent drifts such as changes in the laser suppression.

5.3.2 Results: Hanbury Brown and Twiss

Figure 5.7 shows the results for the HBT measurements. The correlation peaks are separated by the $t_L = 13$ ns of the excitation laser's pulsed emission. The peaks are fitted using a multi-peak Gaussian where the width gives the combined IRF of the SPADs and TCSPC. Using Equation 5.1, the pulse width (τ_L) of 13 ps (red) gives a $g_{HBT}^{(2)}(0) = 0.134 \pm 0.003$. This gives a single-photon purity ($1 - g_{HBT}^{(2)}(0)$) of $86.6 \pm 0.3\%$.

The τ_L of 2.4 ps (blue) clearly shows the narrower peak width from the improved IRF. The $g_{HBT}^{(2)}(0)$ measured for $\tau_L = 2.4$ ps is 0.026 ± 0.007 which gives a single-photon purity of $97.4 \pm 0.7\%$. The inset to Figure 5.7 shows the two HBT correlation peaks at time-zero. This shows that there were very few correlation counts for the $\tau_L = 2.4$ ps. The pulse length of 13 ps is relatively long compared to the exciton T_1 of 22.7 ± 0.9 ps [106]. Figure 5.8 shows the Monte Carlo results (green) of master equation simulations performed by John O'Hara in Ref.[106]. They show that multiple photon emission events, caused by re-excitation of the QD within the same excitation pulse, reduce the single-photon purity observed. The coloured points on Figure 5.8 are the measured values for $g_{HBT}^{(2)}(0)$ at a τ_L of 13 ps (red) and 2.4 ps (blue). When an excitation pulse with $\tau_L < T_1$ is used, the single-photon purity is improved as the likelihood of re-exciting the QD within the time that the excitation pulse is present in the system is decreased.

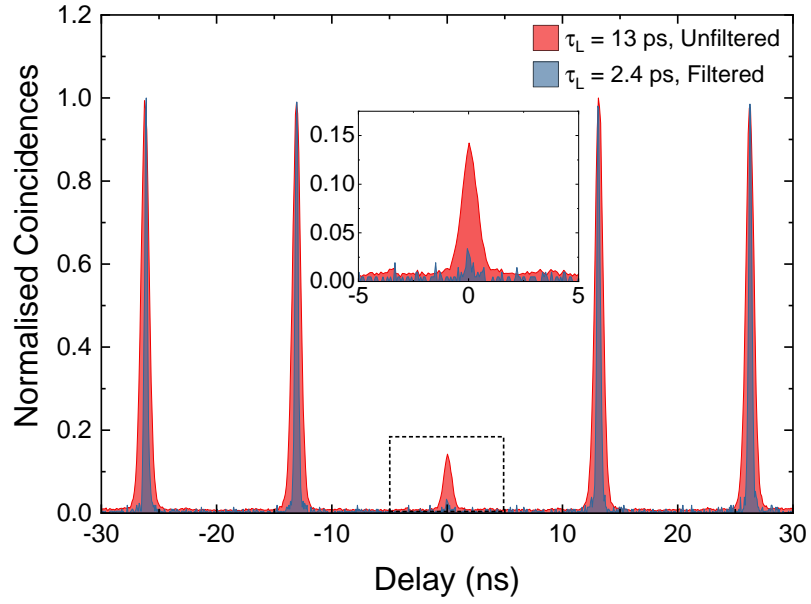


Figure 5.7: **HBT** measurements for the **QD** excited by a resonant π -pulse for laser pulse widths (τ_L) of 13 ps (red) and 2.4 ps (blue). The $\tau_L = 13$ ps emission is unfiltered, while the $\tau_L = 2.4$ ps is spectrally filtered using a $96 \mu\text{eV}$ grating filter to eliminate residual scatter from the sample surface from the spectrally broader laser excitation pulse. *Inset*: Increased scale for the time-zero peaks of the **HBT** measurements.

5.3.3 Method: Hong-Ou-Mandel

The sample is excited resonant to the neutral exciton emission with a π -pulse of length 13 ps (τ_L) and the emission is collected from an out-coupler. The laser background is suppressed using the cross-polarisation technique described in Section 3.4, the signal-to-background ratio is $\sim 20:1$. The entire emission collected from the out-coupler passes to the interferometer for the **HOM** ($g_{\text{HOM}}^{(2)}(t)$) measurements without any filtering. The first time delay (Δt) used was 2 ns. Before measuring a **HOM**, the Δt of the laser pulses is set to match that of the interferometer and the two arms of the interferometer are re-polarised, as described in Section 5.2.2.

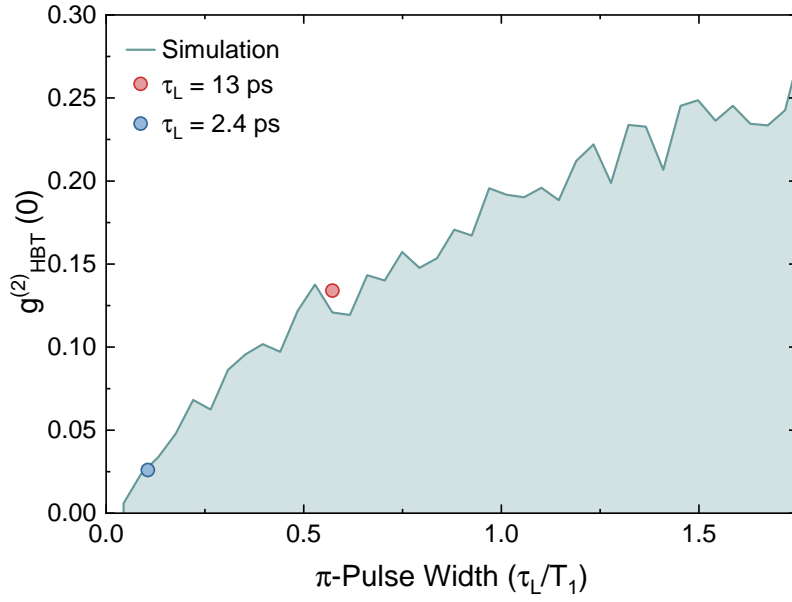


Figure 5.8: Monte Carlo simulations (green) of $g_{HBT}^{(2)}(0)$ as a function of the τ_L relative to the exciton T_1 of 22.7 ± 0.9 ps. The coloured points show the experimental results for the $g_{HBT}^{(2)}(0)$ with a π -pulse length (τ_L) of 13 ps (red) and 2.4 ps (blue). The Monte Carlo simulation was performed by John O’Hara.

The **TCSPC** is configured using the same parameters that were used for the **HBT** measurements. Again an extra electrical delay is added to one of the **SPAD** channels to centre the time-zero peak in the measurement window.

The **HOM** correlation measurement visibility is given by measuring with the interferometer in both co-polarised and cross-polarised configurations, where the photon indistinguishability is maximised and minimised respectively. The polarisation is rotated every 15 minutes during the measurement to minimise any time-dependent drifts. Due to a count-rate of 2-3 kHz on each channel at the **TCSPC**, the **HOM** measurements were run overnight with the signal to background monitored between each cycle.

5 Cavity-Coupled QD as a Single-Photon Source

After analysing the results for $\tau_L = 13$ ps and $\Delta t = 2$ ns, further measurements using a $\tau_L = 2.4$ ps and a Δt of 2 ns and 24 ns were performed to investigate the effect of the excitation pulse length and the time delay between the pulses. As for the HBT measurements, the $\tau_L = 2.4$ ps pulses required a 96 μeV grating filter to eliminate the reflected spectrally broad laser background to achieve a signal-to-background ratio of $\sim 50:1$.

5.3.4 Results: Hong-Ou-Mandel

Figure 5.9 shows the HOM two-photon interference visibility measurement for photons produced with a time separation of Δt of 2 ns and a $\tau_L = 13$ ps excitation pulse. Here, no filtering has been used between the sample and the interferometer. The expected five peak pattern centred around zero time delay is observed [149]. The five peaks arise from the different paths that consecutive photons can take through the interferometer. Like the HBT measurements, the HOM records coincidence events.

The peaks labelled 1 and 5 in Figure 5.9 are coincidence counts when the first photon in the pair takes the short path through the interferometer and the second photon takes the path delayed by Δt . There is a time difference of $2\Delta t = 4$ ns between the two detection events. This peak is repeated 4 ns away from time zero on both sides. This occurs as the time separated photons can exit from either port of the second beam splitter and so can be detected on either SPAD. If the first photon triggers the “CFD” SPAD to start the clock and the second photon triggers the “Sync” SPAD then the photon peak will be recorded at a time equal to the added electrical delay on the “Sync” channel plus the 4 ns delay that the second photon gained from the optical delay in the interferometer. However, if the photon that leaves the interferometer second triggers the clock on the “CFD” SPAD and the first photon exits through the “Sync” port of the second beam splitter then the “Sync” SPAD will detect the photon at a time of the electrical delay minus 4 ns. When both of the photons exit the same port of the second beam splitter then the event is not recorded as only one detector is triggered and thus no coincidence counts occur.

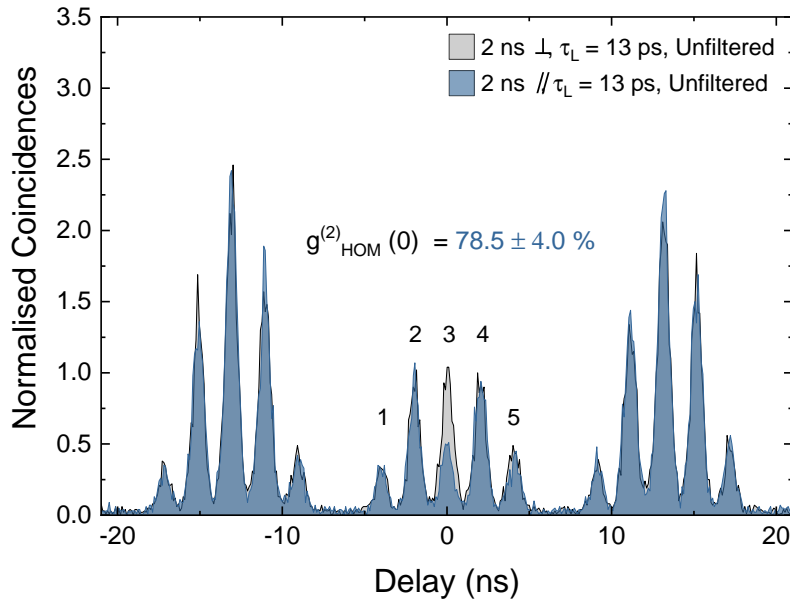


Figure 5.9: **HOM** measurements using Δt of 2 ns and π -pulse excitation with $\tau_L = 13$ ps. The coincidence count data for cross-polarised (\perp) arms of the interferometer is shown in grey and the coincidences for co-polarised (\parallel) interferometer arms are shown in blue. The $g_{HOM}^{(2)}(0)$ value shown is the corrected value taking into account multi-photon emission from the source and deviations of the interferometer beam splitter.

The peaks labelled 2 and 4 have twice the area of peaks 1 and 5 as they are populated by two different events. One is where both photons in the pair take the short path through the interferometer whilst the second event is where both photons take the delayed path. Both of these events have a time difference of $\Delta t = 2$ ns. Again, this peak is repeated either side of zero time delay.

The central peak (3) is where the first photon takes the delayed path and the second photon takes the short path through the interferometer. The difference in time between the first and second photon entering the interferometer is the same as the

5 Cavity-Coupled QD as a Single-Photon Source

time delay of the delayed path in the interferometer. Therefore, both photons reach the second beam splitter (Fig. 5.3) at the same time. If the two arms of the interferometer are co-polarised (\parallel), shown in blue on Figure 5.9, then the photons are maximally indistinguishable and indistinguishable photons take the same path out of the beam splitter. This means that no central peak would be seen for perfect indistinguishability as there would be no coincidence detection events. The grey data in Figure 5.9 shows where the two arms of the interferometer are set to be cross-polarised (\perp). This means that when the photons reach the second beam splitter, they are maximally distinguishable from each other due to their difference in polarisation. Therefore, they are not limited to taking the same path out of the interferometer and so a peak in coincidence counts is seen. By fitting the areas of Peak 3 under both conditions, Equation 5.3 can then be used to find the raw HOM visibility. In this case the raw visibility is $51.2 \pm 3.9 \%$.

Equation 5.3 gives the raw visibility of the two-photon interference. To calculate the true visibility, it is necessary to correct for deviations in the beam splitters used in the interferometer away from their ideal behaviour, as well as multi-photon emission from the sample. There are two different analysis methods for extracting the true HOM visibility.

The first method uses the following equation [149], where A_3 is the area of peak 3:

$$A_3 \propto (R^3T + RT^3)(1 + 2g_{HBT}^{(2)}(0)) - 2(1 - \epsilon)^2R^2T^2V. \quad (5.4)$$

Here the parameters are the $g_{HBT}^{(2)}(0)$ value, the fringe contrast of the interferometer ($1 - \epsilon$), and both the reflection (R) and transmission (T) coefficients of the beam splitters. Equation 5.4 assumes that both of the beam splitters used in the HOM interferometer have the same values of R and T . These values are shown in Table 5.2.

The left part of Equation 5.4 considers the probability that two photons entering the interferometer simultaneously, therefore when $g_{HBT}^{(2)}(0)$ is non-zero, take the same

Parameter	Value	Correction	Measurement Method
$(1 - \varepsilon)$	0.968 ± 0.004	6.38 %	Measurement of fringe contrast with a single mode laser
$g_{HBT}^{(2)}(0),$ $\tau_P = 13$ ps	0.134 ± 0.003	19.5 %	HBT
$g_{HBT}^{(2)}(0),$ $\tau_P = 2.4$ ps	0.026 ± 0.007	4.0 %	HBT
R	0.544 ± 0.002	1.53 %	Resonant transmission with a single mode laser
T	0.456 ± 0.002		
Polarisation	99.99 ± 0.01 %	<0.01 %	Resonant extinction with a single mode laser

Table 5.2: Parameters used to correct the raw HOM two-photon interference visibility. The correction column shows the estimated contribution of each component. However, these values are approximate due to the co-dependence of the parameters from equations 5.4 and 5.6

path at the first beam splitter (i.e. R^2 or T^2 for the first beam splitter) and then leave from opposite ports of the second beam splitter, therefore each of the terms for the first beam splitter are multiplied by RT for the second beam splitter. The right hand side of Equation 5.4 is the probability that two photons, which are separated by the interferometer path-length difference (Δt), take the correct paths through the interferometer to arrive simultaneously at the second beam splitter. This would give a factor of RT for the first beam splitter. If these photons then exit from opposite ports of the second beam splitter then a second factor of RT needs to be included for the second beam splitter. As this can only occur if the two photons do not interact at the second beam splitter this term is normalised by the $(1-\varepsilon)$ term and so would vanish for a “perfect” second beam splitter. The factor of $g_{HBT}^{(2)}(0)$ is included as the single-photon purity is an area that can be improved on (for example, through different excitation schemes, as shown in Section 5.3.2). The single-photon purity can therefore be seen

5 Cavity-Coupled QD as a Single-Photon Source

as a limiting factor for the **HOM** and so can be corrected for.

The values of $g_{HBT}^{(2)}(0)$ are the ones measured in Section 5.3.2. The fringe contrast of the interferometer was measured by adding a piezo-tunable free-space delay to one arm of the interferometer. Then, after equalising both the length and intensity through each of the interferometer arms, and setting the arms to be co-polarised, a single mode **CW** laser was used to measure transmission through the interferometer as a function of the delay. The **CW** laser has the same wavelength as the neutral exciton emission from the **QD** that was used in **RF** for the **HOM**. The fringe contrast data is shown in Figure 5.10. The total fringe contrast was obtained by finding the contrast for each fringe using Equation 5.5 and taking the mean over many fringes:

$$(1 - \varepsilon) = \frac{I_{max} - I_{min}}{I_{max} + I_{min}}. \quad (5.5)$$

By using equation 5.4 and taking $V = 1$ for $A_{3\parallel}$ and $V = 0$ for $A_{3\perp}$, the raw visibility that would be measured for perfectly indistinguishable photons can be extracted. Using this to normalise the raw visibility of $51.2 \pm 3.9\%$, it is possible to correct for just the interferometer properties by setting the $g_{HBT}^{(2)}(0)$ contribution to zero. This gives a corrected visibility of $59.0 \pm 4.0\%$. When including the $g_{HBT}^{(2)}(0)$ component, the corrected value becomes $V = 78.5 \pm 4.0\%$.

The second, equivalent, correction method uses a single equation that compares $A_{3\parallel}$ to $A_{2\parallel}$ and $A_{4\parallel}$ rather than also using the cross-polarised **HOM** measurement [155]:

$$V = \frac{1}{(1 - \varepsilon)^2} \left[2g^{(2)}(0) + \frac{R^2 + T^2}{2RT} - \frac{A_{3\parallel}}{A_{2\parallel} + A_{4\parallel}} \left(2 + g_{HBT}^{(2)}(0) \frac{(R^2 + T^2)}{RT} \right) \right]. \quad (5.6)$$

Applying this equation to the raw visibility gives a corrected visibility of $V = 74.0 \pm 3.1\%$.

As with the **HBT** measurements, the **HOM** measurement was repeated using the narrower pulse width (τ_L) of 2.4 ps. Again, filtering of 96 μeV is used to eliminate laser scatter from the spectrally broad pulse. For this measurement newer **SPADs** were

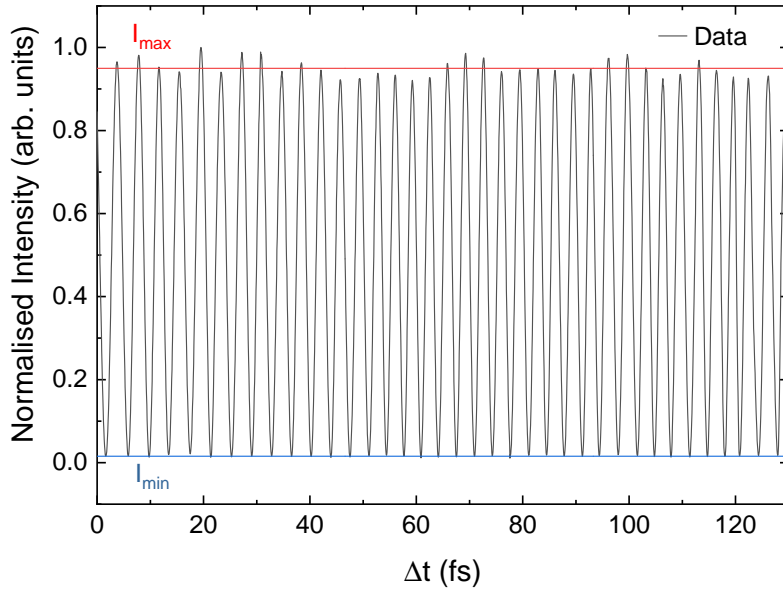


Figure 5.10: Interference fringes using single-mode CW laser through the Mach-Zehnder interferometer. Fringes are measured while varying the delay length in one arm of the interferometer.

used, this gives narrower coincidence peaks due to their improved IRF of ~ 340 ps as opposed to ~ 860 ps. Figure 5.11 shows the HOM measurement for $\tau_L = 2.4$ ps and $\Delta t = 2$ ns. The coincidence count data for when the two arms of the interferometer are cross-polarised (\perp) is shown in grey and the red data is where the arms of the interferometer had been set to be co-polarised (\parallel). The raw data gives a visibility of 81.0 ± 3.7 %. After correcting for the beam splitter, using Equation 5.4, without the multi-photon emission correction the visibility is 88.8 ± 3.8 %. The corrected visibility increases to 93.3 ± 3.6 % when the effects of multi-photon emission are included. In carrying out this correction, the $g_{HBT}^{(2)}(0)$ value for the $\tau_L = 2.4$ ps pulses is used.

The raw visibility is higher than for the longer τ_L partially due to the reduction in multi-photon emission. As can be seen from Table 5.2, the $\tau_L = 2.4$ ps HBT contribution to the HOM correction is much smaller than that of the $\tau_L = 13$ ps HBT contri-

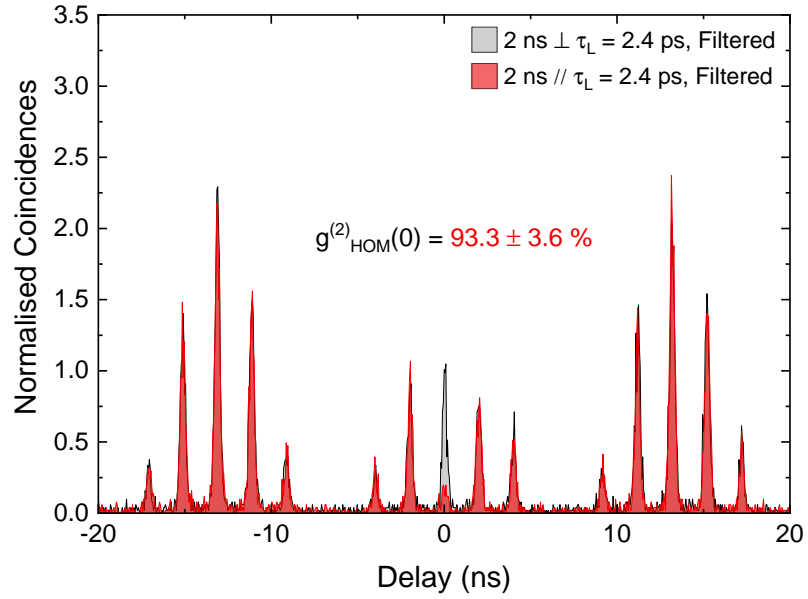


Figure 5.11: **HOM** measurements using Δt of 2 ns and resonant π -pulse of $\tau_L = 2.4$ ps. The coincidence count data for cross-polarised (\perp) arms of the interferometer is shown in grey and the coincidences for co-polarised (\parallel) interferometer arms are shown in red. The $g_{HOM}^{(2)}(0)$ value is the corrected value taking into account multi-photon emission from the source and deviations of the interferometer beam splitter from an ideal beam splitter.

bution. The visibility is also improved due to the spectral filter, used to remove the spectrally broad laser background, as this filter also removes a significant amount of the phonon sideband. Theoretical studies have suggested that for unfiltered emission from InGaAs QDs at 4.2 K that are not Purcell-enhanced, the single-photon visibility is limited to around 80 % due to incoherent phonon sideband emission, comprising around 10 % of the total spectrum [95, 100]. As visibility compares two photons, both of the compared photons should be emitted from the ZPL to have the highest probability of indistinguishability. However, emission is a probabilistic event, with each photon having a ~ 90 % chance of being emitted from the ZPL and ~ 10 % from the PSB. This leads to an indistinguishability limit of $0.9 \times 0.9 \approx 80$ %. The visibility can

be improved, without the losses from filtering, by using a QD in a resonant high- Q cavity. However, for the QD used here the Q -factor is relatively low. Therefore, the cavity filtering effect is weaker, introducing a theoretical upperbound to the unfiltered visibility of $\sim 90\%$ [95].

A value of Δt of 2 ns is the equivalent of comparing the indistinguishability of photons produced over 20 emission cycles of the QD if it were driven with a 10 GHz pulsed laser. This would produce a pulse separation of 100 ps which at $4.4T_1$ is sufficient to allow for essentially complete radiative recombination between pulses [106]. To look at how the indistinguishability decays over longer repetition times, a Δt of 24 ns was used. This is the equivalent of comparing the indistinguishability of photons produced over 240 emission cycles if 10 GHz excitation is used.

Figure 5.12 shows the HOM for resonant π -pulse excitation using $\tau_L = 2.4$ ps and $\Delta t = 24$ ns. As can be seen, the peaks $A_{2\parallel}$ and $A_{4\parallel}$ are not easily identifiable due to the many overlapping peaks. The change in the $g_{HOM}^{(2)}(t)$ histograms occurs as Δt is longer than the pulse separation generated by the laser, $t_L = 13$ ns, under these conditions. Care has to be taken when choosing the Δt that none of the sidepeaks overlap with the time-zero correlation peak. Equation 5.4 is used to correct for the interferometer and multi-photon component as it only compares the $A_{3\perp}$ and $A_{3\parallel}$ peaks. The raw visibility for this measurement is $69.0 \pm 3.4\%$ which gives a corrected visibility of $76.7 \pm 3.4\%$ when only considering the interferometer deviations and a corrected visibility of $81.3 \pm 3.6\%$ when including the multi-photon components of the QD emission. This shows a 12% difference between the single-photon indistinguishability at $\Delta t = 2$ ns and $\Delta t = 24$ ns.

The reduction in photon indistinguishability at 24 ns compared to 2 ns is attributed to spectral wandering caused by fluctuations in the charge environment on the scale of tens of nanoseconds, as the Δt of 24 ns is much greater than the QDs T_1 of 22.7 ± 0.9 ps.

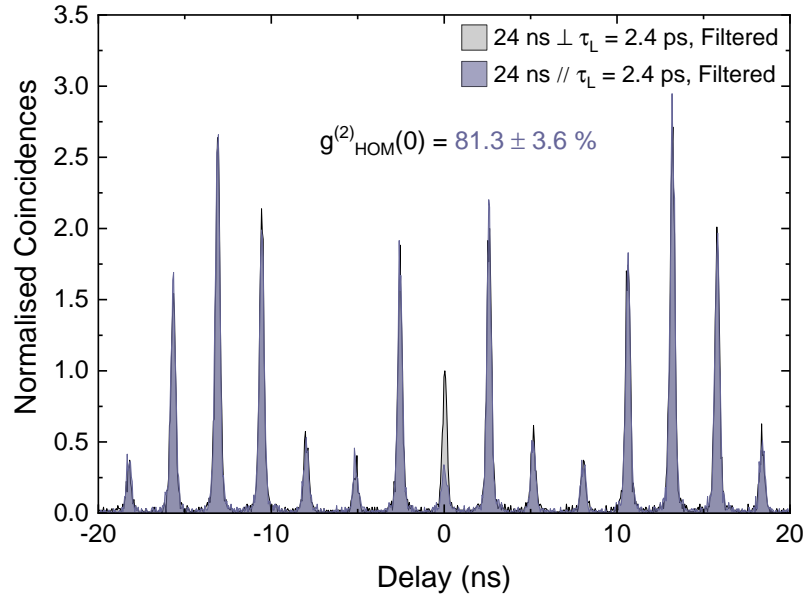


Figure 5.12: **HOM** measurements using Δt of 24 ns and resonant π -pulse excitation with $\tau_L = 2.4$ ps. The coincidence count data for cross-polarised (\perp) arms of the interferometer is shown in grey and the coincidences for co-polarised (\parallel) interferometer arms are shown in purple. The $g_{HOM}^{(2)}(0)$ value is the corrected value taking into account multi-photon emission from the source and imperfections of the interferometer beam splitter.

The fluctuations in the charge environment could be a result of etched surfaces close to the QD [156, 157]. A previous study using QD microlens structures, which also include etched surfaces close to the QD, showed a visibility decrease of $\sim 40\%$ caused by spectral wandering on a time scale of 12.5 ns, which is comparable to the 24 ns time scale used here [158]. The advantage of the QD device studied here is its very short T_1 enhanced by the Purcell factor (F_p), meaning that a given amount of spectral wandering degrades the visibility far less than the non-Purcell enhanced case. Furthermore, photons can be extracted much faster than the spectral wandering timescale and thus longer strings of indistinguishable photons may be generated before their indistinguishability begins to degrade.

5.4 Conclusion

The results presented in this chapter show that a QD in a H1 PhCC can act as an excellent single photon source, enabled particularly by the Purcell factor of 43, giving a shortened T_1 of 22.7 ± 0.9 ps for the neutral exciton. The first important property shown in Section 5.3.2 is a high single-photon purity. Exciting above the cavity, resonant to the neutral exciton with a π -pulse of 13 ps in length and collecting from the end of a waveguide, a single-photon purity of $86.6 \pm 0.3\%$ is observed. This value is measured without the use of spectral filtering. The lack of a need for spectral filtering shows promise for on-chip experiments [34] where the produced photons are manipulated and detected without leaving the chip to be filtered.

The effect of the excitation pulse length on the single-photon purity has also been investigated with a shorter pulse length (τ_L) of 2.4 ps, giving an improved single-photon purity of $97.4 \pm 0.7\%$. The shorter pulse length is much smaller than T_1 of the QD and therefore reduces the probability that the neutral exciton will be re-excited during the excitation pulse. The $\tau_L = 2.4$ ps pulse requires the collected emission to be spectrally filtered to remove the residual laser scatter from the spectrally broad pulse, however on-chip experiments would not require this filtering.

As well as investigating the single-photon purity, the indistinguishability of the photons produced has also been measured. Using a 13 ps excitation pulse, the single-photon corrected indistinguishability for this device is shown to be $78.5 \pm 4.0\%$ without spectral filtering. The largest contribution to the visibility correction has been shown to be the single-photon purity ($g_{HBT}^{(2)}(0)$). Therefore, using the shorter τ_L of 2.4 ps, which increases the single-photon purity, gives a visibility, after correction, of $93.3 \pm 3.6\%$. The shorter τ_L also shows a higher visibility due to the spectral filtering used, due to the removal of the majority of the phonon sideband. The incoherent emission from the phonon sideband would introduce a theoretical upper bound of $\sim 90\%$ without the use of spectral filtering [95]. Both of these measurements were

5 Cavity-Coupled QD as a Single-Photon Source

carried out with a HOM delay line (Δt) of 2 ns, the equivalent of comparing the indistinguishability over 20 photons if a 10 GHz excitation laser had been used.

The τ_L of 2.4 ps excitation was also used with a Δt of 24 ns to compare photons over a longer timescale, the equivalent of 240 photons if a 10 GHz excitation laser had been used. This gave a visibility of $79.9 \pm 3.4\%$ after correction. This decrease in the visibility is attributed to spectral wandering caused by charge fluctuations within the QD, possibly due to the close proximity between the QD and etched surfaces [156–158].

The single-purity and indistinguishability measured using this sample shows promise for the development of on-chip optical circuits. For example, off-chip experiments using QDs as single-photon sources have demonstrated boson-sampling while using indistinguishabilities of $\sim 65\%$ [28, 159] and the current state-of-the-art for boson sampling off-chip uses an indistinguishability of 94% [27]. The results presented in this Chapter show greater or comparable visibilities using an on-chip design of QD embedded in a H1 PhCC with coupled waveguides, suggesting that this design could be used as a foundation for building fully integrated on-chip boson sampling experiments or other optical quantum technologies requiring high quality single photons.

6 Phonon Effects on QD Emission

The work presented in this chapter has been published in:

Alistair J. Brash, Jake Iles-Smith, **Catherine L. Phillips**, Dara P. S. McCutcheon, John O'Hara, Edmund Clarke, Benjamin Royall, Luke R. Wilson, Jesper Mørk, Maurice S. Skolnick, A. Mark Fox, and Ahsan Nazir.

“Light Scattering from Solid-State Quantum Emitters: Beyond the Atomic Picture.”
Physical Review Letters **123**, 167403 (2019).

First-order correlation measurements were set up and carried out by Catherine Phillips and Alistair Brash. High resolution spectroscopy of the coherent scatter using a Fabry-Pérot interferometer was measured by John O'Hara and Alistair Brash. The lower resolution spectroscopy of the phonon sideband was set up and measured by Catherine Phillips and Alistair Brash.

All of the Polaron theory modelling and fitting in this chapter was performed by our collaborators: Jake Iles-Smith, Dara McCutcheon and Ahsan Nazir.

6.1 Introduction

The coherent scattering of light from quantum emitters is a fundamental process that is used as a foundation for many quantum-optics applications. These applications typically exploit two important properties of coherent scattering: it retains the coherence of the excitation laser and shows antibunching on the timescale of the emitter lifetime. (Whether these properties can be measured simultaneously will be dis-

cussed in Chapter 7.) Solid-state emitters are promising candidates for many proposed quantum technologies owing to their strong light-matter interactions and ease of integration with photonic structures. However, solid-state emitters demonstrate strong environmental couplings through phonon interactions leading to phenomena such as the appearance of a phonon sideband (PSB). Phonon effects were introduced in Section 2.4.2.

This chapter presents an experimental investigation into the influence of phonon coupling in different RF regimes, accompanied by the theoretical modelling performed by our collaborators. First-order correlation ($g^{(1)}(t)$) measurements are used in conjunction with spectroscopy measurements to resolve the phonon and emission properties of the QD in both the time and frequency domain, showing deviation from the two-level “atomic picture”. High and low resolution spectroscopy measurements are used to show that the proportion of RF emission into the PSB is insensitive to the excitation power. Furthermore, $g^{(1)}(t)$ measurements are used to show a non-monotonic relationship between the detuning of the excitation laser and the coherent fraction that originates from phonon-mediated relaxation. All of these results show deviations from the idealised “atomic picture” of scattering from a two-level emitter. They do however show excellent agreement with theory modelling produced using polaron master equations.

6.2 Coherent Scattering

Continuous wave (CW) driving of a two-level emitter (TLE) comprises two fundamental interactions. The first is coherent scattering which is also known as elastic scattering or resonant Rayleigh scattering. This is where the excitation photon from the CW laser scatters elastically from the TLE transition, meaning that absorption and emission from the system become a single coherent event. There is no change in the population of the levels for coherent scattering. This is shown in Figure 6.1(a).

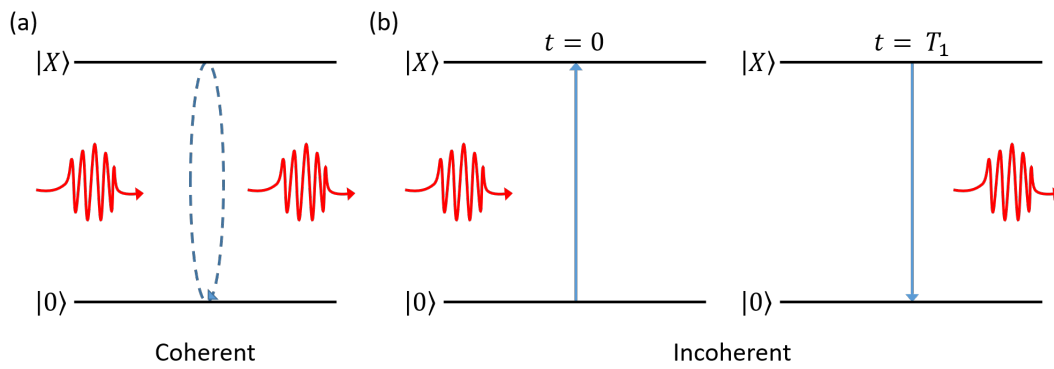


Figure 6.1: (a) Coherent scattering from a two-level emitter. (b) Incoherent emission from a two-level emitter where the laser photon is absorbed, exciting the system. Relaxation due to spontaneous or stimulated emission then occurs, with a coherence time of T_1 , emitting a photon with the energy of the transition.

These elastically scattered photons retain the coherence of the excitation laser. This long coherence time leads to the observation of a “sub-natural linewidth”, whereby the width of the scattered spectrum implies a coherence time longer than the conventional radiative limit $T_2 = 2T_1$. Coherent scattering from a quantum emitter was first observed for atomic systems [160–162]. More recently, coherent scattering from QD systems has also been investigated [49, 106, 163–166]. The second fundamental interaction is incoherent scattering, also known as inelastic scattering. This process is shown in Figure 6.1(b). Here, the excitation laser photon is absorbed, exciting the system and populating the excited state. The TLE later relaxes due to spontaneous or stimulated emission, releasing a photon with the same energy as the optical transition. In the absence of any dephasing, the coherence of this process is governed by the transition lifetime (T_1).

The presence of the two components discussed above in the scattered light from a TLE was first demonstrated in a seminal paper by Mollow [81]. He showed that

6 Phonon Effects on QD Emission

when a TLE with the natural resonance frequency ω_0 is exposed to a monochromatic field of frequency ω (e.g. a CW excitation laser) the power spectrum of the scattered light has the form [81, 164]¹:

$$\tilde{g}(\nu, \omega, \omega_0) = 2\pi|\alpha_\infty|^2\delta(\nu - \omega) + \bar{n}_\infty\kappa\Omega^2 \frac{(\nu - \omega)^2 + \Omega^2/2 + \kappa^2}{|f(i(\nu - \omega))|^2}, \quad (6.1)$$

The first term in Equation 6.1 describes coherent scattering, the delta function indicating this component is monochromatic with the frequency of the excitation laser (ω). The second term in the equation describes incoherent emission with a Lorentzian lineshape. (Another form of the expressions for the respective contributions of the coherent scattering and incoherent emission can be found in [167] p.p. 382-386, where the scattering is modelled in terms of photodetection signals.)

Using a two-level “atomic picture”, there is no coupling of the TLE to its environment. Therefore, the main dephasing mechanisms are radiative decay and pure dephasing, which are related to the coherence time of the emitter through Equation 2.7. In the “atomic picture” the coherent fraction of the total emission (\mathcal{F}_{CS}) is given by:

$$\mathcal{F}_{CS} = \frac{T_2}{2T_1} \frac{1}{1 + \mathcal{S}}. \quad (6.2)$$

Here, \mathcal{S} is the generalised saturation parameter defined as:

$$\mathcal{S} = \frac{(\Omega^2 T_1 T_2)}{(1 + \Delta_{LX}^2 T_2^2)}, \quad (6.3)$$

where Ω is the Rabi frequency, T_1 and T_2 are the emitter lifetime and coherence time respectively and $\Delta_{LX} = \omega_L - \omega_X$ is the laser (ω_L) and emitter (ω_X) detuning. Equation 6.2 generalises expressions from [167] pp. 369, 383 to include pure dephasing.

¹Here, ν is the emission frequency, $\kappa = 1/T_1$ is the spontaneous emission rate of the excited state decaying to the ground state and Ω is the Rabi frequency. The function f is a third-degree polynomial, defined in [81, 164], along with α_∞ , the steady-state quantum mechanical expectation value of the two-level coherence, and \bar{n}_∞ , the steady-state population inversion which is also known as the equilibrium probability of finding the TLE in the excited state. In Equation 6.1, f , α_∞ and \bar{n}_∞ are defined in terms of κ , Ω , the laser detuning ($\Delta\omega = \omega - \omega_0$), the pure dephasing rate ($\frac{1}{T_2^*} = \frac{1}{2T_1} - \frac{1}{T_2}$) and s , the complex frequency parameter from performing a Laplace transformation to convert the time dependency to a frequency dependent power spectrum.

Equation 6.2 shows that the coherent fraction approaches unity when the system is driven well below saturation ($S \ll 1$) and the emitter coherence is radiatively limited ($T_2 = 2T_1$). The coherent fraction also approaches unity for large detunings between the transition and the excitation laser ($\Delta_{LX} > T_2$).

As well as having a sub-natural linewidth due to inheriting the laser coherence time, the emission in the limit $S < 1$ has also been shown to exhibit antibunching on the timescale of the emitter lifetime [49, 163, 165, 166]. This combination of properties makes coherent scattering from TLEs well suited to many quantum-optics applications including: creating tuneable single photons [168–170], generating entangled photon states [171, 172], single photon non-linearities [173–175], and for entangling remote spins [176, 177]. Solid-state emitters, such as QDs, are useful for these applications as they are stationary and can be incorporated into photonic structures. These integrated photonic structures can route photons and create cavities around the emitter, potentially enhancing both the collection efficiency and emission rate.

However, solid state emitters are coupled to their environments. This can lead to dephasing effects caused by fluctuating charge environments [178, 179] and phonon broadening at elevated temperatures through strong coupling with the vibrational modes of the bulk material [180, 181]. Both of these are pure dephasing effects that broaden the ZPL and can thus be captured by the pure dephasing time T_2^* . The phonon broadening of the ZPL in InGaAs QDs can be suppressed through the use of photonic structures, resonant π -pulse excitation and cryogenic temperatures [106, 155, 182], leading to the emission transform-limited photons from the ZPL. Working with resonant π -pulse excitation produces the maximum signal intensity for the lowest excitation power [96, 98, 183], meaning that phonon-mediated excitation induced dephasing (EID) is minimised compared to driving with larger pulse areas. However, the coupling to the vibrational modes of the bulk material also leads to a broad PSB in the QD emission spectrum [95, 99, 181, 184–187]. Similar PSBs have also been seen in

6 Phonon Effects on QD Emission

many other solid-state systems including defects in Hexagonal Boron Nitrate (HBN) [188], colour centres in diamond [189], carbon nanotubes [190], monolayer transition metal dichalcogenides (TMDCs) [191] and single organic molecules [192].

The phonon sideband is attributed to a rapid change in the configuration of the bulk material's lattice during transitions between states of the emitter. This configuration change originates from the difference in Coulomb interaction between the lattice and the charge configurations associated with the ground and excited states. This leads to simultaneous emission or absorption of longitudinal acoustic (LA) phonons alongside the emission of a detuned "sideband" photon. Consequently, to measure perfectly indistinguishable photons, the PSB needs to be removed from the emission signal. This can be achieved through the use of spectral filters. However, this does reduce the efficiency of the single-photon source. If the emitter is embedded in a cavity with a moderate-to-high Q factor then the cavity acts as a spectral filter. Although increasing Purcell enhancement increases the emission into the ZPL in this regime the efficiency of the indistinguishable single-photon source is still reduced, mediated by the fraction emitted into the PSB [95, 100, 193].

The QD studies of the PSB previously referenced were performed with strong resonant π -pulse excitation where incoherent scattering dominates. In this regime, there is a large excited state population and thus a definite change in the charge configuration of the QD. By contrast, in the coherent scattering regime there is a vanishingly small exciton population. Therefore, it could be assumed that there would be no PSB effects, as there is no change in the charge configuration. However, recent theory predictions show phonon effects even at vanishingly weak resonant excitation [99]. The following measurements explore these effects and their deviations from the "atomic picture" described by Equation 6.2.

6.3 First-Order Correlation Measurements

As well as the second-order correlation function, as described in Section 5.2, the first-order correlation function can also be measured. The first-order correlation function ($g^{(1)}(t)$) quantifies the properties of the first power of the electric field through field-field correlations [47] and is used here to study the coherence of light scattered by the QD in the time domain.

6.3.1 Experimental Method

The first-order correlation function is measured through use of a Mach-Zehnder interferometer. The set-up for the fibre-based interferometer used in these experiments is shown in Figure 6.2. The collected emission from the sample passes through a 50:50 fibre beam splitter and down the two arms of the interferometer. One arm of the interferometer contains a free-space time delay comprising a retroreflector mounted on a 225 mm motorised linear delay stage. The second arm comprises a Phoenix Photonics “Electronic all-fibre variable phase shifter”. The phase shifter is controlled through use of a voltage source and the phase shift is induced by heating the fibre, without affecting the fibre polarisation. The second arm also has a Thorlabs “Electronic variable optical attenuator” (VOA) which is controlled by a second voltage supply and is used to balance the power through the two arms of the interferometer. It is installed in this arm of the interferometer as the delay stage arm has greater emission losses. The main source of loss is due to the recoupling of the emission back into the single-mode fibre after the free-space delay stage. However, there are also additional losses due to the reflections on the two mirrors and the retroreflector.

Both arms of the interferometer use fibre paddles so that the emission can be set to be co-polarised as it recombines at the second beam splitter, using the method previously described in Section 5.2.2. Having balanced power and co-polarised interferometer arms is important to maximise the fringe contrast in the measurement

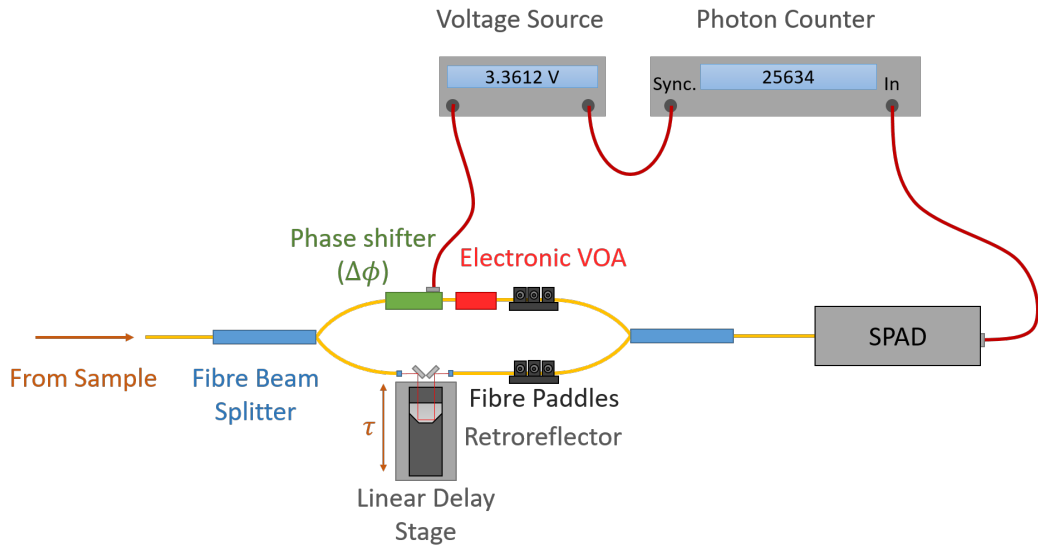


Figure 6.2: Schematic for the fibre-based Mach-Zehnder interferometer used for first-order correlation measurements ($g^{(1)}(t)$). A 50:50 fibre beam splitter is used to split the QD emission between the two paths of the interferometer. One path contains a fibre phase shifter that provides a phase shift ($\Delta\phi$) when voltage is applied. The other arm contains a free-space time delay through use of a retroreflector mounted on a motorised linear stage, controlling the path difference (τ) between the two arms. An electronic variable optical attenuator (VOA) is used to balance the power through both arms of the interferometer. A 50:50 fibre beam splitter then recombines the emission on to a SPAD which is connected to a photon counter.

of $g^{(1)}(t)$. After the emission is recombined at the second 50:50 fibre beam splitter, it travels to a single-photon avalanche diode (SPAD). The SPAD is connected via coaxial cables to an Stanford Research Systems SR400 photon counter.

During the set-up of the Mach-Zehnder interferometer, the time-zero position of the delay stage needs to be found, to calibrate the time delay between the two interferometer arms. This is achieved through interferometric measurements, as shown in

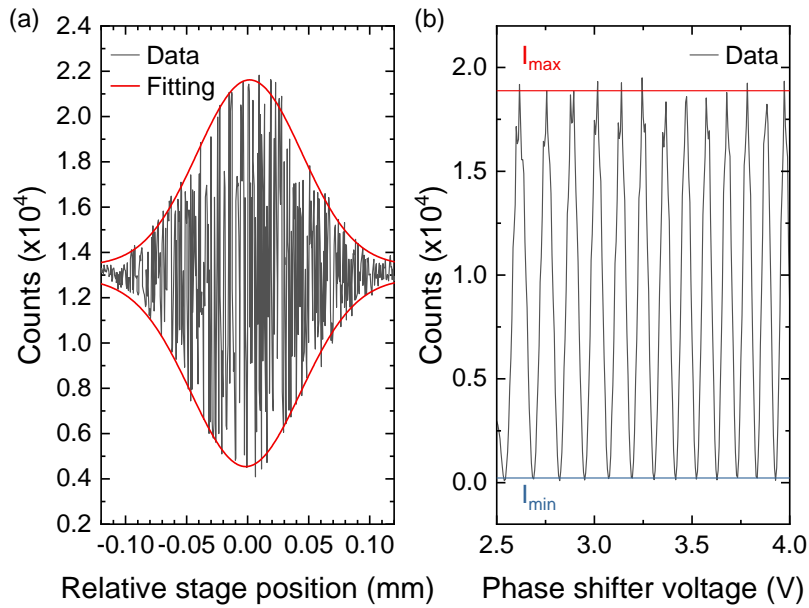


Figure 6.3: (a) Interferometric measurements are used to find the time-zero position of the motorised linear stage in the Mach-Zehnder interferometer. The Mira pulsed **Ti:S** laser is sent through the interferometer while the delay stage is stepped. Time-zero occurs when both pulses meet at the second beam splitter at the same time. This is seen as a maximum in the interference fringes. (b) Interference fringes recorded as a function of $\Delta\phi$ by the photon counter for a fringe contrast measurement, using emission from the **QD** under **CW** excitation. $\Delta\phi$ is swept by changing the voltage applied to the fibre phase shifter.

Figure 6.3(a). The Mira **Ti:S** pulsed laser, tuned to the resonant wavelength of the **QD** neutral exciton, is attenuated and sent through the interferometer. The delay stage is stepped and at each step the signal at the **SPAD** is recorded by the SR400 photon counter. Maximum fringe intensity occurs when the laser pulses that have been split between the two arms of the interferometer arrive simultaneously at the second beam splitter. This occurs when both arms of the interferometer have the same length in time or when the τ between the arms differs by the pulse separation of the laser.

6 Phonon Effects on QD Emission

However, as the difference between laser pulses corresponds to 3.9 m in free-space or ~ 2.69 m in fibre, a comparison of the interferometer arms can be made before measuring time-zero, allowing extra fibre delay to be added if required. It is also useful to adjust the relative length of fibre in both arms to ensure that time-zero is close to the near end of the delay stage, as this allows for a larger range of τ delay values to be reached.

During a $g^{(1)}(t)$ measurement, the time delay (τ) between the two arms of the interferometer is stepped. At each step, a set of interference fringes like those shown in Figure 6.3(b) are measured. To measure this, the voltage supply steps the voltage to the electronic phase shifter to change $\Delta\phi$. Each time the voltage is stepped, the voltage supply also sends a trigger to the ‘‘Sync’’ channel on the SR400 photon counter. The SR400 is gated to count photons for $\sim 95\%$ of the time that the voltage supply is set to wait at each voltage. This is done to allow the phase to stabilise after each voltage step. After a set of interference fringes has been measured their fringe contrast is calculated using:

$$v = \frac{I_{max} - I_{min}}{I_{max} + I_{min}}. \quad (6.4)$$

The fringe contrast is calculated for each fringe individually and then averaged to give the total fringe contrast. The fringe contrast v is related to $g^{(1)}(t)$ through:

$$v(\tau) = (1 - \varepsilon) \frac{|g^{(1)}(\tau)|}{g^{(1)}(0)}, \quad (6.5)$$

where $(1 - \varepsilon)$ is the maximum resolvable fringe contrast of the interferometer measured using a CW laser and is used to account for imperfections in the fibre beam splitters that would prevent perfect mode overlap. Measuring $|g^{(1)}(\tau)|$ gives the time-averaged coarse-grained value of $g^{(1)}(t)$ as the first-order correlation function also oscillates at the transition frequency, resulting in fringes within the $g^{(1)}(t)$. Measuring $|g^{(1)}(\tau)|$ fringes measures the envelope of the first-order-correlation fringes. The magnitude ($|\dots|$) is used in Equation 6.5 as the theoretical expression for $g^{(1)}(\tau)$ is complex and only the real components are measured. Fringe contrast v has a magnitude be-

tween 0 and 1. Therefore, the first-order correlation function has to be normalised to this range, this is achieved by the factor of $1/g^{(1)}(0)$. This total fringe contrast can then be plotted against the time delay (τ) to visualise the temporal coherence of the QD.

6.3.2 Results and Theory

Figure 6.4(a) shows the results of the $g^{(1)}(t)$ measurement made when the QD is excited resonant to the neutral exciton, with CW excitation and an excitation power corresponding to $S = 0.25$. The CW laser used for this work is the M-Squared Ti:S and the excitation power was calibrated using the Mollow triplet method described in Section 3.7.2. This method gives Ω that can then be converted to S using Equation 6.3, here $\Delta_{LX} = 0$. Both excitation and collection occurred directly above the H1 cavity of the PhC. The emission was collected using the cross-polarisation RF technique described in Section 3.4.

By using an S of 0.25, the QD is excited well below saturation and coherent scattering is expected to dominate the emission, whilst still ensuring sufficient emission intensity to perform accurate measurements. The dashed line in Figure 6.4(a) shows the mono-exponential result expected in this regime using the pure dephasing model predicted by atomic theory. Instead, the experimental data (triangles) shows a rapid decay of the coherence in the first few picoseconds. This timescale is comparable to that seen for phonon interactions in four-wave mixing measurements of InGaAs QDs [84, 194, 195], suggesting that the rapid loss of coherence is due to the same mechanism, electron-phonon interactions.

Hence, to describe the behaviour seen in Figure 6.4(a) a description of the microscopic nature of the electron-phonon interaction in the QD is needed [196]. Here this is achieved by applying the polaron transformation to the Hamiltonian of the full open quantum system. A polaron is a quasi-particle which describes the interaction

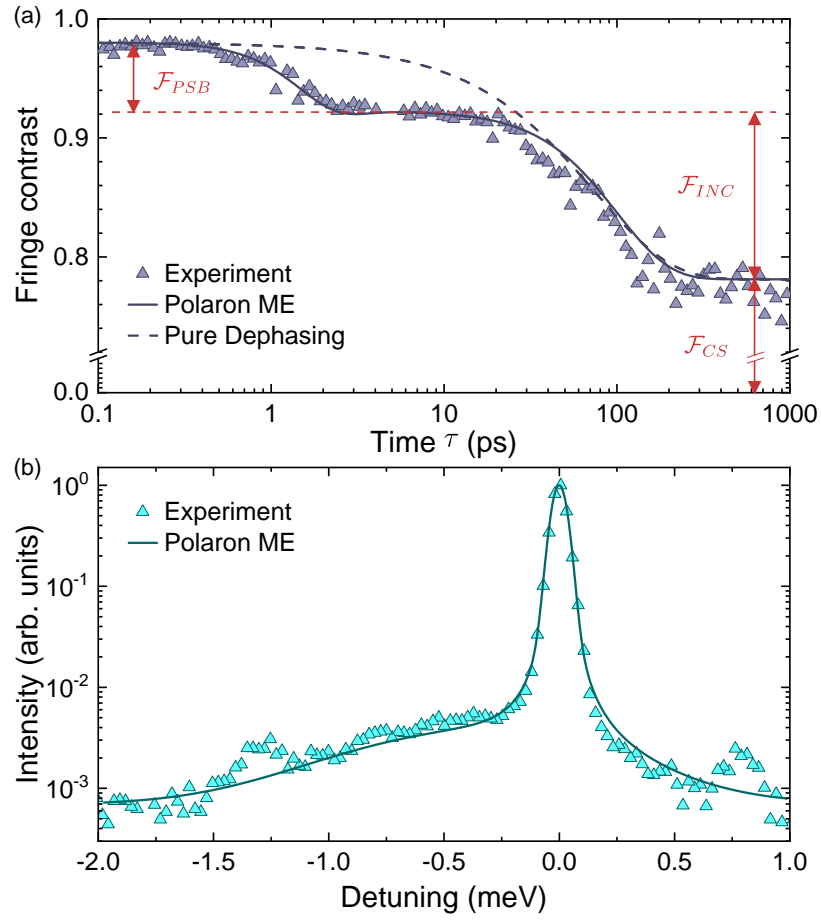


Figure 6.4: (a) First-order correlation measurement at $S = 0.25$ when $\Delta_{LX} = 0$. The experimental fringe contrast data (purple triangles) shows good agreement with a calculation made using the polaron master equation (solid purple line) where the only free parameters are the phonon coupling strength (α) and the cutoff frequency (ν_c) used in the phonon propagator (Equation 6.8). The dashed purple line shows the monoexponential predicted by a pure dephasing model, which does not capture the phonon dynamics present. (b) An experimental spectrum (blue triangles), taken at the same time as the $g^{(1)}(t)$ in (a), is also well produced using the polaron master equation with the same parameters. The spectrum calculated from the polaron master equation is convolved with the spectrometer IRF to reproduced the observed width of the ZPL.

between a charge and the surrounding lattice. Here, the charged particle is the exciton confined to the QD. When the exciton forms it displaces the surrounding semiconductor lattice, which returns to its original state when the exciton recombines. The QD can be modelled as a two-level system with a ground $|0\rangle$ and single-exciton state $|X\rangle$. The two level system is coupled to a phonon bath which can be represented by a infinite collection of harmonic oscillators. The polaron transformation displaces the bath of oscillators when the QD is in its excited state [197]. In other words, the polaron transformation dresses the excitonic states of the system with vibrational states, originating from the phonon environment. Dressing the states using the polaron transformation allows the derivation of a QD master equation (ME) that is nonperturbative in the electron-phonon coupling strength [99, 197–200]. For the following theory a more detailed explanation can be found in Brash et al. [200] and its associated supplement.

In the polaron frame, the first-order correlation function is given by [99]:

$$g_{pol}^{(1)}(\tau) = \mathcal{G}(\tau)g_{opt}^{(1)}(\tau). \quad (6.6)$$

Here $g_{opt}^{(1)}(\tau)$ is the purely optical contribution (equivalent to an ideal TLE) which is found using the polaron frame ME. $\mathcal{G}(\tau)$ is the polaron correction function for the phonon environment, accounting for the non-Markovian phonon relaxation, given by:

$$\mathcal{G}(\tau) = B^2 e^{\varphi(\tau)}, \quad (6.7)$$

where B is the Franck-Condon factor, defined as $B = e^{-\varphi(0)/2}$, and $\varphi(\tau)$ is the phonon propagator defined as:

$$\varphi(\tau) = \alpha \int_0^\infty v e^{-v^2/v_c^2} (\cos(v\tau) \coth(v/2k_B T) - i \sin(v\tau)) dv. \quad (6.8)$$

This means that the coupling of the QD to the phonon environment can be described by the thermal energy of the phonon environment ($k_B T$) and the coupling strength (α) and cut-off frequency (v_c) for the deformation potential coupling [184, 196, 201].

6 Phonon Effects on QD Emission

The coupling strength (α) gives the strength of the exciton-phonon interaction and is dependent on the bulk properties of the QD [96, 197]. The exponential cut-off with frequency defines the highest possible energy of the LA phonons associated with a transition. For excitons in SAQDs the cut-off frequency is proportional to the inverse of the carrier localisation length, in other words it is inversely proportional to the size of the QD [184, 197, 202].

The polaron ME is further modified to include the effects of the cavity on the emission. The Purcell enhancement of the exciton transition is already included within the ME, but the cavity also leads to spectral filtering of the emission [95]. To include this effect, the polaron ME is modified to add a cavity filter function, giving the $g^{(1)}(t)$ correlation function for what is detected in a cavity-based system [200].

Both the cut-off frequency (ν_c) and the deformation-potential coupling strength (α) can be extracted by fitting the first 15 ps of the $g^{(1)}(t)$ measurement shown in Figure 6.4(a). The resulting values of $\nu_c = 1.3 \text{ ps}^{-1}$ and $\alpha = 0.045 \text{ ps}^2$ are comparable to values previously found for InGaAs QDs [96]. The other parameters in the polaron ME are set to directly measured values. The solid line in Figure 6.4(a) shows that the result of the polaron ME accurately reproduces the experimental $g^{(1)}(t)$. After the first rapid decay in coherence, attributed to phonon relaxation, a second decay in coherence occurs between $\tau = 20 - 200 \text{ ps}$. This decay is associated with incoherent resonance fluorescence and is consistent with the radiative lifetime of the QD. After $\tau = 200 \text{ ps}$, the $g^{(1)}(t)$ plateaus again. This plateau is caused by the coherent fraction of the emission where the long coherence time is inherited from the excitation laser. From the amplitude of the fringe contrast in each region of the $g^{(1)}(t)$ function, the fraction that each component contributes to the total emission (\mathcal{F}) can be determined (see arrows in Fig. 6.4(a)). This gives a phonon sideband fraction (\mathcal{F}_{PSB}) of 0.06, an incoherent fraction (\mathcal{F}_{INC}) of 0.14, and a coherently scattered fraction (\mathcal{F}_{CS}) of 0.80.

6.3 First-Order Correlation Measurements

To check the accuracy of the components extracted from the polaron ME, the emission was investigated in the frequency domain as well as the time domain. To measure this under the same conditions as the $g^{(1)}(t)$ function, part of the emission is sent to the spectrometer through use of a fibre beam splitter, before the emission reaches the Mach-Zehnder interferometer. The spectrum measured is shown in Figure 6.4(b) (triangles).

The emission spectrum is calculated theoretically by taking the Fourier transform of the first-order correlation function derived from the polaron ME. This can be written in the form:

$$S(\omega) = H(\omega)(S_{opt}(\omega) + S_{SB}(\omega)), \quad (6.9)$$

where $H(\omega)$ is the frequency-domain cavity filter function [95, 203, 204]. Thus, from Equation 6.9, the emission spectrum has two main components. One is a purely optical component and is given by:

$$S_{opt}(\omega) = B^2 \int_{-\infty}^{+\infty} g_{opt}^{(1)}(\tau) e^{-i\omega\tau} d\tau. \quad (6.10)$$

This part includes coherent and incoherent contributions to the spectrum. The second component, S_{SB} , is a completely incoherent component given by:

$$S_{SB}(\omega) = \int_{-\infty}^{+\infty} (\mathcal{G}(\tau) - B^2) g_{opt}^{(1)}(\tau) e^{-i\omega\tau} d\tau. \quad (6.11)$$

This component is attributed to non-Markovian phonon relaxation and leads to the phonon sidebands in the emission spectrum [95, 99].

Both the optical and sideband components show a dependence on the square of the Franck-Condon factor ($B < 1$). The origins of the Franck-Condon factor are shown in Figure 6.5. The bulk lattice around the QD has a different configuration dependent on whether the QD is in the ground $|0\rangle$ or excited $|X\rangle$ state. Both of these lattice configurations have their own wavefunctions. The Franck-Condon factor is defined by the overlap between the two wavefunctions. The probability that the system will emit

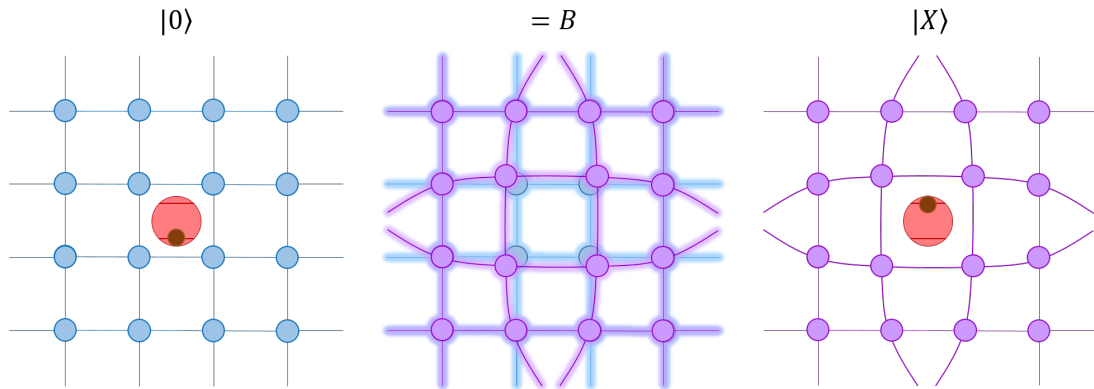


Figure 6.5: Origin of the Franck-Condon factor: The ground $|0\rangle$ and excited $|X\rangle$ states of the QD have different lattice configurations. The Franck-Condon factor B corresponds to the overlap of the two lattice configurations. Figure adapted from Iles-Smith et al. [95].

through the ZPL is B^2 and the probability that the system will instead emit through the PSB is given by the missing fraction of the ZPL, $(1 - B^2)$ [95].

The theory curve (solid line) plotted on Figure 6.4(b) shows good agreement with the experimental data (triangles). A broad PSB is seen, which is expected due to the short timescale of the phonon dynamics. Both the time domain and frequency domain measurements show that even in the low power regime well below saturation, where the excited state population is small, there is still a PSB visible that makes up $\sim 6\%$ of the emission.

6.4 Effect of Excitation Power on the Phonon Sideband

As was shown in Section 6.3, the phonon sideband persists in the low excitation power coherent scattering regime. To further investigate the effect of \mathcal{S} on the PSB, the RF spectrum is measured for a range of excitation powers using both high and low resolution spectroscopy.

6.4.1 Experimental Method

The low resolution spectra are measured using the 1200 l mm^{-1} grating of the spectrometer where the PSB can clearly be seen when the spectra are plotted on a semi-log scale. High resolution spectroscopy on the zero-phonon line (ZPL) is performed using a Fabry-Pérot interferometer (FPI) by John O'Hara and Alistair Brash. The Fabry-Pérot has a resolution of 67 MHz ($\sim 0.3 \text{ } \mu\text{eV}$) and free-spectral range (FSR) of 10 GHz ($\sim 40 \text{ } \mu\text{eV}$). By scanning the narrow transmission window of the FPI across the entire FSR, the lineshape of the collected emission can be mapped out. Before the emission reaches the FPI, the spectrometer is used to filter the emission centred on the ZPL. The filter bandwidth FWHM of spectrometer is $96 \text{ } \mu\text{eV}$. The filter is centred by monitoring the emission power after the spectrometer and adjusting the grating angle. The throughput power is maximised when the ZPL is centred through the filter.

The neutral exciton transition of the QD is again excited resonantly ($\Delta_{\text{LX}} = 0$) above the H1 cavity with the M-Squared Ti:S. The emission is also collected from the same position. The cross-polarised RF technique described in Section 3.4 is used to suppress the scattered laser. The excitation power is calibrated using Equation 6.3. A power dependence is measured with the laser being re-suppressed between each measurement to maximise the signal-to-background ratio.

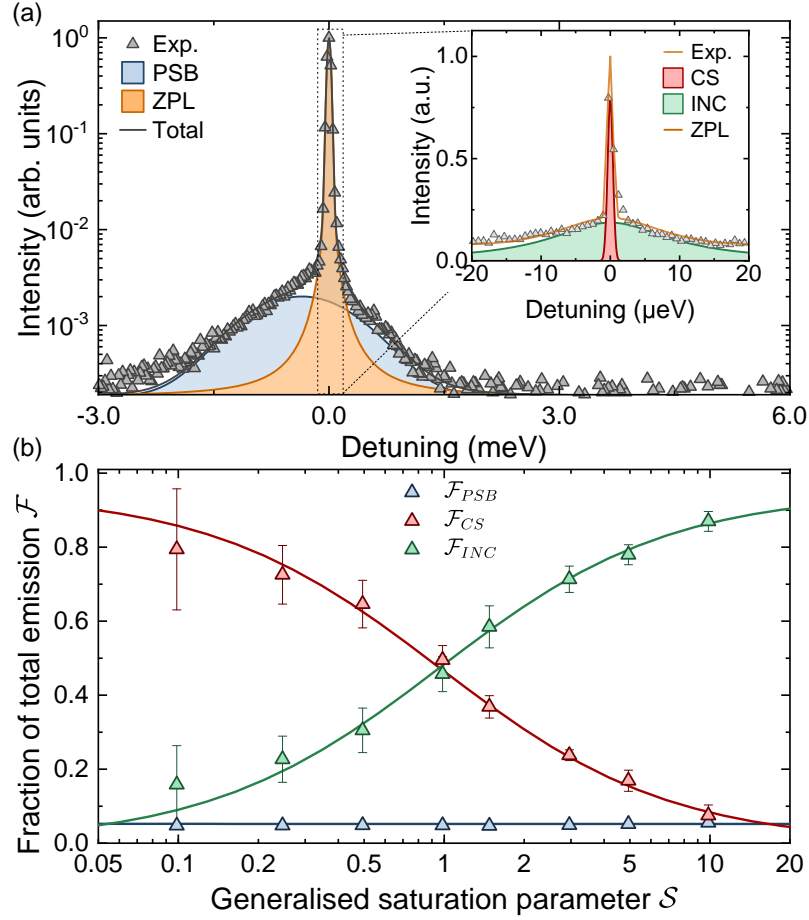


Figure 6.6: Resonance fluorescence spectral components: (a) Low resolution spectrum, measured at $S = 10$, plotted on a semi-log scale where grey triangles are the experimental data, blue is the fit to the PSB, orange is the fit to the ZPL and the grey line is the total fit. *Inset*: High-resolution spectrum of the ZPL using a Fabry-Pérot interferometer. The grey triangles are the experimental data; the fit for the coherent scattering is shown in red and for the incoherent RF in green. The total fit for the ZPL is shown by the yellow line, this is higher than the incoherent fit as the measured spectra contains contributions from the incoherent part of two neighbouring FSRs. (b) The evolution of the RF emission with increasing Ω . Triangles show the experimental data where blue gives the fraction of the total emission given by the phonon sideband, red gives the coherent scattering fraction and green the incoherent emission fraction. The solid lines show the theory predictions made using the polaron ME model.

6.4.2 Results and Theory

Figure 6.6(a) shows a typical spectrum of the resonance fluorescence emission from the QD measured using both low and high resolution spectroscopy when $\mathcal{S} = 10$. The PSB can clearly be seen in the low resolution spectrum (grey triangles) as it is plotted on a semi-log scale. The Gaussian fit to the PSB is shown in blue. The ZPL (orange) is fitted using a Voigt function. The Voigt function is used as it can incorporate the Gaussian IRF from the spectrometer, which here was measured to have a FWHM of $68 \mu\text{eV}$. The solid grey line shows the combined PSB and ZPL fits. The areas (A) of these components are used to evaluate the PSB fraction (\mathcal{F}_{PSB}):

$$\mathcal{F}_{PSB} = \frac{A_{PSB}}{A_{PSB} + A_{ZPL}}. \quad (6.12)$$

The inset to Figure 6.6(a) shows the high resolution FPI spectrum (grey triangles) of the QD ZPL. The broad component (green) is the contribution from the incoherent resonance fluorescence, the linewidth of which is governed by the transition coherence time T_2 . The narrow component (red) is the contribution from the coherent scattering. The natural linewidth of the incoherent component is defined as $1/T_1$. Here the linewidth is $\sim 25 \mu\text{eV}$ which is comparable to the $\sim 40 \mu\text{eV}$ FSR of the FPI. The broad incoherent scattering component is fitted using a Lorentzian to find A_{INC} . The narrow coherent scattering component (A_{CS}) is fitted using a Gaussian as the observable linewidth is limited by the IRF of the Fabry-Pérot of $\sim 0.5 \mu\text{eV}$. The fraction of the total emission that is contributed by each component can then be calculated using the following equations:

$$\mathcal{F}_{CS} = \frac{A_{CS}}{A_{CS} + A_{INC}} \frac{A_{ZPL}}{A_{PSB} + A_{ZPL}}, \quad (6.13)$$

and:

$$\mathcal{F}_{INC} = \frac{A_{INC}}{A_{CS} + A_{INC}} \frac{A_{ZPL}}{A_{PSB} + A_{ZPL}}. \quad (6.14)$$

6 Phonon Effects on QD Emission

Figure 6.6(b) shows the calculated fractions (\mathcal{F}) plotted against \mathcal{S} . The RF ($\Delta_{LX} = 0$) emission evolves from coherent scattering to incoherent emission as the excitation power is increased, as would be expected from Equation 6.2. Figure 6.6(b) also shows that the polaron model (lines) agrees well with the experiment. However, it can be seen that the coherently scattered fraction does not reach unity at vanishingly small \mathcal{S} . This result has been previously predicted [99] and is accounted for by the fraction of the emission that is emitted through the phonon sideband (\mathcal{F}_{PSB}). Figure 6.6(b) shows a constant \mathcal{F}_{PSB} of $\sim 6\%$ that is independent of Ω .

The origin of the constant \mathcal{F}_{PSB} is illustrated in Figure 6.7. The ground ($|0\rangle$) and excited ($|X\rangle$) states of the optical transition are dressed by vibronic bands which correspond to the emission or absorption of an LA phonon. In the limit of $\Omega \rightarrow 0$, coherent scattering dominates, with a probability defined by the square of the Franck-Condon factor, B^2 . Coherent scattering, also known as resonant Rayleigh scattering, is illustrated in Figure 6.7(a). However, due to phonon coupling there is also a finite probability that the scattering event will end in a different vibrational state of the ground-state manifold. This is illustrated in Figure 6.7(b) where the probability to finish in a different vibrational state is given by $(1 - B^2)$. Inelastic Stokes scattering occurs when a lower energy photon is emitted, and a phonon is emitted to correct the energy difference and reach the ground state. Anti-Stokes scattering occurs when a high energy photon is accompanied by absorption of a LA phonon. At 4.2 K, emission of a phonon is more likely than absorption, leading to the asymmetry of the phonon sideband seen in Figure 6.6. As the probability of whether the scattering is Rayleigh or Stokes/Anti-Stokes depends only on a constant B , then there is always a constant PSB contribution even at vanishingly small Ω .

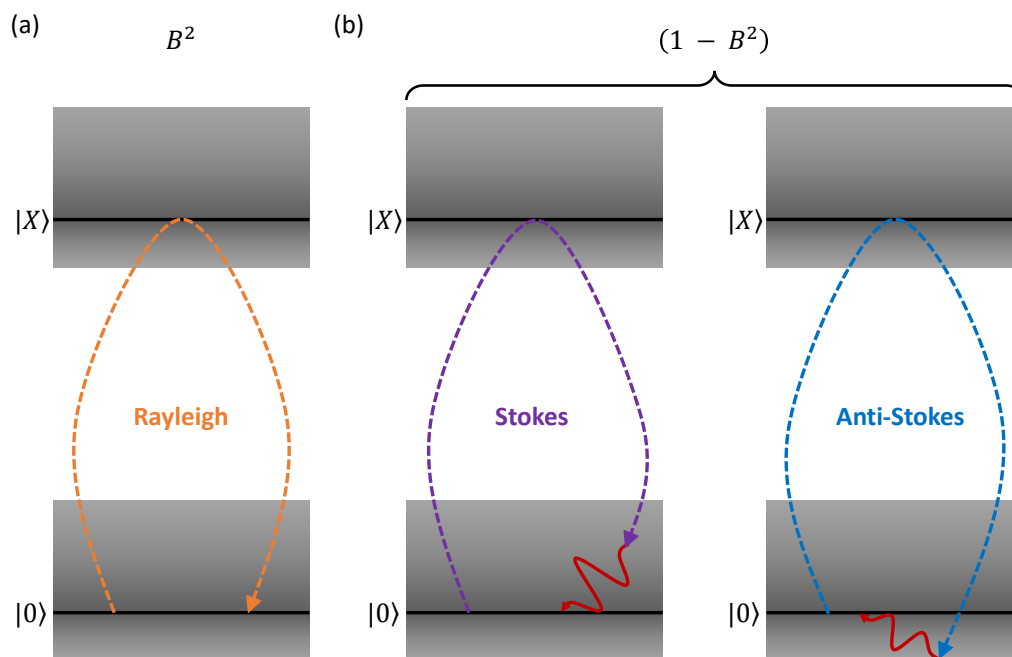


Figure 6.7: (a) Coherent scattering (orange-dashed) between the bare ground ($|0\rangle$) and excited ($|X\rangle$) states (solid lines) occurs with a probability given by the Franck-Condon factor squared (B^2). (b) The ground and excited states are dressed by phonon coupling, giving rise to a manifold of vibrational states (grey shading). The probability of inelastic scattering ending at a different vibrational state of the ground-state manifold is given by $(1 - B^2)$. The energy difference is carried by the emission or absorption of an LA phonon (red-solid) in Stokes (purple-dashed) or Anti-Stokes (blue-dashed) scattering processes respectively.

6.5 Phonon Effects in Detuned Coherent Scattering

As well as investigating the influence of phonons on the coherent scattering using resonant excitation, investigations were also carried out into the effect of detuning the excitation laser away from the emitter.

6.5.1 Experimental Method

To investigate the effect of detuning, two types of measurements were made. The first involved measuring spectra using the spectrometer 1200 l mm⁻¹ grating. The M-Squared CW Ti:S laser is used to excite the QD with $\hbar\Omega = 5.7 \mu\text{eV}$. The power is calibrated using the method described in Section 3.7.2 when the excitation laser is resonant with the neutral exciton transition. The M-Squared is then detuned from $\Delta_{LX} = 0$, the background laser scatter is suppressed, and spectra are recorded.

The second method used in this section investigates how the coherent fraction of the emission changes with detuning. The coherent fraction (\mathcal{F}_{CS}) is found using the $g^{(1)}(t)$ method previously described in Section 6.3. However, rather than measuring the fringe contrast at a large range of delay times, finding the coherent fraction only requires the fringe contrast value at time-zero (t_0) and at a time when the $g^{(1)}(t)$ is dominated by coherent emission, in the case of this measurement at 1 ns. The coherent fraction is given by:

$$\mathcal{F}_{CS} = \frac{v_{1\text{ns}}}{v_{t_0}}. \quad (6.15)$$

Here, v_{t_0} is the fringe contrast at time-zero and $v_{1\text{ns}}$ is the fringe contrast at 1 ns. Understanding how this can give the coherent fraction requires revisiting Figure 6.4(a), in which the parts of the $g^{(1)}(t)$ function given by \mathcal{F}_{PSB} , \mathcal{F}_{INC} and \mathcal{F}_{CS} are labelled, and:

$$\mathcal{F}_{PSB} + \mathcal{F}_{INC} + \mathcal{F}_{CS} = 1. \quad (6.16)$$

Looking at these components, it can be seen that Equation 6.15 is the equivalent of normalising the coherent component to the sum of all contributions:

$$\mathcal{F}_{CS} = \frac{\mathcal{F}_{CS}}{\mathcal{F}_{CS} + \mathcal{F}_{INC} + \mathcal{F}_{PSB}}. \quad (6.17)$$

To allow for any time dependent drifts, five measurements of the fringe contrast are made at each time point, alternately measuring at each delay stage position. The QD is excited with $\hbar\Omega = 25.6 \mu\text{eV}$ using the M-squared CW Ti:S. The laser is detuned by Δ_{LX} , the laser scatter is suppressed and the \mathcal{F}_{CF} is measured.

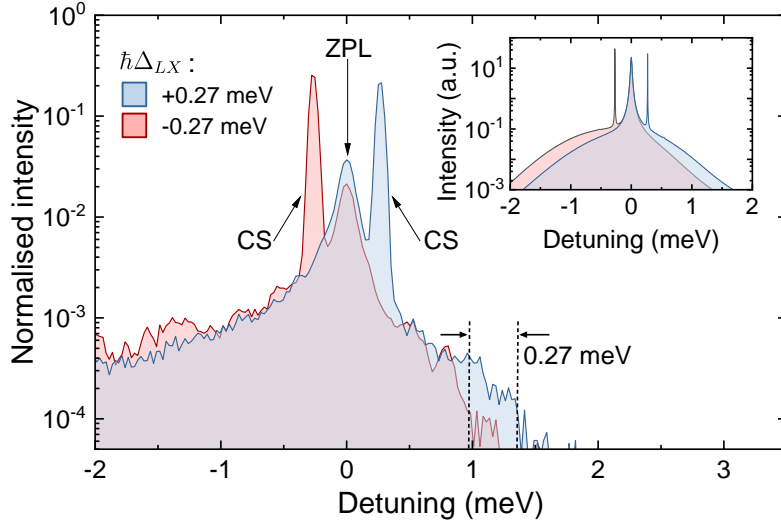


Figure 6.8: The influence of phonons on detuned coherent scattering. Semi-log spectra measured with the laser detuned from the **ZPL** by $\hbar\Delta_{LX} = \pm 0.27$ meV (blue/red) at a constant $\hbar\Omega = 5.7$ μ eV. The coherent scattering (CS) peaks are separated from the incoherent **ZPL**. The spectra have been normalised by the integrated intensity. *Inset*: Theoretical spectra showing the shift of the **PSB** under the same excitation conditions.

6.5.2 Results and Theory

Spectroscopy Measurements

Figure 6.8 shows, on a semi-log plot, spectra of the **QD** when excited with a **CW** laser with a constant $\hbar\Omega$ of 5.7 μ eV. Two spectra are shown in Figure 6.8 with a laser detuning of $\hbar\Delta_{LX} = \pm 0.27$ meV. The coherent scattering peaks, labelled “CS”, dominate the spectrum and are separated from the **ZPL**, which remains centred at zero detuning.

For the positive detuning (blue), it can be seen that the **PSB** is also shifted in the positive direction by ~ 0.27 meV. The origins of this shift comes from Equation 6.11, where the product between $(\mathcal{G}(\tau) - B^2)$ and $g_{opt}^{(1)}$ in the time domain, implies a convolution in frequency between the purely optical spectrum and the frequency-space

6 Phonon Effects on QD Emission

phonon correlation function. This implies that all optical features have an associated phonon sideband. The positive detuned spectra shows a +0.27 meV shift in the PSB for the coherent scattering with respect to the PSB for the ZPL which was measured when $\Delta_{LX} = -0.27$ meV. The PSB for the ZPL has the same position in both spectra. It would be expected for the negative detuned spectra to show a -0.27 meV difference from the negative side of the ZPL. Experimentally this shift is obscured by weak incoherent backgrounds that occur due to the low counts rates experienced when exciting with a large Δ_{LX} , here the QD signal is $\sim 50x$ weaker than when using resonant excitation. The inset to Figure 6.8 shows theoretical spectra calculated under the same conditions, here the shift in the phonon sideband associated with the coherent scattering component can clearly be seen for both positive and negative detunings. The agreement between experiment and theory for positive detunings in Figure 6.8 confirms the interpretation of the product in Equation 6.11, suggesting that all optical features have a associated phonon sideband.

Detuned Coherent Fraction

Figure 6.9 shows the \mathcal{F}_{CS} (grey triangles) found by applying Equation 6.15 to detuned $g^{(1)}(t)$ measurements. Due to the low count rates when measuring far-detuned from the ZPL, the main source of error in \mathcal{F}_{CS} is shot noise from the detectors. This leads to the error bars on Figure 6.9 increasing at larger detunings from the ZPL ($\Delta_{LX} = 0$). Both the predictions from the atomic model (green) and the polaron ME (red) are plotted on Figure 6.9. The coloured areas of the theoretical models are the confidence bounds given by the experimental uncertainty in Ω . Again, a clear deviation away from the monotonic increasing of \mathcal{F}_{CS} with detuning predicted by the atomic model is seen in the experimental data. The initial increase of \mathcal{F}_{CS} shown in the data is predicted by both theoretical models. This increase is caused by the phonon interaction being weaker close to zero detuning [205] and so the atomic interaction dominates. As the detuning increases in either direction, the coherent fraction starts to decrease. This decrease occurs due to excitation-induced dephasing (EID) which arises from

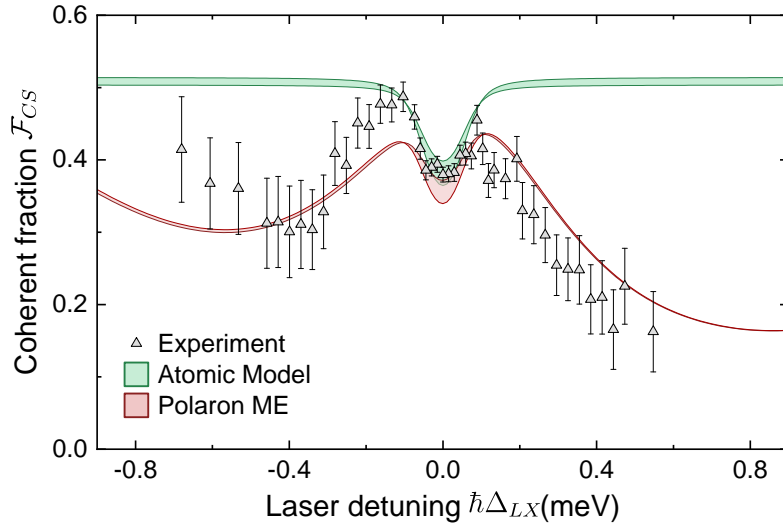


Figure 6.9: The influence of phonons on detuned coherent scattering. The coherent fraction (\mathcal{F}_{CS}) is measured at different laser detunings (Δ_{LX}), using a constant $\hbar\Omega$ of $25.6 \mu\text{eV}$. The grey triangles show the experimental data. The green and red areas show respectively the atomic and polaron ME model predictions. The areas represent the uncertainty in the experimental Ω , and both models include additional pure dephasing and spectral wandering corrections.

LA phonon mediated transitions between the dressed states of an optically excited emitter [96, 206]. As the rate of the EID is proportional to $(\Omega^2 + \Delta_{LX}^2)$, the coherent scattering fraction \mathcal{F}_{CS} decreases as Δ_{LX}^2 increases.

Figure 6.9 can be understood by comparison with Figure 6.10. Again the “bare” ground ($|0\rangle$) and excited ($|X\rangle$) states are shown dressed by the phonon manifolds (grey). When $\Delta_{LX} > 0$ (green dashed arrow), an LA phonon (red arrow) can be emitted into the lattice. This allows the $|X\rangle$ state to become populated [205], increasing the probability of incoherent emission (purple arrow). This leads to a decrease in the coherent fraction (\mathcal{F}_{CS}) for $\Delta_{LX} > 0$ as seen in Figure 6.9.

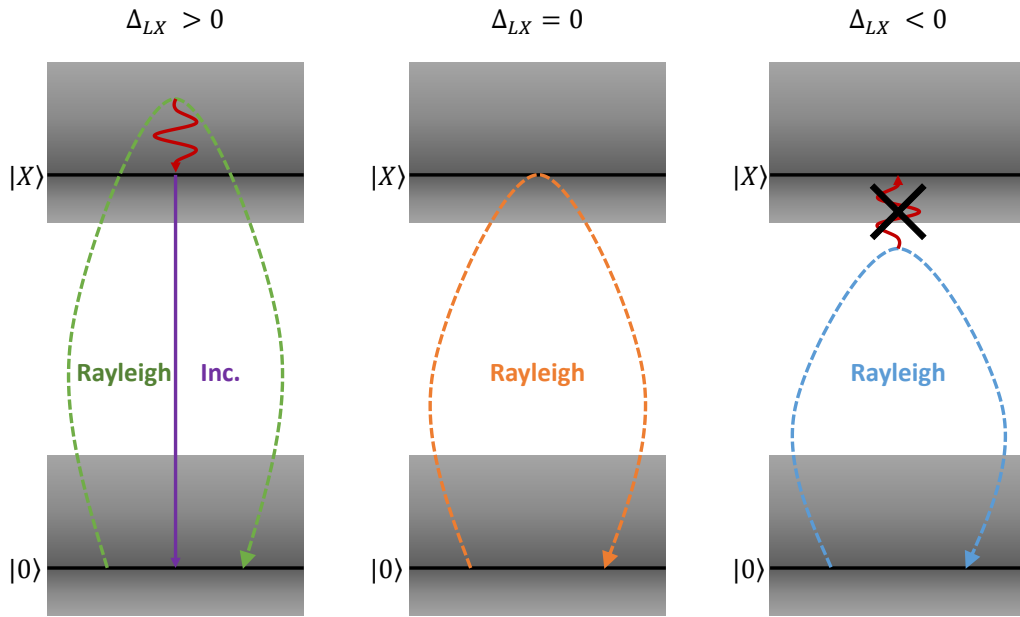


Figure 6.10: For $\Delta_{LX} > 0$, emission of an LA phonon can populate $|X\rangle$. This leads to an increased probability of incoherent emission, reducing the coherent fraction. For $\Delta_{LX} < 0$, population of $|X\rangle$ requires the absorption of an LA phonon which is a weak effect at 4.2 K. This limits the possibility of incoherent emission, and so the coherent fraction begins to increase again back towards the limiting atomic case.

For $\Delta_{LX} < 0$ (blue dashed arrow) to populate the $|X\rangle$ state requires the absorption of an LA phonon (red) from the lattice. However, at 4.2 K the probability of this occurring is low [184, 207, 208], inhibiting incoherent scattering. Also, due to the asymmetry of the phonon manifold [184, 205], the laser detuning exceeds the cut-off energy for phonon coupling for significantly smaller detunings than when $\Delta_{LX} > 0$. This leads to a recovery of \mathcal{F}_{CS} back towards the limiting atomic case at larger negative detunings. Resulting in the clear asymmetry seen in the experimental data of Figure 6.9, the behaviour of which is well modelled by the polaron ME.

Corrections to the Polaron and Atomic Models

Both the atomic and polaron models shown in Figure 6.9 have been corrected for the QD system used here. When driving off resonance, both the atomic and polaron models significantly overestimate the coherent fraction that is seen in the experiment. Here, this has been attributed to pure dephasing originating from charge noise generated by the reduced scattering cross-section of the QD when exciting off resonance. The reduced scattering cross-section allows the detuned laser to be absorbed by the doped bulk material instead [209]. Figure 6.4 shows strong agreement between the polaron model (with zero pure dephasing) and the experimental data when driving resonantly. It is therefore suggested that the effect of the pure dephasing only becomes significant at large detunings, where the absorption cross-section of the QD reduces.

To capture the detuning-dependent dephasing in both the atomic and polaron models, a Lorentzian detuning-dependent dephasing term:

$$\gamma(\Delta_{LX}) = \gamma_{\max}(1 - \xi^2/(\Delta_{LX}^2 + \xi^2)), \quad (6.18)$$

is used to represent the reducing QD absorption cross-section, where ξ is the natural linewidth of the QD. When the polaron ME model, with this extra term, is fitted to the experimental data shown in Figure 6.9, an amplitude of $\gamma_{\max} = 21 \pm 0.1 \mu\text{eV}$ is found. Figure 6.11(a) shows the modelled detuning-dependent pure dephasing rate, with Figures 6.12(a) and 6.12(b) showing the dephasing term applied to the polaron (red dashed) and atomic (green dashed) models respectively; the original models are plotted with dotted lines.

As well as overestimating the coherent fraction at large detunings, both models also produce a dip at $\Delta_{LX} = 0$ which is significantly narrower than what is observed in the experimental data. The suggested reason for this is spectral wandering of the

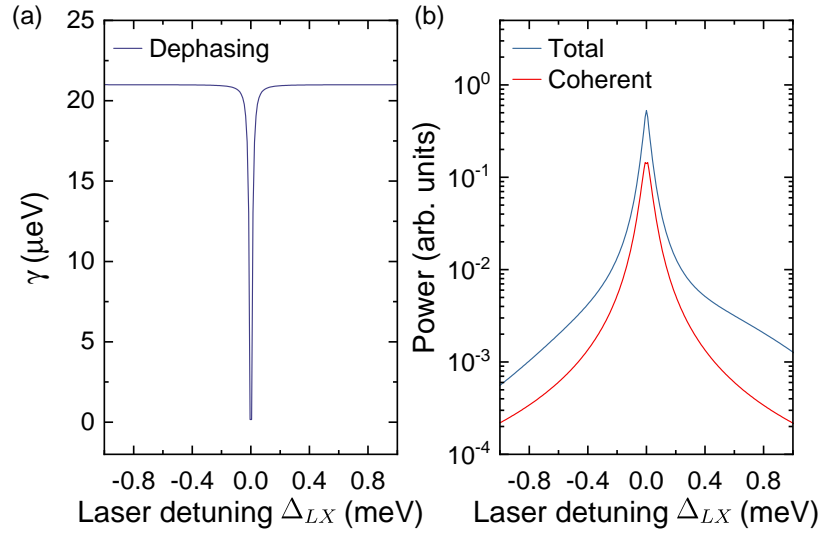


Figure 6.11: (a) Theory plot of the detuning-dependent dephasing rate $\gamma(\Delta_{LX})$. (b) Theory plot of the total (blue) and coherent (red) powers of the QD emission from the polaron model.

QD, on a timescale $\gg T_2$, due to the charge environment around the QD. In Section 5.3.4, a reduction in Hong-Ou-Mandel visibility for this sample was observed on the timescale of tens of nanoseconds [106], inferring the presence of such spectral wandering. The effect of spectral wandering is to give a time-varying detuning between the QD and the laser, meaning that the resulting spectrum contains contributions from multiple detunings that are weighted according to the noise function associated with the wandering. To account for the spectral wandering, the polaron and atomic models are convolved with a Gaussian noise function. The FWHM of the Gaussian noise function is found to be $66 \mu\text{eV}$ by fitting the incoherent peak of detuned spectra, for example, the spectra shown in Figure 6.8. The incoherent peak is fitted with a Voigt function whose Lorentzian width is set to be the natural linewidth of the QD. To include these effects in the theoretical model, the detuning-dependence of the coherent and incoherent power scattered by the QD (Figure 6.11(b)) is convolved with this noise function. From these plots, \mathcal{F}_{CS} is then calculated according to Equation 6.15 as before, producing the solid curves in Figure 6.12.

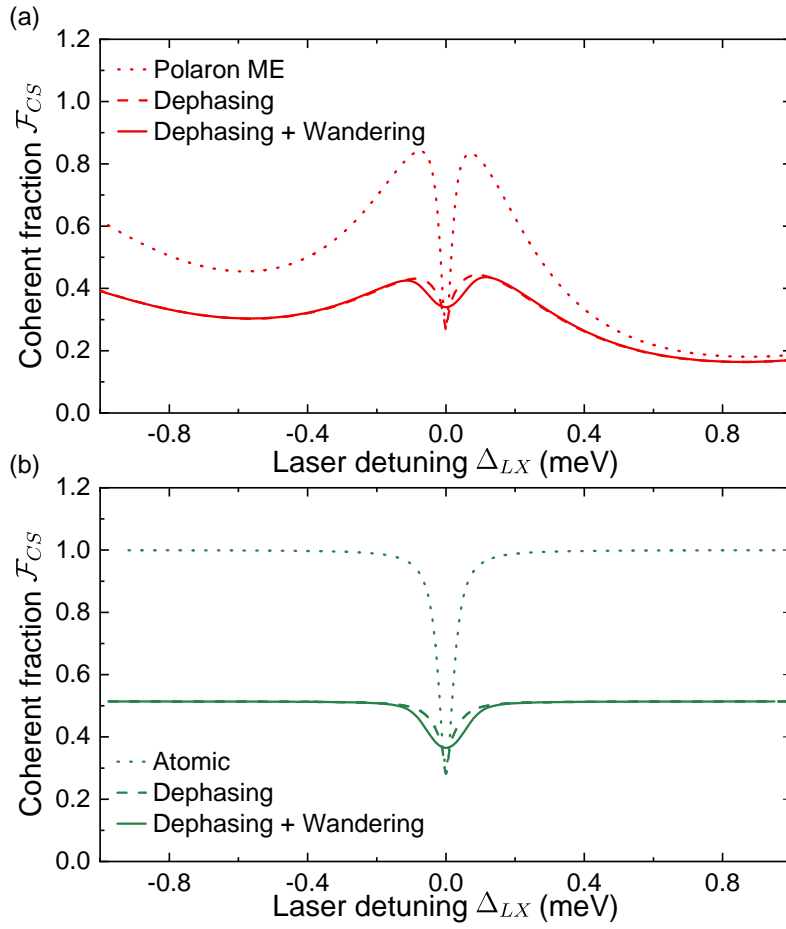


Figure 6.12: (a) Theory plot of the coherent fraction \mathcal{F}_{CS} against the laser detuning (Δ_{LX}) predicted by the polaron model (dotted). The effect of pure dephasing ($\gamma(\Delta_{LX})$) and the effect of pure dephasing with spectral wandering are shown with dashed and solid lines respectively. (b) Theory plot of the coherent fraction \mathcal{F}_{CS} against the laser detuning (Δ_{LX}) predicted for the atomic model (dotted). Again the dashed and solid lines shown the pure dephasing and pure dephasing with spectral wandering corrections respectively.

Figure 6.11(b) shows the emitted power of the QD against the laser detuning (Δ_{LX}) calculated using the polaron model, illustrating why a detuned spectra is used to quantify the spectral wandering. Figure 6.11(b) is plotted on a semi-log scale. When the QD is excited resonantly ($\Delta_{LX} = 0$), any wandering results in a sharp drop in the emitted intensity from the QD due to the steep gradient. Consequently, any spectral wandering has very little effect on the QD spectra measured as the resonant emission dominates and any wandering is effectively converted to blinking. However, away from resonance the gradient of the emitted power is shallower, so the full wandering distribution contributes to the spectrum. It can also be seen from Figure 6.11(b) that the coherent emission from the QD is symmetrical with detuning but that the total emission is asymmetric, demonstrating the reduction in phonon-mediated emission at negative detunings, which leads to the recovery of the coherent scattering fraction. Figure 6.12 shows how convolving spectral wandering with the polaron model and atomic model, both of which have already been corrected for the detuning-dependent pure dephasing, broadens the central dip. It is important to note from Figure 6.12 that these corrections only serve to capture additional effects observed in experiments, they do not change the qualitative features of the two models. The solid curves in Figure 6.12 incorporating both pure dephasing and spectral wandering are shown with the experimental data in Figure 6.9.

6.6 Conclusion

The results in this chapter show that, for a solid-state emitter, a fixed fraction of the emitted light is always lost through the phonon sideband. The PSB is present regardless of excitation power or detuning. The presence of the phonon sideband is demonstrated through both first-order correlation ($g^{(1)}(t)$) measurements and the use of spectroscopy. These results are modelled using a polaron ME approach which shows excellent agreement with the measured QD properties. The presence of the

PSB is fundamentally incompatible with atomic model physics where there is no coupling of the emitter to its surroundings, demonstrating the importance of using accurate modelling of solid-state emitters to include their environment.

The polaron ME model is then used to explain the fixed fraction shown experimentally to be emitted through the PSB regardless of the Rabi frequency (Ω). The PSB area depends solely on the Franck-Condon factor (B); the probability that a photon will be emitted into the ZPL is B^2 , leaving a $(1 - B^2)$ probability that the emission will involve either the absorption or emission of a phonon. The presence of a PSB whose area is independent of Ω supports theoretical work that predicts the presence of a PSB even at vanishingly weak resonant driving [99].

CW detuning measurements of the emitted spectra from the QD show that all features of the emission have an associated PSB with the total area of the PSBs still governed by $(1 - B^2)$. Here, a PSB was observed both for the ZPL when exciting detuned but also for the coherently scattered photons which have a frequency equal to the laser frequency. This phenomenon is described within the polaron ME model, where a frequency-domain convolution between the optical and PSB components of the spectrum is found. Measurements of the coherently scattered fraction of the emission (\mathcal{F}_{CS}) with detuning also show the strong influence of phonons. \mathcal{F}_{CS} cannot be described by the monotonic increase with increasing detuning that is predicted by the atomic model. These effects can, however, be understood by applying phonon dressing to the “bare” optical transition and modelling the system using the polaron ME. These measurements also illustrate the asymmetry of the phonon coupling at 4.2 K, where emission of a phonon is more likely than absorption. This asymmetry allows the cut-off for phonon coupling to be exceeded for negative detuning, causing the coherent fraction to tend back towards the limiting atomic case for large negative detunings.

6 Phonon Effects on QD Emission

These results were measured using a QD, but are applicable to all solid-state emitters where interactions can occur with the environment. Understanding that these phonon effects are present in solid-state systems even under the conditions of vanishingly small excitation power or large detunings is important for the development of indistinguishable single-photon sources, as these processes can lead to a fundamental limit to the indistinguishability of the photons produced [95]. Furthermore, these phenomena are also important for a number of other quantum optics applications. For example in a spin-photon entanglement experiment based on coherent scattering from Zeeman split states [172], the atomic model suggests that the laser should be tuned to equal and opposite detunings from the two transitions. For solid-state emitters, the asymmetry in \mathcal{F}_{CS} observed in this chapter will lead to unequal scattering probabilities, compromising the entanglement fidelity. By reoptimising such schemes with an appropriate model of phonon interactions, optimal performance could be restored even in the presence of phonon interactions.

7 Spectral Filtering Effects on QD Resonance Fluorescence

The work presented in this chapter has been published in:

Catherine L. Phillips, Alistair J. Brash, Dara P. S. McCutcheon, Jake Iles-Smith, Edmund Clarke, Benjamin Royall, Maurice S. Skolnick, A. Mark Fox, and Ahsan Nazir.

“Photon Statistics of Filtered Resonance Fluorescence.” *Physical Review Letters* **125**, 043603 (2020).

Hanbury Brown and Twiss second-order correlation measurements were set up and carried out by Catherine Phillips and Alistair Brash, including the setting up, optimisation and use of all the spectral filters. The 4f tunable filter was built with the additional assistance of Kévin Seurre. Sensor theory modelling for the $g^{(2)}(t)$ and $g^{(2)}(0)$ measurements was performed by Ahsan Nazir, Dara McCutcheon and Jake Iles-Smith. The MATLAB simulations of the emission spectra, transmission coefficients and filtered fractions (\mathcal{F}) were performed by Catherine Phillips.

7.1 Introduction

Spectral filtering of the resonance fluorescence (RF) from a two level emitter (TLE) is commonly employed in quantum-optics experiments to improve the single-photon purity and indistinguishability. A single-photon source (SPS), where the emitted photons are indistinguishable, is necessary for measurements schemes where quantum

interference is required. For example, it is required for quantum simulators [210], boson sampling [27, 28], linear optical quantum computing [211] and quantum repeaters [212]. These schemes also require a high efficiency of single-photon production, where the SPSs are bright with a high collection efficiency.

The filters used in quantum-optics experiments are typically centred on the zero-phonon line (ZPL) of the emission and are used to remove residual backgrounds from the excitation laser [106, 155], other transitions [213] or phonon sidebands [213–215]. Whilst filtering out these components will improve the single-photon indistinguishability measured in HOM experiments, this always occurs at the cost of the efficiency [95]. Furthermore, as the bandwidth (Γ) of the filter approaches the natural linewidth (γ) of the ZPL, theory has predicted that the measured photon statistics of the RF emission are strongly modified in both the weak (coherent scattering) [216, 217] and strong (Mollow) driving regimes [218].

This chapter presents a joint experimental and theoretical investigation into the influence of filtering RF with bandwidth comparable to the natural linewidth. Hanbury Brown and Twiss (HBT) $g^{(2)}(0)$ experiments are used to measure the photon statistics of spectrally filtered QD RF. Both the low and high power driving regimes are investigated using a range of spectral filters with different Γ . Simulations of the components of the emission after filtering provide insight into the observed modifications of the photon statistics. The experimental results show excellent agreement with an extended theoretical model based on the sensor formalism.

7.2 Filtering QD emission

For the following measurements the QD, described in Chapter 4, was slightly detuned from the cavity, leading to a Purcell Factor of 30, which gives a broad natural line width (γ) of 20 μeV . This enables spectral filtering of the QD RF emission with a

bandwidth (Γ) smaller than γ . Five different filters are used to filter the RF emission. Four of the filters have a fixed spectral bandwidth (Γ) whereas the fifth filter has a tunable Γ . The values of Γ used are shown in Table 7.1. The following section describes the filters and how Γ was measured.

4f Tunable Filter

Figure 7.1 is a schematic diagram of the 4f tunable filter. This filter has both a tunable Γ and centre wavelength. The 4f tunable filter uses the same principles as the 4f pulse shaper (Fig. 3.2) used with the Mira Ti:S pulsed laser but in a more compact folded geometry. The transmission grating splits the emission into its spectral components. A cylindrical lens is mounted one focal length (f) after the grating, focusing the diverging, spectrally separated emission at the Fourier plane located one focal length after the lens. In this plane, each position corresponds to an optical frequency of the input beam. Therefore, by placing an adjustable slit in the Fourier plane, certain wavelengths of light can be transmitted while others are removed from the emission. The filtered emission is then reflected back through the cylindrical lens and is focussed on the grating. The spectral components are recombined at the transmission grating and the filtered emission is recoupled into a single-mode fibre. Unlike the 4f pulse shaper, which uses two gratings spaced $4f$ apart, the 4f filter has a folded geometry and only uses one grating. This means that the filter has a smaller spatial footprint as the filter only needs to be $2f$ long.

The folded geometry is also advantageous for alignment. In a 4f geometry the second grating recombines the spectral components that were spatially separated by the first grating. The quality of the recombination is quantified by the spectro-spatial overlap of the filtered beam after the second grating. Perfect spectro-spatial overlap occurs when the grating perfectly reverses the splitting caused by the first grating. The spectral splitting depends on the first grating's angle and tilt with respect to the input beam. For the second grating to reverse the splitting requires having the same grating

7 Spectral Filtering Effects on QD Resonance Fluorescence

Filter	Bandwidth Γ (μeV)
Free-space Fabry-Pérot - Thorlabs SA210-8B	0.25
Etalon - Light Machinery 1.6mm fused silica	5.8
Fibre Fabry-Pérot - Micron Optics FFP-TF2	17
1200 l mm^{-1} grating spectrometer - Princeton	97
4f tunable filter	454
4f tunable filter	3051

Table 7.1: Bandwidth (Γ) of spectral filters.

angle and tilt with respect to the beam as the first grating. The spectro-spatial overlap after the second grating can be checked by moving a beamblock laterally through the Fourier plane of the filter and viewing the emission after the grating on an IR card. For perfect spectro-spatial overlap, blocking part of the beam only affects the intensity of the observed beam. If the spectro-spatial overlap is not optimised, moving the beamblock will cause the observed spot to move. This occurs as the separated spectral components in the Fourier plane are being focussed at different points on the grating. Herein lies the advantage of the folded geometry; by travelling through the same grating, the input and output beams have the same angles, provided that both beams have vertical alignment on the grating and that the grating is level in the horizontal direction.

The resolution of diffraction gratings is given by:

$$\Delta\lambda = \frac{\lambda}{mN}, \quad (7.1)$$

where $\Delta\lambda$ is the smallest resolvable difference in the wavelength, m is the diffraction order and N is the number of illuminated grooves. Therefore, to maximise the resolution by optimising N , a 1500 l mm^{-1} transmission grating is used, with the optics before the grating designed to fill the width of the grating with collimated emission. The tilted mirror provides a vertical displacement between the input and

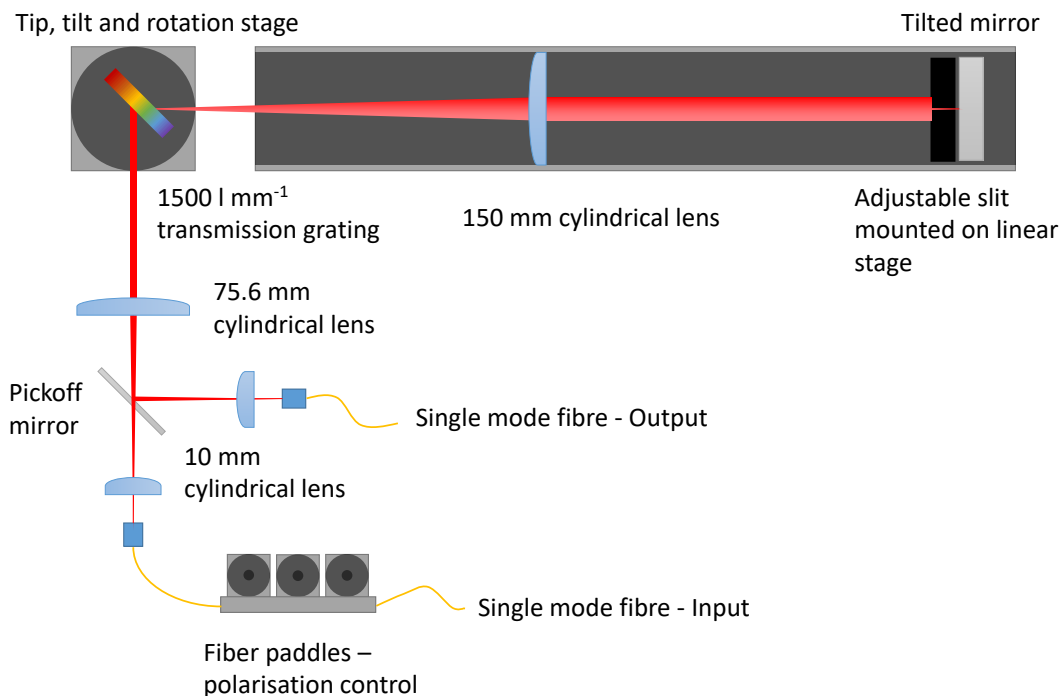


Figure 7.1: Schematic of the filter with tunable centre wavelength and filter bandwidth achieved by using a 4f pulse shaper design with a 1500 l mm^{-1} transmission grating.

output beams, allowing a semicircular pickoff mirror to be used to divert the filtered emission so that it can be recoupled into the fibre. It is due to the vertical displacement and the large beam waist that pairs of cylindrical lenses are used for the fibre coupling. If spherical lenses are used, then filling the lens and having a vertical offset from the centre of the lens causes spherical aberration in the beam. This spherical aberration leads to the beam having a crescent shape when viewed in the far field, reducing the efficiency with which it can be coupled in to single-mode fibre. Using a pair of cylindrical lenses to collimate the beam onto the transmission grating also allows the beam shape to be modified so that it is wide in the x-axis but narrow in the y-axis. This allows greater resolution, as the width of the rectangular grating, 5 cm wide by 1 cm tall, can be filled without a loss in throughput efficiency.

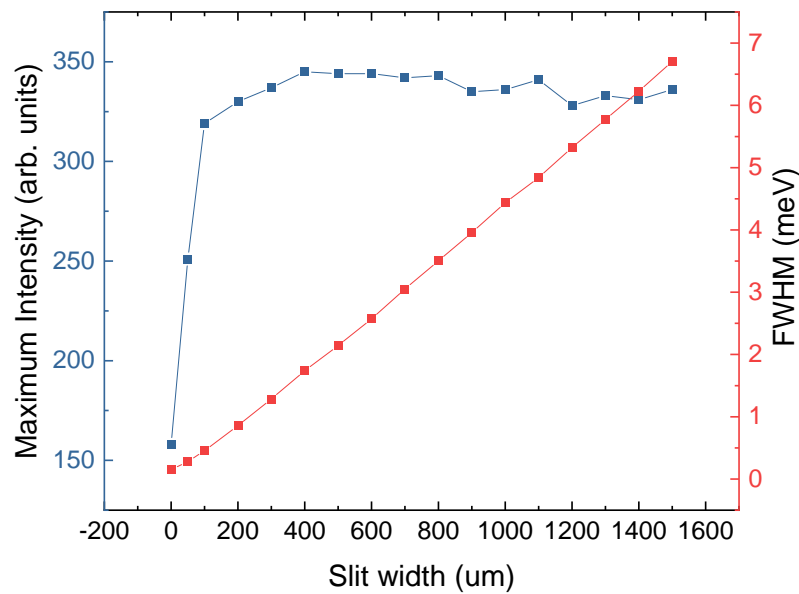


Figure 7.2: Transmission of a broadband tungsten-halogen white light source through the 4f tunable filter at different slit widths. The transmission bandwidth (red) shows a linear relationship with increasing the micrometer slit width of the filter. The maximum intensity through the filter (blue) begins to decrease when the slit width is reduced below 100 μm .

The throughput efficiency of the tunable filter using a CW laser at the QD resonant wavelength is 30%. The transmission grating has a small polarisation dependence. Fibre paddles set in quarter-wave, half-wave and quarter-wave plate configuration, respectively, are used to adjust the input polarisation to maximise the throughput of the filter.

The 4f tunable filter was characterised using a fibre-coupled broadband white light source (Thorlabs - Stabilised Tungsten-Halogen Light Source). The output of the filter was connected to the spectrometer and spectra were taken at different micrometer slit widths; each division on the micrometer corresponds to a 10 μm change in the slit width. The two narrowest micrometer slit widths produced spectra that could be fit-

ted using a Gaussian function as the slit width becomes comparable to the diameter of the focal spot of a single frequency component in the Fourier plane. However, for slit widths wider than $50\ \mu\text{m}$, the spectra become top-hat in shape and so could not be fitted in the same way. Here the **FWHM** was measured by finding the wavelength halfway up the rising and falling edges of the top-hat spectra and taking the difference between these points.

Figure 7.2 (red) shows the results of the micrometer slit width dependence. The measurements show a linear dependence between the width of the slit and the transmitted bandwidth. As well as measuring the **FWHM** of the spectra, the maximum intensity of the spectra for each micrometer slit width was also analysed and is shown in blue on Figure 7.2. The intensity measurements show that the filter does not cause the transmitted signal to lose throughput intensity with slit width change, apart from at slit widths below $100\ \mu\text{m}$ ($454\ \mu\text{eV}$). This means that the slit does not clip the beam, implying that the filter is well aligned and the distance between the focussing lens and the slit is f , the focal length of the lens. In the following experiment, $454\ \mu\text{eV}$ is the smallest Γ used for the $4f$ tunable filter.

Spectrometer filtering

As well as being used to take spectra, the Princeton spectrometer can also be used as a spectral filter. The $1200\ \text{l mm}^{-1}$ grating is used to separate out emission into its different wavelength components and these are usually directed onto the **CCD** of the spectrometer. However, a diverting mirror can be flipped in front of the **CCD** to direct the separated emission out of an adjustable exit slit, where it can then be coupled back into a single-mode fibre. The Γ of the spectrometer filtering is governed by the width of the exit slit, as well as by the coupling of the filtered emission back into a single-mode fibre. The angle of the grating can be adjusted to change the central wavelength transmitted through the filter. The spectrometer's Γ was found by sending the attenuated Mira **Ti:S** pulsed laser through the spectrometer. The filtered

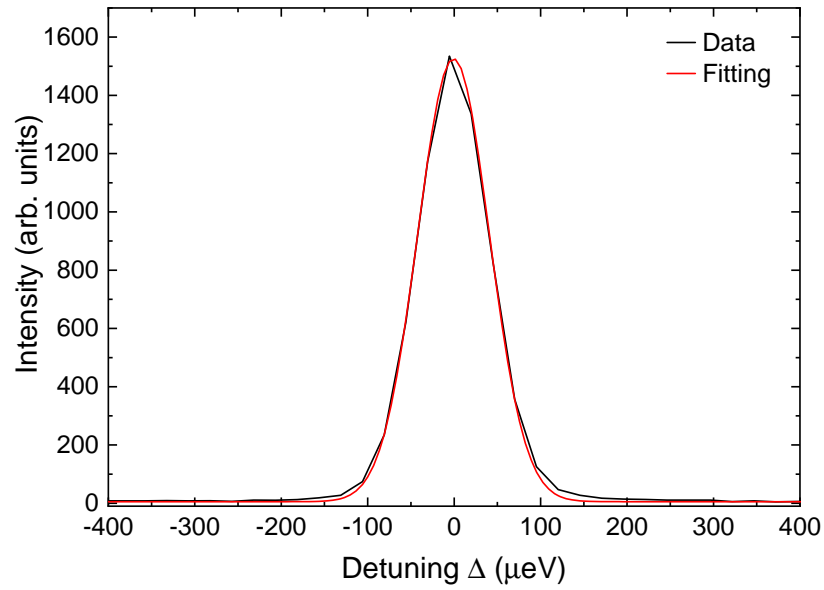


Figure 7.3: Transmission of the attenuated broad Mira Ti:S laser pulse through the Princeton spectrometer using the 1200 l mm^{-1} grating. The resulting spectra (black) is measured on a second spectrometer and fitted with a Gaussian (red). The Γ is the FWHM of the Gaussian, $97 \mu\text{eV}$.

emission was then measured on a second spectrometer and fitted with a Gaussian to give the Γ of $97 \mu\text{eV}$. The measurement is shown in Figure 7.3. The width of the exit slit was kept constant for all of the following measurements.

Etalon Filters

The bandwidth for the two Fabry-Pérot filters were found using the following equation:

$$\Gamma = \frac{FSR}{\mathcal{F}}, \quad (7.2)$$

where Γ is the spectral bandwidth of the filter, FSR is the free spectral range and \mathcal{F} is the Finesse of the cavity. The FSR and \mathcal{F} are supplied on the datasheets for both filters.

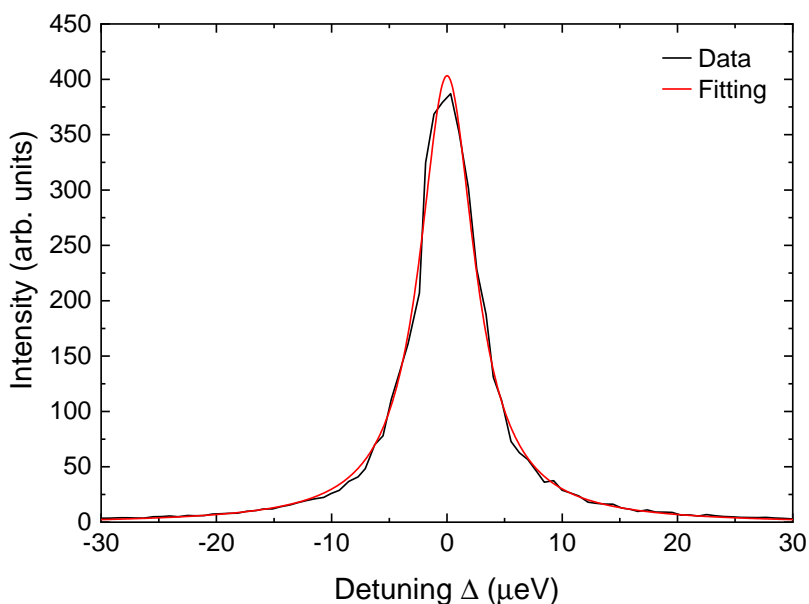


Figure 7.4: Transmission through the Light Machinery etalon measured by scanning the tunable M-Squared Ti:S CW laser. The M-Squared was stepped by 18 μm and the transmission recorded on a power meter. The resulting spectra (black) is fitted with a Lorentzian (red) to give a Γ of 5.8 μeV .

Fabry-Pérot interferometers have two high reflectivity mirrors that create a cavity. Constructive interference occurs when the distance between the mirrors is integer multiples of $\lambda/2$ and that wavelength (λ) is transmitted out of the far side of the cavity. Both of the Fabry-Pérot filters are scanning tunable interferometers. For the Thorlabs tunable Fabry-Pérot etalon, one of the mirrors is mounted on a piezo actuator so the cavity length can be tuned by applying a voltage to the piezo. The fibre Fabry-Pérot utilises a cavity created through the use of fibre Bragg mirrors rather than a free-space cavity.

Tunable Fabry-Pérots can be used to transmit a single narrow bandwidth or, by scanning through a free spectral range (*FSR*) of the etalon, to build up a broader high-resolution transmission spectra. Broad high resolution scanning using a Fabry-Pérot

7 Spectral Filtering Effects on QD Resonance Fluorescence

was shown in Section 6.4. To transmit the single narrow bandwidth, the required central transmission wavelength needs to be selected and locked. Locking the transmitted wavelength is achieved by continually adjusting the applied bias, keeping the transmitted signal maximised on a single-photon detector if the peak of the emission spectrum is the required centre wavelength. The filter output can also be monitored on a spectrometer if the centre wavelength required is not at the peak of the emission spectrum. For the following measurements, a narrow bandwidth was required, and the signal was locked by keeping the transmitted signal maximised.

The Light Machinery etalon is a 1.6 mm thick fused silica solid etalon. This type of etalon does not use mirrors separated by an air gap to create a cavity. Instead, it comprises a solid piece of silica with coated faces. Rather than tuning the centre wavelength of the filter by moving one of the mirrors, the etalon centre wavelength can be tuned by slightly changing the angle of the incident beam. The Γ of this filter was found by measuring the transmission as a function of wavelength of the M-Squared Ti:S CW laser through the etalon. The wavelength of the Ti:S was stepped by 18 pm and the resulting transmission peak, shown in Figure 7.4 was fitted with a Lorentzian to give a Γ of 5.8 μeV .

7.3 Weak Driving Regime

When using resonant continuous wave (CW) excitation and an emitter with a lifetime limited coherence time ($T_2 = 2T_1$), the weak excitation regime is defined as $\Omega_R^2 < (\gamma^2/2)$ where Ω_R is the Rabi frequency and is defined as $\gamma = 1/T_1$. This regime is often termed the Resonant Rayleigh Scattering (RRS) or Heitler Regime [49, 163, 219]. In this excitation regime the resonance fluorescence (RF) spectrum from a two-level system, such as a QD, has two components: a coherent part and an incoherent part. This was described in Section 6.2 but is reiterated here as an understanding of both components is essential for the following experiments. The origin of these two components

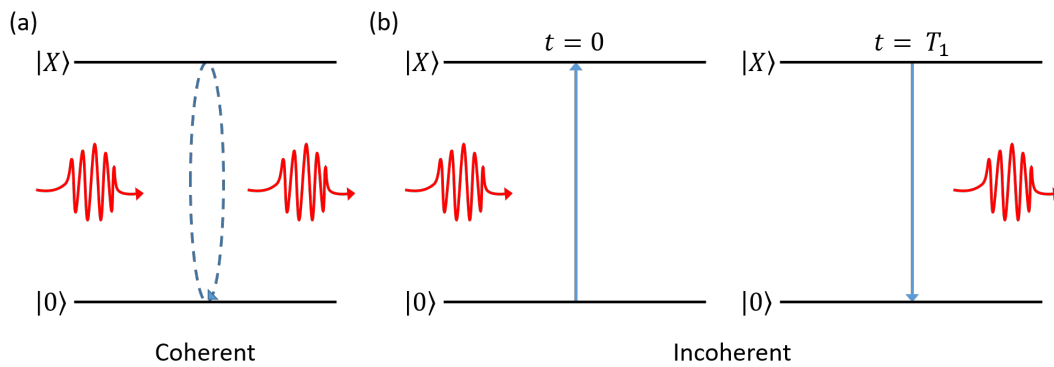


Figure 7.5: (a) Coherent scattering from a two-level emitter. (b) Incoherent emission from a two-level emitter; the laser photon is absorbed and populates the transition's excited state. The transition then relaxes due to spontaneous or stimulated emission on a timescale given by T_1 , emitting a photon with the energy of the transition.

is again shown in Figure 7.5. The coherent component, shown in Figure 7.5(a), comes from photons that are coherently scattered by the transition. Here, excitation and emission become a single coherent event and the elastically scattered photons retain the coherence of the excitation laser. This leads to a sub-natural linewidth which is characteristic of a long coherence time [49, 106, 160, 163, 164, 166]. The incoherent component, shown in Figure 7.5(b), occurs where a photon is absorbed, exciting the (TLE) from the ground ($|0\rangle$) to excited ($|X\rangle$) state. Then, by spontaneous or stimulated emission, the system relaxes back to the ground state, emitting a photon of the same energy. The linewidth of the incoherent emission is governed by the transition coherence time T_2 . In the absence of pure dephasing, this is given by the natural linewidth $\gamma = 1/T_1$. In Chapter 6, the effect of the solid-state environment on the coherent scattering was investigated. In Chapter 7, investigations are carried out into how the photon statistics of the scattered and emitted photons are effected, after emission, by spectral filtering.

7.3.1 Experimental Method

The CW laser used for all measurements in this chapter is the Toptica DL Pro. The neutral exciton of the QD is resonantly excited with a CW laser of energy $\hbar\omega_L$, inducing a Rabi frequency of $\Omega_R = 0.5\gamma$. Ω_R is calibrated using the method described in 3.7.2. The broad $\gamma = 20 \mu\text{eV}$ of the QD allows the regime of $\Gamma < \gamma$ to be explored in the following HBT $g^{(2)}(t)$ measurements using the filters described in Table 7.1 and the method described in Section 5.2.1. Here, a CW laser is used instead of a pulsed laser and the detectors used are the superconducting nanowire single-photon detectors (SNSPDs).

7.3.2 Results and Theory

Figure 7.6(a) shows the simulated total spectrum (blue) of the QD RF emission at $\Omega_R = 0.5\gamma$, with the coherent and incoherent components modelled using Lorentzian line shapes. Under these excitation conditions the natural linewidth (green) of the QD is $20 \mu\text{eV}$ with the coherent peak (red) having a linewidth of $\sim 10 \text{ neV}$ inherited from the resonant CW excitation laser. The area of the coherent peak relative to the total emission spectrum for the TLE is given by the coherent scattering fraction \mathcal{F}_{CS} [167] calculated using Equation 7.3:

$$\mathcal{F}_{CS} = \frac{1}{1 + 2\Omega_R^2/\gamma^2}, \quad (7.3)$$

which is derived from Equations 6.2 and 6.3 using $T_2 = 2T_1$, $\Delta L_{LX} = 0$ and $\gamma = 1/T_1$. When $\Omega_R = 0.5\gamma$, Equation 7.3 gives a coherent scattering fraction (\mathcal{F}_{CS}) of $2/3$. Figure 7.6(b) shows a high resolution spectrum (triangles) of the QD measured using a scanning Fabry-Pérot interferometer, measured by Alistair Brash and John O'Hara under the same conditions as Figure 7.6(a). The grey line shows the total simulated spectrum from Figure 7.6(a), convolved with the Gaussian IRF of the Fabry-Pérot interferometer which has a FWHM of $1.5 \mu\text{eV}$.

A simulation of the normalised transmission of each of the components from the

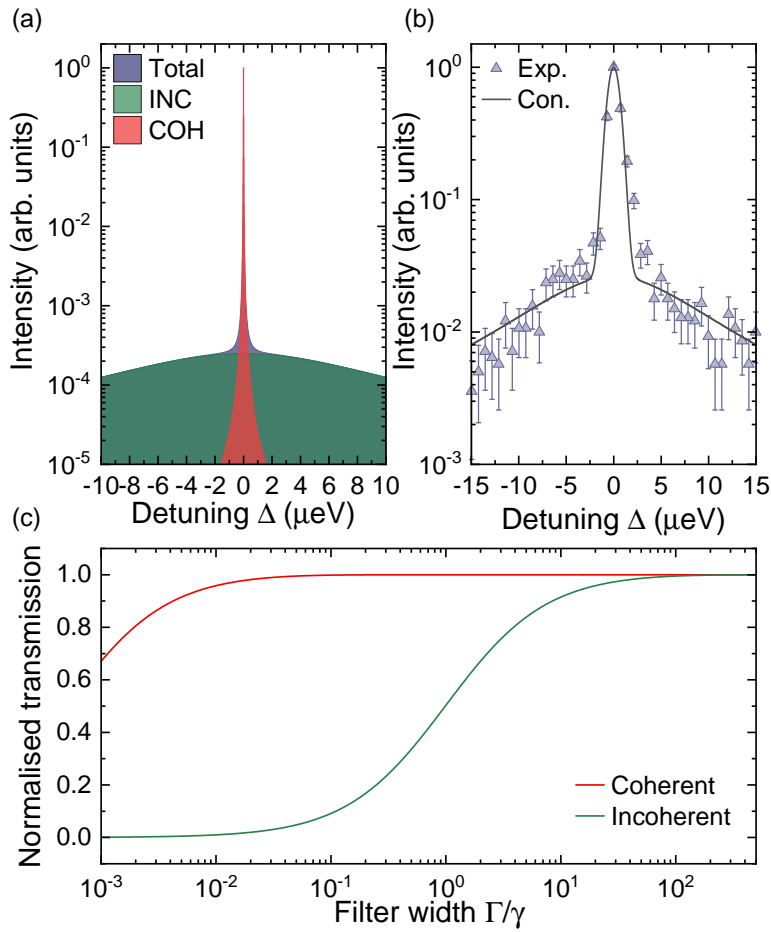


Figure 7.6: (a) Simulated emission spectrum for the QD (blue) under weak ($\Omega = 0.5\gamma$) CW excitation, showing the coherent (red) component with a ~ 10 neV linewidth inherited from the laser and the incoherent (green) component with a natural linewidth (γ) of $20 \mu\text{eV}$. (b) High resolution spectrum (triangles) of the QD, measured under the same conditions as (a) by John O'Hara and Alistair Brash, using a scanning Fabry-Pérot interferometer. The grey line shows the total theoretical spectrum from (a) after convolution with the IRF of the Fabry-Pérot interferometer. (c) Simulated transmission of the coherent (red) and incoherent (green) components through an ideal Lorentzian filter of width Γ . Reducing Γ changes the ratio of the two components.

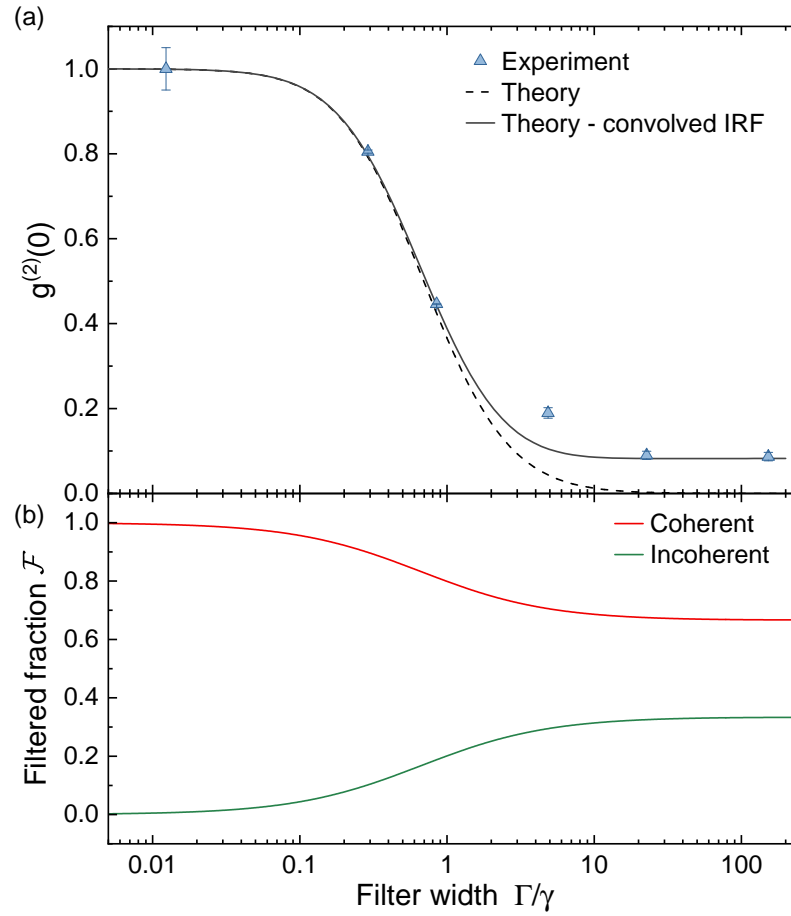


Figure 7.7: Filtered resonance fluorescence photon statistics under weak driving ($\Omega_R = 0.5\gamma$): (a) HBT $g^{(2)}(0)$ measurements of the emission through different filter bandwidths (Γ). The lines show the theory derived from sensor formalism with (solid) and without (dashed) convolution with the IRF of the nanowire detectors, 37.5 ± 0.1 ps. (b) The simulated filtered fraction (\mathcal{F}) of the emission spectrum that originates from the coherent (red) and incoherent (green) components of the QD RF emission at $\Omega_R = 0.5\gamma$.

emission through spectral filters with different Γ is shown in Figure 7.6(c). Here an ideal Lorentzian filter was applied to both the coherent and incoherent components. The proportion of each component that the emission contains after the filter is plotted against Γ/γ . As the incoherent linewidth is considerably broader (x2000) than the coherent scattering, the incoherent component starts to be removed from the RF before the coherent component when moving to narrower filter bandwidths, changing their ratio. Theory suggests that it is the change in ratio of the RF components that leads to a degradation in the antibunching, as antibunching is created by interference between the RF components [216].

Figure 7.7(a) shows the $g^{(2)}(0)$ values for filtering the RF emission with filters of various Γ . The measurements (blue triangles) show that where $\Gamma \gg \gamma$, strong antibunching ($g^{(2)}(0) < 1$) with a $g^{(2)}(0)$ value of $\sim 0.087 \pm 0.010$ is observed. As Γ approaches γ , the antibunching begins to degrade till Poissonian statistics ($g^{(2)}(0) = 1$) are reached at $\Gamma \ll \gamma$. The black line (dashed) shows the theoretical prediction using sensor theory formalised in del Valle et al. [220]. For the following theory a more detailed explanation can be found in Phillips et al. [221] and its associated supplement.

The sensor formalism for N -photon correlation functions enlarges the Hilbert space of the system to include N auxiliary two-level systems. These auxiliary two-level systems act as sensors for the emitted photons [220–222]. Using the Born-Markov-secular approach allows the the optical master equation of the QD dynamics to be derived. Enlarging the system Hilbert space and including two additional two-level systems to act as sensors for second-order correlation measurements ($g^{(2)}(t)$) gives [220–222]:

$$\dot{\rho}_S = -i[H_S, \rho_S] + \gamma \mathcal{L}_\sigma(\rho_S) + \Gamma_1 \mathcal{L}_{\theta_1}(\rho_S) + \Gamma_2 \mathcal{L}_{\theta_2}(\rho_S). \quad (7.4)$$

Here, $-i[H_S, \rho_S] + \gamma \mathcal{L}_\sigma(\rho_S)$ represents the QD system where H_S is the QD Hamiltonian and ρ_S is the QD reduced density operator, both in expanded Hilbert space. The spontaneous emission rate of the QD is given by $\gamma = 1/T_1$ and \mathcal{L}_σ is the QD emission

7 Spectral Filtering Effects on QD Resonance Fluorescence

dissipator. $\Gamma_i \mathcal{L}_{\theta_i}(\rho_S)$ represents each of the sensors. As the broadening of the filter bandwidth can be described as the broadening of the sensors, each sensor term also has a dissipator term. The filter width of each sensor is described by Γ_i .

As the experiments are performed under resonant continuous driving conditions the second-order photon correlation function can be written as [221, 222]:

$$g_{\Gamma}^{(2)}(\tau) = \lim_{\eta \rightarrow 0} \frac{\text{tr}[n_2(\tau)\theta_1(0)\rho_S(\infty)\theta_1^{\dagger}(0)]}{\langle n_1(0) \rangle_{ss} \langle n_2(0) \rangle_{ss}}. \quad (7.5)$$

Here, $\rho_S(\infty)$ is the steady-state density operator of the combined system of QD and sensors. For Figure 7.7, as Ω_R and γ are known in the experiments, Γ can be swept and $g^{(2)}(0)$ extracted, producing the dashed sensor formalism line.

Using the same formalism and including convolution with the detector IRF (solid line) agrees well with the experimental data. The SNSPDs have a Gaussian IRF with a FWHM of 37.5 ± 0.1 ps. The theory shows that without the detector IRF almost perfect antibunching ($g^{(2)}(0) = 0$) would be seen at $\Gamma \gg \gamma$.

Figure 7.7 (b) shows a simulation of what the RF comprises after a filter of width Γ is applied to the emission. The simulation models the incoherent and coherent emission as Lorentzian peaks, where the area of the coherent peak relative to the incoherent is given by Equation 7.3. The applied filter is also modelled as a Lorentzian. Unlike Figure 7.6(c), where both the incoherent and coherent components were separately normalised, here the filtered fraction (\mathcal{F}) gives the ratio of the components that remain after filtering.

Where $\Gamma \gg \gamma$, Figure 7.7(b) shows that the RF contains 2/3 coherent scattering and 1/3 incoherent emission, matching the \mathcal{F}_{CS} given by Equation 7.3. As Γ approaches γ the incoherent fraction of the RF starts to decrease as the edges of the Lorentzian start to be removed by the filter. Therefore, the relative coherent fraction of the filtered emission increases. Filtering with $\Gamma \ll \gamma$ removes most of the incoherent component,

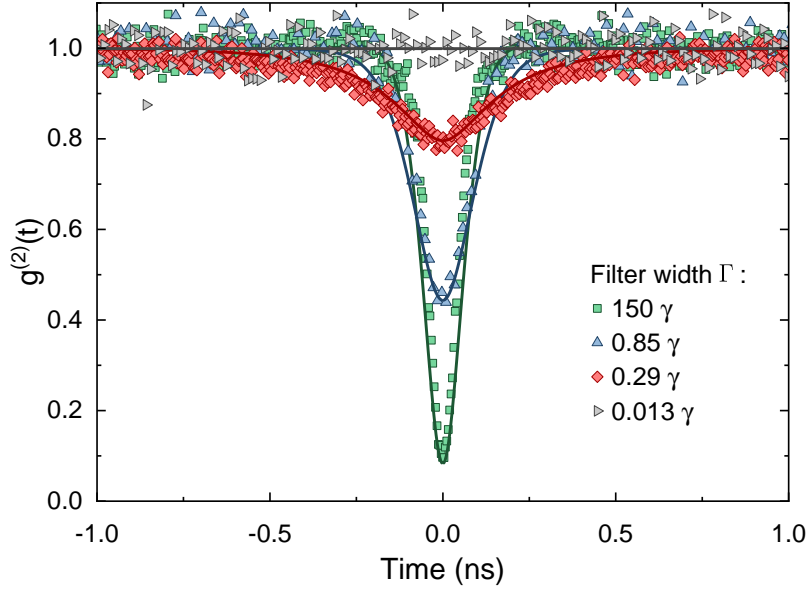


Figure 7.8: HBT $g^{(2)}(t)$ measurements of filtered RF through filters of different bandwidths (Γ). The $g^{(2)}(t)$ measurements exhibit time broadening as well as a reduction in the antibunching as Γ decreases. The solid lines show sensor theory calculations which include the detector IRF.

leaving the coherent scattering as the dominant fraction. It is important to note that the smallest filter bandwidth used ($\Gamma = 250$ neV) is much greater than the 10 neV linewidth of the coherent scattering.

Our results demonstrate that the photon statistics measured must depend on interference between the different components. A crude example for this reasoning is to consider the behaviour at $\Gamma \gg \gamma$ and assume that the incoherent component is purely antibunched and that the coherent component shows Poissonian statistics. This would give a maximum possible antibunching of 0.67 when $\Omega_R = 0.5\gamma$. In reality, theory predicts that the incoherent component is bunched [223]. In an interference-free picture, this would result in an even higher $g^{(2)}(0)$ and perfect antibunching would be impossible.

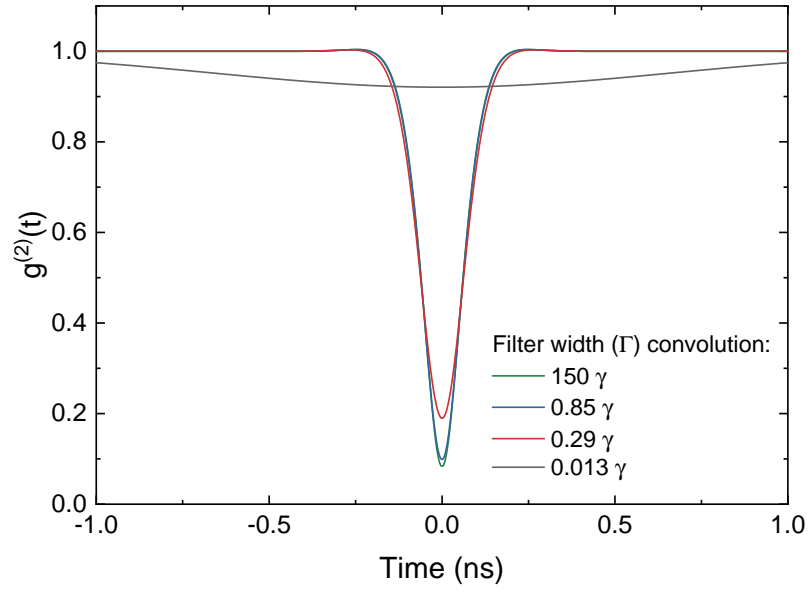


Figure 7.9: HBT simulations where the sensor theory simulation from the $\Gamma = 150\gamma$ $g^{(2)}(t)$ (Figure 7.8) is convolved with the a Gaussian with a FWHM equivalent to the Fourier transform of the different filter bandwidths.

A selection of the $g^{(2)}(t)$ measurements analysed to derive the $g^{(2)}(0)$ values shown in Figure 7.7(a) are shown in Figure 7.8. As the filter bandwidth decreases, the antibunching dip of the $g^{(2)}(t)$ exhibits time broadening. This broadening can be interpreted using the uncertainty relation [224] $\Delta E \Delta t > \hbar/2$. By using narrower filter bandwidths, the uncertainty in the energy of the photons (ΔE) is decreased. Therefore, the associated uncertainty in the photon arrival time has to increase.

However, this explanation can not be used to explain the degree of the reduction in the antibunching that is observed after filtering, for that the full sensor model is required [216]. Figure 7.9 shows theoretical $g^{(2)}(t)$ curves, calculated assuming that the filter acts only to increase the detector timing uncertainty according to the uncertainty relation $\Delta t = \hbar/(2\Delta E)$, where ΔE is the spectral filter bandwidth Γ . To simulate

7.4 Strong Driving - Mollow Triplet Regime

this, for each filter width a Gaussian with a FWHM of Δt is convolved with the $g^{(2)}(t)$ calculated using sensor theory for the broadest filter (150γ) where the filtering has negligible effect. The resulting curves show that the timing uncertainty introduced by reducing ΔE does decrease the antibunching, however the magnitude of the effect is much smaller than measured in Figure 7.8. This discrepancy, combined with the excellent agreement between the experimental data and sensor theory modelling (solid lines in Figure 7.8), demonstrates that interference between the components gives rise to the observed photon statistics and that the full sensor theory description is required to accurately model the filtered HBT [216, 221].

Passing the photons through a filter with a bandwidth Γ is equivalent to a projective measurement of a linewidth Γ . Therefore, by considering the results of Figures 7.7 and 7.8 in the regime $\Gamma < \gamma$, it can be seen that it is not possible to simultaneously measure a sub-natural linewidth and strong antibunching from a TLE, agreeing with previous theoretical predictions [216, 217].

7.4 Strong Driving - Mollow Triplet Regime

To further investigate the effect of filtering on the RF single photon statistics, measurements were also carried out in the strong driving regime. The strong driving regime is defined as $\Omega_R^2 \gg \frac{1}{T_1 T_2}$. In this regime, the excitation laser “dresses” the “bare” ground ($|0\rangle$) and excited ($|X\rangle$) states of the TLE, here the QD, resulting in the AC Stark effect transformation, as shown in Figure 7.10. The states are split by the Rabi energy, $\hbar\Omega_R$. Figure 7.10 shows that this splitting creates four possible transitions between the ground and excited states. However, as two of the transitions are degenerate (green), there are three possible transition energies, giving rise to the Mollow triplet (purple).

The spectrum shown in Figure 7.10 is a simulation for excitation of a TLE with $\Omega_R = 2\gamma$. The central peak of the Mollow triplet (green) is often termed the Rayleigh peak

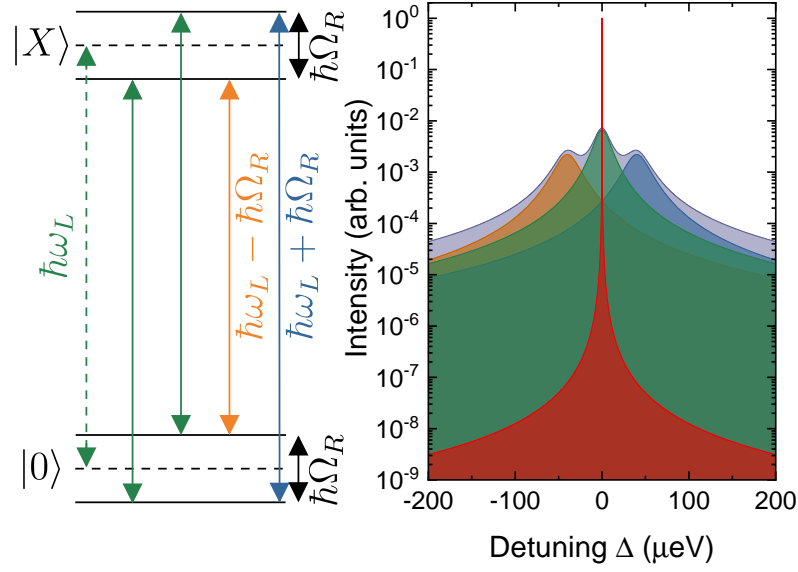


Figure 7.10: Under strong driving conditions the ground ($|0\rangle$) and excited ($|X\rangle$) states (dashed) are split (solid) by the Rabi energy ($\hbar\Omega_R$). This creates four possible transitions (orange/green/blue). However, two of the transitions are degenerate (green), leading to three possible transition energies, thus creating the Mollow Triplet (purple). The emission also contains a coherent scattering component (red). The spectrum shown here is the simulation for excitation of $\Omega_R = 2\gamma$.

and has a linewidth of γ . The two Mollow side peaks (orange/blue) have a width of $3\gamma/2$ [206, 225]. The three peaks of the Mollow triplet are all formed by incoherent emission. As well as the incoherent peaks, there is also a coherent component (red). However, as the coherent fraction is governed by Equation 7.3, the fraction of the spectrum that is coherent in the high power regime is smaller than the coherent fraction (\mathcal{F}_{CS}) in the weak driving regime.

Many frequency-resolved correlation measurements have been performed on the Mollow triplet. Performing a HBT measurement on the entire Mollow triplet emis-

7.4 Strong Driving - Mollow Triplet Regime

sion spectrum shows antibunched photon statistics. Isolating the central peak gives Poissonian statistics ($g^{(2)}(0) = 1$) [226–228], whilst isolating the side peaks shows antibunched photon statistics [227, 228]. HBT cross-correlation measurements between the central Rayleigh peak and either of the side peaks show antibunching [229] and cross-correlation between the side peaks shows bunching ($g^{(2)}(0) > 1$) [226, 228, 230]. As well as filtering the individual peaks of the Mollow triplet, measurements have also been made using filters centred half-way between the Rayleigh peak and the side peaks. These measurements have shown strong bunching originating from two-photon transitions known as “leapfrog” transitions [231, 232].

The limit of narrow spectral filtering, however, is relatively unexplored as most studies use $\Gamma > \gamma$. Peiris et al. [231] have shown that weak bunching ($g^{(2)}(0) \sim 1.2$) occurs when measuring centred on the Rayleigh peak through a filter of bandwidth $\Gamma \sim 0.25\gamma$. This section describes measurements that were performed to further investigate the regime of narrow filtering under strong driving conditions.

7.4.1 Power Dependence at $\Gamma = 0.29\gamma$

The first measurement performed to investigate the strong driving regime is a $\Gamma < \gamma$ RF power dependence (Ω_R) of the HBT $g^{(2)}(0)$. The QD exciton transition is excited resonantly with power stabilised CW driving. The excitation power is calibrated using the method in Section 3.7.2. The RF emission is filtered using the $\Gamma = 0.29\gamma$ fused silica etalon filter (Table 7.1), centred on the Rayleigh peak. This filter is used as it has $\Gamma < \gamma$. It is also the narrowest filter used in the $\Omega_R = 0.5\gamma$ HBT $g^{(2)}(0)$ Γ -dependent measurements before the return to Poissonian statistics was observed. The etalon filter also has a stable central transmission wavelength and is tuned by slight adjustments of its angle in the beam path without needing to be locked by the application of a changing stabilising voltage. The fused silica etalon filter also has a higher throughput efficiency than the scanning Fabry-Pérot interferometers.

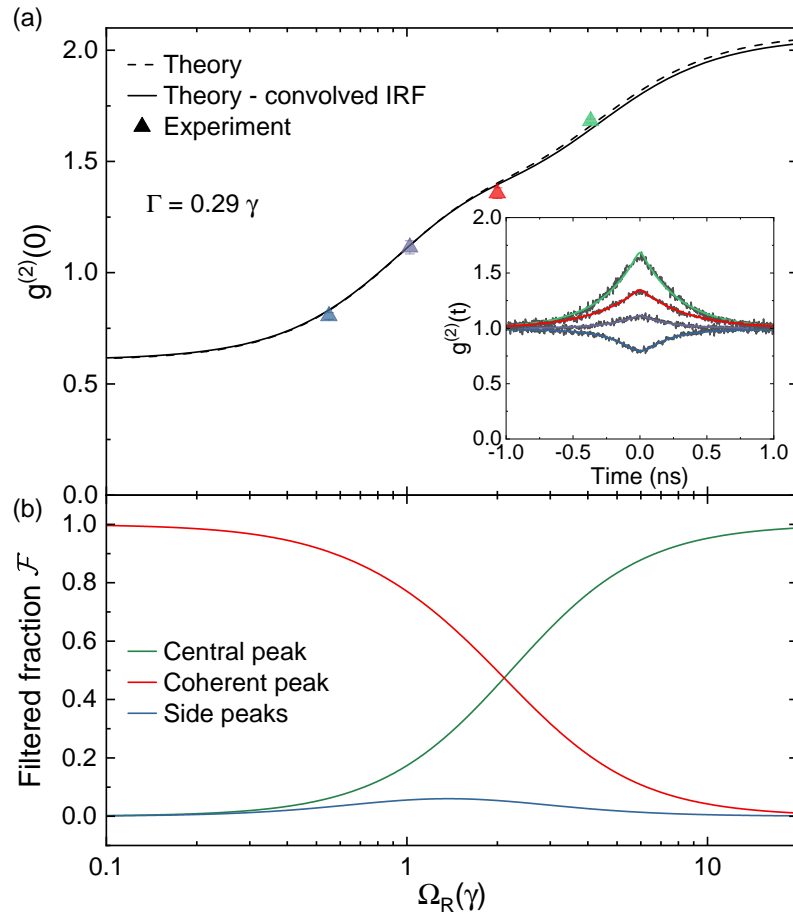


Figure 7.11: Power dependence of RF photon statistics through a $\Gamma = 0.29\gamma$ filter: (a) HBT $g^{(2)}(0)$ measurements of the filtered emission at different Ω_R . The lines show the theory derived from sensor formalism with (solid) and without (dashed) convolution with the SNSPD IRF of 37.5 ± 0.1 ps. *Inset:* The raw $g^{(2)}(t)$ measurements that are analysed for (a), showing the transition from antibunched to bunched photon statistics. The broad shape of the dip/peaks originates from the time broadening effect of using a narrow filter, demonstrated in Figure 7.8. (b) The simulated filtered fraction (\mathcal{F}) of the emission spectrum that originates from the Mollow triplet Rayleigh (green) and side peaks (blue) as well as the coherent component (red).

7.4 Strong Driving - Mollow Triplet Regime

Figure 7.11 shows the HBT $g^{(2)}(0)$ power dependence. The measurements show a transition from antibunching to bunching ($g^{(2)}(0) > 1$) as Ω_R is increased. Understanding the reasons for this transition requires understanding the filtered fractions (\mathcal{F}) that make up the RF emission after the $\Gamma = 0.29\gamma$ filter.

A simulation of \mathcal{F} is shown in Figure 7.11(b). Similar to the \mathcal{F} simulations calculated for $\Omega_R = 0.5\gamma$, an ideal Lorentzian filter was applied to the modelled RF spectrum. However, for the strong driving regime, there are also the side peaks of the Mollow triplet to consider, as well as the central Rayleigh peak and the coherent scattering. The Rayleigh peak is modelled with a linewidth of $\gamma = 20 \mu\text{eV}$, the side peaks with a linewidth of $3\gamma/2$ [206, 225] and the coherent scattering with a linewidth of 10 neV.

As can be seen in Figure 7.11(b), at low Ω_R the filtered spectrum is mostly coherent (red) due to the large coherent fraction (F_{CS}) that passes through the filter owing to a linewidth $\ll \Gamma$. Meanwhile, the majority of the incoherent emission has been removed by the filter as $\gamma > \Gamma$. As Ω_R is increased the side peaks (blue) separate from the Rayleigh peak (green) by $\hbar\Omega_R$, moving out of the bandwidth of the filter. F_{CS} also decreases in accordance with Equation 7.3. This leaves the incoherent Rayleigh peak as the dominant component of the filtered emission. It could therefore be expected that the $g^{(2)}(0)$ would return to the Poissonian photon statistics that are expected for the central peak [226–228]. However, this is not what is seen in Figure 7.11(a).

The transition from antibunching to bunching occurs due to an effect in the regime of $\Gamma < \gamma$ that is termed “indistinguishability bunching” [218]. This bunching originates from quantum fluctuations in the light field [233, 234] and is observed when filtering at less than the natural linewidth of a light source. This effect has also been observed for classical light sources, for example when filtering a laser [235]. Here, the filter has a Γ of 0.29γ and so this causes “indistinguishability bunching” of the incoherent part of the emission spectrum. The bunching component competes with the Poissonian

statistics of the coherent component. As can be seen in Figure 7.11(b), at larger values of Ω_R the incoherent component dominates as the coherent fraction decreases, leading to the domination of the indistinguishability bunching effect over the Poissonian component in the $g^{(2)}(0)$ measurements.

The dashed black line in Figure 7.11(a) shows the prediction of the theoretical model generated by our theory collaborators. As for Figure 7.7, the sensor formalism Equation 7.5 is used. However, here γ and Γ are kept constant and Ω_R is swept, before extracting $g^{(2)}(0)$. The theoretical model predicts a maximum bunching value of $g^{(2)}(0) \sim 2.21$ for these parameters. Experimentally we cannot accurately measure $\Omega_R > 4\gamma$ as the laser background is not removed as effectively by the cross-polarisation technique at high powers, reducing the signal to noise of the collected emission. Theoretically it has been shown [218] that a bunching upper limit of $g^{(2)}(0) = 3$ can be reached when using the parameters $\Omega_R = 150\gamma$ and $\Gamma = 0.005\gamma$. However, for a solid state emitter such as a QD, these parameters may not be reached due to the coherent fraction increasing again at large Ω_R . This increase is due to phonon-mediated interactions [225].

The corresponding HBT $g^{(2)}(t)$ experimental measurements (black) are shown in the inset of Figure 7.11(a). They also exhibit the time broadening that was seen in the $\Omega_R = 0.5\gamma$ measurements (Fig. 7.8) that originates from the energy-time uncertainty relation. The coloured lines show the theoretically modelled $g^{(2)}(t)$ function that corresponds to each value of Ω_R . The model uses the same parameters that give the convolved theory model in Figure 7.11(a).

7.4.2 Filter Bandwidth Dependence at $\Omega_R = 2\gamma$

To further investigate the effect of filtering in the strong driving regime, a filter bandwidth dependence of $g^{(2)}(0)$ is measured at $\Omega_R = 2\gamma$ using the filters listed in Table 7.1. A simulation of the QD RF emission spectra at $\Omega_R = 2\gamma$ is shown in Figure 7.10.

The results of the filter bandwidth dependence are shown in Figure 7.12(a). Where $\Gamma \gg \gamma$ antibunching is measured. However, the measured antibunching is degraded compared to the values measured in Figure 7.7(a) with a maximum antibunching of 0.53 ± 0.01 recorded. The reason for this can be understood by looking at the inset to Figure 7.12(a); at $\Omega_R = 2\gamma$ Rabi oscillations are observed in the $g^{(2)}(t)$ measurement. The short period of the Rabi oscillations narrows the central dip. The depth of the dip recorded is sensitive to the detector IRF, and very sharp features shorter than the IRF can be washed out, leading to a reduction in the measured antibunching.

Figure 7.12(b) shows the simulation for the filtered fractions (\mathcal{F}) of the emission against Γ/γ . At $\Gamma \gg \gamma$ the collected emission is dominated by the incoherent emission from the Rayleigh peak and side peaks. At $\Omega_R = 2\gamma$ the side peaks mostly lie within the filter bandwidth when $\Gamma \gg \gamma$. Furthermore, by using Equation 7.3, it can be calculated that the coherent fraction is $1/9$ of the total emission before filtering.

As Γ approaches γ in Figure 7.12(a), the antibunching starts to be further degraded. This contrasts with the measurements for $\Omega_R = 0.5\gamma$, where the photon statistics tended to Poissonian statistics ($g^{(2)}(0) = 1$). Here, as Γ becomes smaller than γ , the photon statistics show bunching ($g^{(2)}(0) > 1$). From Figure 7.12(b) it can be seen that, in the bunching regime, the filtered emission is dominated by the incoherent emission from the Rayleigh peak, the side peak antibunching contribution having been mostly removed by the reduction of Γ . Therefore, this bunching is explained by “indistinguishability bunching” as the bunching occurs in the region where $\Gamma < \gamma$. Here the coherent fraction is small so its Poissonian contribution to the $g^{(2)}(0)$ value is outweighed by the “indistinguishability bunching” contribution. However, at $\Gamma \ll \gamma$ the coherent scattering component starts to dominate the filtered emission again, bringing the photon statistics back to Poissonian statistics in agreement with Figure 7.7.

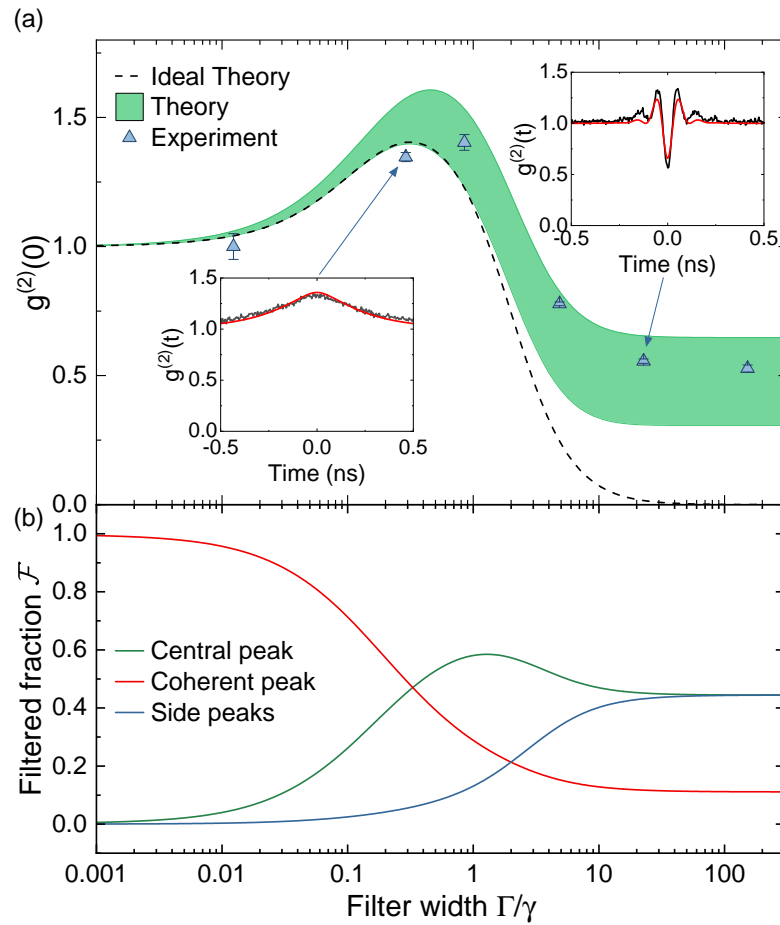


Figure 7.12: Filtered RF photon statistics under strong driving ($\Omega_R = 2\gamma$): (a) HBT $g^{(2)}(0)$ measurements of the emission through different filter bandwidths (Γ). The dashed line shows the theory derived from sensor formalism without convolution with the SNSPD IRF of 37.5 ± 0.1 ps. The green region depicts the confidence bounds defined by the theory when including the SNSPD IRF as well as a 0% (lower bound) and 20% (upper bound) contribution to the signal from the laser background. *Insets*: The $g^{(2)}(t)$ measurements (black) for the same dataset as (a), Rabi oscillations are observed for $\Gamma > \gamma$. The theoretically modelled $g^{(2)}(t)$ is shown in red. (b) The simulated filtered fraction (\mathcal{F}) of the emission spectrum that originates from the coherent (red) and incoherent central Rayleigh peak (green) as well as the Mollow side peaks (blue) components.

If a filter with a bandwidth smaller than the laser linewidth had been used then ultimately a recurrence of the “indistinguishability bunching” would be expected. The need for very narrow filtering comparable to the coherent peak linewidth ($\sim 0.005\gamma$) is why indistinguishability bunching was not observed in the Heitler regime ($\Omega_R = 0.5\gamma$) measurements. There the coherent scattering was the dominant part of the filtered emission and the filters used were much broader than its linewidth.

The theoretical model (green area) in Figure 7.12(a) reproduces the behaviour measured. Here, the model (Equation 7.5, γ and Ω_R are kept constant as Γ is swept) incorporates both the SNSPD IRF along with a lower and upper bound that corresponds to an uncertainty bound between 0% and 20% laser background contribution to the collected signal. The ideal theory line (dashed) is modelled with neither of these parameters and shows how perfect antibunching at $\Gamma \gg \gamma$ is expected if the Rabi oscillations of the $g^{(2)}(t)$ measurements could be fully resolved and not removed by the detector IRF. Figure 7.12(a) also shows that including a 20% Poissonian background contribution to the model increases the maximum bunching theoretically achievable, indicating that this extra contribution to the filtered RF has non-trivial effects.

7.5 Conclusion

In this chapter we have looked at the effect that spectral filtering has on the photon statistics measured from the RF emission of a TLE. To investigate this, filter bandwidth dependant HBT $g^{(2)}(0)$ measurements were made in both the low excitation power (RRS/Heitler) and high excitation power (Mollow) regimes. The antibunching that occurs in these regimes originates from interference between the different components of the unfiltered RF spectrum which have their own photon statistics in isolation.

In the Heitler regime, using an excitation power of $\Omega_R = 0.5\gamma$, the coherent fraction

7 Spectral Filtering Effects on QD Resonance Fluorescence

(\mathcal{F}_{CS}) of the neutral exciton emission is $2/3$. At this power a transition is seen from antibunching, where $g^{(2)}(0)$ is $\sim 0.087 \pm 0.010$ at $\Gamma = 150\gamma$, to Poissonian photon statistics ($g^{(2)}(0) = 1$) when the filter bandwidth becomes narrower than the incoherent natural linewidth (γ) of the QD. This occurs as filtering below γ alters the ratio of the coherent and incoherent components of the RF emission, removing the majority of the incoherent component and leaving the coherent component to dominate the filtered emission. As well as measuring a degradation in the antibunching, a time broadening in the measured $g^{(2)}(t)$ is also observed when measuring at narrower filter widths. As passing the photons through a filter with a narrow bandwidth is the equivalent of measuring a narrow linewidth it can, therefore, be seen that it is not possible to simultaneously measure a sub-natural linewidth and strong antibunching from a TLE. Both of these effects have been modelled using sensor formalism [216] by our theory collaborators, where they have expanded the theory to include the IRF of the detectors [221], showing excellent agreement with the measured results.

A power dependence of the RF photon statistics through a $\Gamma = 0.29\gamma$ filter was also measured. As $\Gamma < \gamma$ the majority of the incoherent emission has been removed by the filter, therefore the low power measurement ($\Omega_R = 0.5\gamma$) shows a small amount of antibunching where $g^{(2)}(0) = 0.087 \pm 0.010$. However, as Ω_R is increased the coherent fraction decreases, leaving the filtered incoherent fraction as the dominant component of the RF. This leads to bunching being observed, with a $g^{(2)}(0)$ of 1.682 ± 0.009 when $\Omega_R = 4.01\gamma$. The bunching occurs due to “indistinguishability bunching” caused by filtering below the linewidth of the dominant component of the emission, in this case the incoherent component. Again, the expanded sensor theory model fits the data well.

A filter bandwidth dependence of the RF photon statistics was also measured in the Mollow triplet regime where $\Omega_R = 2\gamma$. In the Mollow regime, bunching was also observed where $\Gamma < \gamma$ as the incoherent component dominates the filtered spectra at

high power, leading to “indistinguishability bunching”. Here, the maximum bunching observed is 1.40 ± 0.03 at $\Gamma = 0.85\gamma$. As Γ is reduced further, Poissonian statistics are restored when $\Gamma \ll \gamma$ as the coherent component again dominates the filtered spectra, due to the majority of the incoherent component being removed by the narrow filter bandwidth. The theoretical model reproduced the behaviour seen in the measurements. Here, the model included the detector IRF along with an upper and lower bound that corresponded to a 0% and 20% contribution from the laser background to the collected signal.

The dependence of the photon statistics on the filter bandwidth emphasises the need for care when using filters to improve the properties of TLEs. However, it also shows that filtering could be used as a method to modify photon statistics.

8 Summary and Future Work

8.1 Summary

In this thesis the properties of a III-V semiconductor QD in a high Purcell factor H1 PhCC have been investigated. In this chapter the experiments performed, and conclusions drawn, will be summarised.

Chapter 2 provides an introduction to the concepts used throughout this thesis including the growth and properties of self-assembled quantum dots (SAQDs) and the effect of cavities of QD emission.

Chapter 3 describes the basic experimental methods used throughout the experimental chapters. This includes a description of the Resonance Fluorescence (RF) set-up, the lasers and detection methods used

Chapter 4 describes the fabrication process for the sample along with a summary of the characterisation measurements that were performed. These include the measurement of the T_1 time of the neutral exciton emission, through use of a DPRF measurement scheme, and so by extension the Purcell factor of the cavity-QD system.

8.1.1 Cavity Coupled QD as a Single-Photon Source

In Chapter 5 the single-photon properties of the cavity-QD system were investigated using pulsed RF. Using Hanbury Brown and Twiss (HBT) second-order correlation

measurements the single-photon properties are shown to be improved when the length of the excitation pulse is decreased to $\ll T_1$. As well as measuring the antibunching properties of the QD, Hong-Ou-Mandel (HOM) measurements were performed, under the same conditions, to measure the single-photon indistinguishability. Further investigations into the effect of the excitation pulse separation on the single-photon indistinguishability were also carried out, showing that the QD-cavity structure's high Purcell factor would potentially allow for the production of over 20 or so near-identical photons if the repetition rate of the pump laser was increased. The indistinguishability begins to decrease at a time on the order of the expected spectral wandering, an effect that is again reduced by the high Purcell factor of the H1 cavity.

8.1.2 Phonon Effects on QD Emission

In Chapter 6 the effect of the QD's environment on its coherently scattered emission was investigated to provide insight into the phonon interactions present and how this behaviour deviates from the two-level "atomic picture". First-order correlation measurements were used to measure the phonon relaxation timescale and were well fitted using the polaron master equation. Through spectroscopic measurements, the proportion of emission into the phonon sideband (PSB) was found to be insensitive to CW excitation power, as is predicted by the polaron model. Investigation into the effect of laser detuning on the coherent scattering through the use of first-order correlation measurements also showed a non-monotonic relationship which deviates from two-level "atomic picture" behaviour.

8.1.3 Spectral Filtering Effects on QD Resonance Fluorescence

In Chapter 7 the effect of filtering RF emission from the QD on the measured photon statistics was investigated. In the weak (RRS/Heitler) CW excitation regime, filtering the RF emission below the natural linewidth (γ) of the QD showed a reduction in the measured antibunching, tending to coherent Poissonian statistics where the

filter bandwidth was $\ll \gamma$. This verifies that strong antibunching and a sub-natural linewidth cannot be simultaneously observed. The strong (Mollow) CW excitation regime was also investigated. Here, a transition from antibunched to bunched statistics was observed as the filter bandwidth was reduced below γ . This “indistinguishability bunching” occurs when filtering below the linewidth of the dominant component of the RF, in this case filtering below the linewidth of the incoherent central peak of the Mollow triplet. When filtering at $\ll \gamma$ a transition from bunched to Poissonian statistics is seen as under these conditions coherent scattering becomes the dominant component of the emission but the filter bandwidth remains much broader than the coherent scattering linewidth.

8.2 Future Work for the QD in a H1 Cavity

8.2.1 Improving the Excitation Pulse Shaping

As was demonstrated in Section 5.3.2, the antibunching properties of the QD as a single photon source can be improved by decreasing the excitation laser pulse length. This is due to a lower re-excitation probability when the pulse length is $\ll T_1$ [139]. Experimentally, the reduction in the length of the excitation pulses at the sample is limited by dispersion. One of the main sources of dispersion originates from the single-mode fibres that are used between the 4f pulse shapers and the cryostat.

Dispersion is where the individual optical pulses spread out temporally in a medium (e.g. silicon for single-mode fibres). This occurs as the refractive index (n) of a medium is wavelength dependent and therefore the speed of light in the medium is also wavelength dependent [236]. The dispersion can be characterised as normal or anomalous dispersion. Normal dispersion leads to a lower group velocity for the high frequency components of a pulse and is termed positive chirp. Anomalous dispersion leads to negative chirp where the low frequency components have a lower group velocity. To enable short pulses at the sample the fibre dispersion needs to be

8 Summary and Future Work

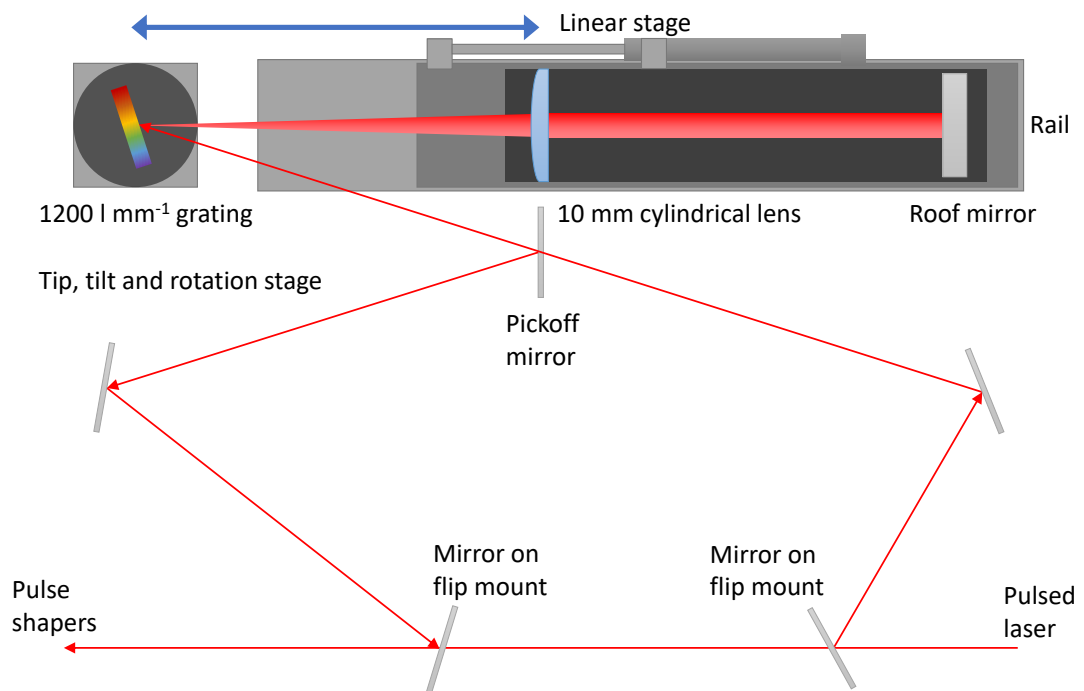


Figure 8.1: Schematic of the Martinez pulse compressor used to correct for dispersion in single-mode optical fibres. By adjusting the position of the linear stage either positive or negative chirp can be corrected for.

compensated for, this is achieved by pre-chirping the pulses in the opposite direction before the fibre.

To correct for the fibre dispersion a Martinez pulse compressor [237] is built between the Mira pulsed laser and the 4f pulse shapers. A schematic of the Martinez pulse compressor is shown in Figure 8.1. Mirrors mounted on flip mounts are used to divert the pulsed laser through the pulse compressor, the flip mounts allow the beam to bypass the pulse compressor if it is not required. The Martinez pulse compressor has a similar geometry to a folded 4f pulse shaper. However, rather than using a slit and tilted mirror in the Fourier plane of the shaper, a roof mirror is used at the focal point (f) of the cylindrical lens to achieve vertical displacement between the input

8.2 Future Work for the QD in a H1 Cavity

and output beams. The distance between the lens and the roof mirror is fixed at f . By mounting them on a linear stage, the distance between the fixed optics and the 1200 mm^{-1} diffraction grating can be adjusted. Changing this distance can give the pulses positive or negative chirp by adjusting the path length of the different spectral components.

To monitor the effect of the Martinez pulse compressor on the pulse dispersion, an APE Mini autocorrelator is used after the pulsed laser has been coupled into single-mode fibre. The fibre used between the fibre coupler and the autocorrelator has the same length as the fibre between the fibre coupler and the cryostat-mounted breadboard. The Martinez pulse compressor allows correction of both positive or negative chirp and can reduce the length by an order of magnitude to $\sim 200 \text{ fs}$.

To further increase the control over the excitation pulse length, improvements have also been made to the $4f$ pulse shapers. The plano-convex lenses have been replaced by cylindrical lenses to reduce spherical aberration. Also, to improve the resolution of the pulse shapers, an additional 3:1 telescope has been incorporated before the first 1200 l mm^{-1} diffraction grating to increase the fill of the laser spot on the grating. This magnification is reversed after the second grating by a second 3:1 telescope, before the pulsed laser is coupled into the single-mode fibre. The increased resolution allows for the generation of longer pulses as filling the grating allows for a larger spectral splitting and so spectrally narrower pulses can be achieved. The telescopes produce a factor of 3 improvement to the pulse shaper resolution.

Finer excitation pulse control can be used for further investigation of how the antibunching properties of the single-photon source are modified with pulse length.

8.2.2 Improving the H1 PhCC Sample

The QD in the H1 PhCC used throughout this thesis experiences a Purcell factor (F_p) of ~ 43 . This leads to a short radiative lifetime of ~ 21.7 ps. A short radiative lifetime is advantageous for single-photon sources in photonic crystal structures as it reduces the effect of charge fluctuations from nearby etched surfaces and, in doing so, can reduce the spectral wandering of QD emission, increasing the indistinguishability of the single photons [34, 106, 238]. Here, the high F_p is generated as the H1 PhCC has a high cavity Q -factor and a low mode volume (Section 4.2). The short radiative lifetime also leads to the exciton's broad $20 \mu\text{eV}$ natural linewidth, which made filtering below the natural linewidth for the HBT measurements of Chapter 7 possible [221]. As well as generating a high F_p , a high Q cavity can also be used as a filter to reduce the QD phonon sideband emission (PSB) [95, 100, 200]. However, a very high Q -factor can move the cavity to the strong-coupling regime [95].

In Section 2.5.4 methods to increase the Q -factors of H1 PhCCs were discussed. These included changing the radius and position of the etched holes closest to the cavity. Improvements to the Q -factor of H1 PhCCs have also been shown in systems where the lattice of the photonic crystal is stretched [239]. Theoretical Q -factors of $\sim 1 \times 10^6$ have been shown for Silicon H1 PhCCs, where the inner three rings of etched holes closest to the cavity have a modified position [240]. These all suggest that much higher Purcell factors than that achieved with the sample in this thesis are possible. This improvement could be achieved through further simulation of the H1 PhCC and also through improved fabrication methods, reducing the decrease in the Q -factor that occurs due to the high scattering loss rates observed in the fabricated samples [121].

As the F_p also depends on the spatial overlap between the emitter and the cavity mode (Section 2.5.2), the position of the QDs within the cavity is also important to achieve a high F_p . This can be achieved through QD registration which will be discussed in Section 8.3.3.

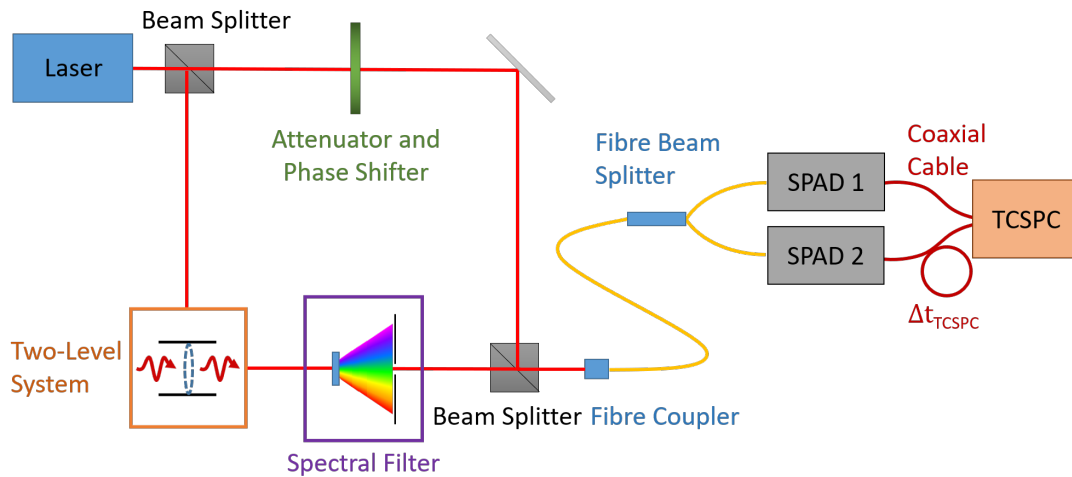


Figure 8.2: Theoretical homodyne scheme allows simultaneous measurement of a sub-natural linewidth and strong antibunching. A π -phase shift is introduced to the driving laser which is then recombined with the RF from a two-level system at a beam splitter. The modified laser destructively interferes with the coherent part of the RF, returning its relative coherent and incoherent fractions to their pre-filtering values. This allows strong antibunching to be measured using a HBT set-up. Figure adapted from López Carreño et al. [216] to include the measurement scheme used in Chapter 7.

8.2.3 Homodyne Scheme for Measuring Antibunching and a Sub-natural Linewidth

As was shown in Chapter 7, a sub-natural linewidth and strong antibunching cannot be measured simultaneously. However, a homodyne scheme where the RF output of a two-level system is combined with a coherent beam, has been shown theoretically by López Carreño et al. [216] to lead to a recovery of the strong antibunching, while measuring a sub-natural linewidth. Antibunching occurs from interference between the coherent and incoherent parts of the RF emission. The coherent part of the emission inherits a long coherence time from the excitation laser and so has a narrow linewidth when compared to the incoherent emission's natural linewidth. Filtering

8 Summary and Future Work

below the natural linewidth of the RF removes part of the broad incoherent emission, leading to a reduction in the observed antibunching [216, 218, 221, 241].

The homodyne scheme proposed by López Carreño et al. [216] introduces an external π -phase shifted coherent laser beam to destructively interfere with the coherent part of the RF and, in doing so, reduce the coherent fraction. This returns the coherent and incoherent fractions of the RF to their relative values before the filter modification. Therefore, a return of strong antibunching can theoretically be observed. Figure 8.2 shows the measurement scheme from López Carreño et al., modified to include the filtering system used in Chapter 7. By diverting part of the laser that is initially used to excite the two-level system ensures that the homodyning laser has the same wavelength and coherence time as the driving laser and makes it immune to slow fluctuations.

8.3 Future Work - Related Areas

The following section describes some possible future directions for QD-cavity coupled systems with high Purcell factors and ways to optimise the fabrication of such systems.

8.3.1 Telecom C-Band QDs

As was described in Section 1.1, quantum states of light can be used for secure quantum communication [1, 31]. However, many QD sources of quantum light states emit in the visible and near infra-red range and the current optical-telecom fibre infrastructure has a loss of >1 dB/km at 900 nm [242]. Therefore, for low-error long-distance fibre-based quantum communication, single-photon sources that emit in the low-loss fibre telecom C-band (~ 1550 nm) are required, where the loss is ~ 0.2 dB/km [243, 244]. Sources that emit at 1550 nm can also generate photons for use in free-space satellite communication during daylight, by exploiting the reduction in the

solar radiation spectrum and an increase in atmospheric transmission at this wavelength [245].

Progress has been made on growing QDs that emit in the telecom C-band. Two of the material systems used to emit in the C-band are InAs/InP and InAs/InGaAs/GaAs. Both systems have shown the emission of single-photons [246–248] and long coherence times [242, 249]. Combining resonance fluorescence excitation [249], along with photonic crystal cavity structures [250], has the potential to create Purcell enhanced single-photon sources, like the cavity-QD system described in this thesis, at telecom wavelengths.

8.3.2 QD Spin in a Cavity for Photonic Cluster State Generation

As sources of single-photons, QDs have the potential to be used in the generation of photonic cluster states for linear optical quantum computing. As is described in Ref. [30], one dimensional photonic cluster states can be generated through repeated pulsed resonant excitation of a QD whose spin is precessing in an external magnetic field. This scheme encodes the photons in terms of polarisation. Further work has been carried out into encoding the photons into time-bins instead of polarisation. Here, a QD with a trapped charge carrier is placed in a Voigt magnetic field [251, 252]. Both of these schemes benefit from the use of cavities.

When mapping the spin of the electron onto the polarisation of a photon, to produce a cluster state with a high fidelity T_1 needs to be much shorter than the spin precession time, otherwise there is a large resulting uncertainty in the polarisation of the emitted photon. However, for any realistic emitter, T_2 is finite and therefore it is advantageous to increase the speed of the spin precession, so that many photons can be emitted within the spin coherence time, enabling the creation of large cluster states. To increase the speed of the precession, while maintaining the fidelity, requires a reduction of T_1 . This can be achieved through the use of a cavity with a high Purcell

8 Summary and Future Work

factor. Reducing the T_1 , through a strong Purcell enhancement, allows the production of cluster states with more photons from a spin with the same coherence time.

The spin to time-bin scheme operates in a Voigt magnetic field, where the excitation scheme produces a double lambda system. Therefore, a cavity with a strong Purcell effect can be used to enhance the desired transition and suppress the undesired spin-flip of the diagonal transitions. A large Purcell factor also decreases T_1 , enabling a much faster readout.

8.3.3 QD Registration

To achieve all of the above quantum-optics goals it would be beneficial to have finer control over the QD-cavity properties measured. One way in which this could be improved would be to fabricate nano-photonic structures around optimally positioned QDs. The positioning of QDs can be achieved through site-controlled QD growth, as briefly discussed in Section 2.2.2. Another possible solution is the registration of QDs before the photonic structures are fabricated. Two methods for this are briefly discussed here.

One method to register the position and emission wavelength of QDs involves using scanning microscopic photoluminescence (μ -PL) spectroscopy [56]. Gold open-box markers are patterned onto the sample surface with the boxes having an area of $\sim 20 \mu\text{m}^2$. A μ -PL set-up is used to excite the sample using an above-band laser and to collect the sample emission. By mounting either the sample or the objective lens of the μ -PL set-up on closed-loop piezo stages, the excitation and collection can be scanned in a grid pattern across the sample. The collected emission is split onto two avalanche photodiodes (APDs), each with a different narrow-band filter. One filter allows emission of the ideal QD wavelength to be detected. The second allows monitoring of the emission from the semiconductor bandgap. The emission from the bandgap is reduced above the markers due to the high reflectivity of the gold. By

mapping the peaks in the QD emission relative to the marker positions a map of the sample can be created. For more detailed spectral information about the QDs, a spectrometer can be used instead of APDs. This method can map the position of the QDs with a < 10 nm accuracy [56].

A second method for QD registration is to use an imaging set-up [57–59]. Similarly to the scanning μ -PL spectroscopy method, markers are patterned onto the surface of the sample. However, for imaging QD registration the markers can define a larger registration area, e.g. the 10 mm^2 area used in Ref. [58]. The imaging set-up uses two-colour LED illumination of the sample. A CCD camera detects the emission and reflected light from the sample. One LED wavelength is above the bandgap of the semiconductor and so excites the QDs. The second LED has a wavelength close to the expected QD emission wavelength and is used to dimly illuminate the surface of the sample. Using low levels of illumination allows the reflective markers to be seen on the camera without saturating the dimmer QD signal. Image analysis is then used to map the centre of each QD with respect to the markers. The precision of the QD mapping relates to the pixel size of the camera CCD and the size of the projected image of the sample on the camera. Optimising the magnification so that the emission from each QD is detected on multiple pixels has been shown to give position uncertainties for the QDs of ~ 5 nm [59]. Incorporating an excitation laser in to the imaging set-up along with a beam splitter to divert part of the collected emission to a spectrometer allows μ -PL spectra of individual QDs to be taken after their position has been mapped.

Improving the QD-cavity coupling through optimally positioning the nano-photon structures around the QDs can increase the Purcell factor of the QD. As well as increasing the possible emission rate, a high Purcell factor would also broaden the natural linewidth of the emission and so would allow a greater range of spectral filter bandwidths to be investigated when measuring the effects of spectral filtering on the QD photon statistics.

Acronyms

AC	Alternating Current
AlAs	Aluminium Arsenide
AlGaAs	Aluminium Gallium Arsenide
APD	Avalanche Photodiode
CCD	Charge-Coupled Device
CuCl	Copper Chloride
CW	Continuous Wave
DC	Direct Current
DBR	Distributed Bragg Reflector
DPRF	Double π -Pulse Resonance Fluorescence
EBL	Electron Beam Lithography
EID	Excitation-Induced Dephasing
FPI	Fabry-Pérot Interferometer
FSS	Fine-Structure Splitting
FDTD	Finite-Difference-Time-Domain
FSR	Free Spectral Range
FWHM	Full-Width Half Maximum
Ga	Gallium
GaAs	Gallium Arsenide
HBT	Hanbury Brown and Twiss
He	Helium
HOM	Hong-Ou-Mandel

Acronyms

HF	Hydrofluoric Acid
In	Indium
InAs	Indium Arsenide
InGaAs	Indium Gallium Arsenide
InP	Indium Phosphide
ICP	Inductively Coupled Plasma
IRF	Instrument Response Function
LA	Longitudinal Acoustic Phonons
LO	Longitudinal Optical Phonons
MOCVD	Metal-organic Chemical Vapour Deposition
MOVPE	Metal-organic Vapour-phase Epitaxy
μ -PL	Microscopic Photoluminescence
MBE	Molecular Beam Epitaxy
ME	Master Equation
ND	Neutral Density
PhC	Photonic Crystal
PhCC	Photonic Crystal Cavity
PSB	Phonon Sideband
QCSE	Quantum-Confined Stark Effect
QD	Quantum Dot
RF	Resonance Fluorescence
SAQD	Self-assembled Quantum Dot
SEM	Scanning Electron Microscope
SK	Stranski-Krastanow
SNSPD	Superconducting Nanowire Single-Photon Detectors
SPAD	Single-Photon Avalanche Diode
SPS	Single Photon Source
TA	Transverse Acoustic Phonons
TCSPC	Time-correlated Single Photon Counting Module

Ti:S	Ti:Sapphire
TLE	Two-level Emitter
VOA	Variable Optical Attenuator
ZPL	Zero Phonon Line

Bibliography

- [1] N. Gisin, G. Ribordy, W. Tittel, and H. Zbinden, "Quantum cryptography," *Reviews of Modern Physics* **74**, 145–195 (2002).
- [2] Z.-S. Yuan, X.-H. Bao, C.-Y. Lu, J. Zhang, C.-Z. Peng, and J.-W. Pan, "Entangled photons and quantum communication," *Physics Reports* **497**, 1 – 40 (2010).
- [3] R. P. Feynman, "Simulating physics with computers," *International Journal of Theoretical Physics* **21**, 467–488 (1982).
- [4] E. Knill, R. Laflamme, and G. J. Milburn, "A scheme for efficient quantum computation with linear optics," *Nature* **409**, 46–52 (2001).
- [5] P. Kok, W. J. Munro, K. Nemoto, T. C. Ralph, J. P. Dowling, and G. J. Milburn, "Linear optical quantum computing with photonic qubits," *Reviews of Modern Physics* **79**, 135–174 (2007).
- [6] J. P. Dowling, "Quantum optical metrology – the lowdown on high-N00N states," *Contemporary Physics* **49**, 125–143 (2008).
- [7] V. Giovannetti, S. Lloyd, and L. Maccone, "Advances in quantum metrology," *Nature Photonics* **5**, 222–229 (2011).
- [8] J. L. Park, "The concept of transition in quantum mechanics," *Foundations of Physics* **1**, 23–33 (1970).
- [9] P. W. Shor, "Polynomial-Time Algorithms for Prime Factorization and Discrete Logarithms on a Quantum Computer," *SIAM Review* **41**, 303–332 (1999).

Bibliography

- [10] L. K. Grover, "A fast quantum mechanical algorithm for database search," in "28th Annual ACM Symposium on the Theory of Computing (STOC)," (1996), pp. 212–219.
- [11] D. W. Berry, G. Ahokas, R. Cleve, and B. C. Sanders, "Efficient quantum algorithms for simulating sparse hamiltonians," *Communications in Mathematical Physics* **270**, 359–371 (2006).
- [12] B. P. Lanyon, C. Hempel, D. Nigg, M. Müller, R. Gerritsma, F. Zähringer, P. Schindler, J. T. Barreiro, M. Rambach, G. Kirchmair, M. Hennrich, P. Zoller, R. Blatt, and C. F. Roos, "Universal digital quantum simulation with trapped ions," *Science* **334**, 57–61 (2011).
- [13] D. P. DiVincenzo, "The Physical Implementation of Quantum Computation," *Fortschritte der Physik* **48**, 771–783 (2000).
- [14] J. L. O'Brien, "Optical Quantum Computing," *Science* **318**, 1567–1570 (2007).
- [15] C. Vitelli, N. Spagnolo, L. Toffoli, F. Sciarrino, and F. De Martini, "Enhanced resolution of lossy interferometry by coherent amplification of single photons," *Physical Review Letters* **105**, 113602 (2010).
- [16] M. Müller, H. Vural, C. Schneider, A. Rastelli, O. G. Schmidt, S. Höfling, and P. Michler, "Quantum-dot single-photon sources for entanglement enhanced interferometry," *Physical Review Letters* **118**, 257402 (2017).
- [17] Y. Arakawa and M. J. Holmes, "Progress in quantum-dot single photon sources for quantum information technologies: A broad spectrum overview," *Applied Physics Reviews* **7**, 021309 (2020).
- [18] H. Wang, Y.-M. He, T.-H. Chung, H. Hu, Y. Yu, S. Chen, X. Ding, M.-C. Chen, J. Qin, X. Yang, R.-Z. Liu, Z.-C. Duan, J.-P. Li, S. Gerhardt, K. Winkler, J. Jurkat, L.-J. Wang, N. Gregersen, Y.-H. Huo, Q. Dai, S. Yu, S. Höfling, C.-Y. Lu, and

- J.-W. Pan, "Towards optimal single-photon sources from polarized microcavities," *Nature Photonics* **13**, 770–775 (2019).
- [19] M. E. Reimer and C. Cher, "The quest for a perfect single-photon source," *Nature Photonics* **13**, 734–736 (2019).
- [20] M. Arcari, I. Söllner, A. Javadi, S. Lindskov Hansen, S. Mahmoodian, J. Liu, H. Thyrrestrup, E. H. Lee, J. D. Song, S. Stobbe, and P. Lodahl, "Near-Unity Coupling Efficiency of a Quantum Emitter to a Photonic Crystal Waveguide," *Physical Review Letters* **113**, 093603 (2014).
- [21] U. Rengstl, M. Schwartz, T. Herzog, F. Hargart, M. Paul, S. L. Portalupi, M. Jetter, and P. Michler, "On-chip beamsplitter operation on single photons from quasi-resonantly excited quantum dots embedded in gas rib waveguides," *Applied Physics Letters* **107**, 021101 (2015).
- [22] A. Laucht, S. Pütz, T. Günthner, N. Hauke, R. Saive, S. Frédérick, M. Bichler, M.-C. Amann, A. W. Holleitner, M. Kaniber, and J. J. Finley, "A Waveguide-Coupled On-Chip Single-Photon Source," *Physical Review X* **2**, 011014 (2012).
- [23] T. Lund-Hansen, S. Stobbe, B. Julsgaard, H. Thyrrestrup, T. Süner, M. Kamp, A. Forchel, and P. Lodahl, "Experimental Realization of Highly Efficient Broadband Coupling of Single Quantum Dots to a Photonic Crystal Waveguide," *Physical Review Letters* **101**, 113903 (2008).
- [24] M. N. Makhonin, J. E. Dixon, R. J. Coles, B. Royall, I. J. Luxmoore, E. Clarke, M. Hugues, M. S. Skolnick, and A. M. Fox, "Waveguide Coupled Resonance Fluorescence from On-Chip Quantum Emitter," *Nano Letters* **14**, 6997–7002 (2014).
- [25] S. Tanzilli, A. Martin, F. Kaiser, M. De Micheli, O. Alibart, and D. Ostrowsky, "On the genesis and evolution of Integrated Quantum Optics," *Laser & Photonics Reviews* **6**, 115–143 (2012).

Bibliography

- [26] J. L. O'Brien, A. Furusawa, and J. Vučković, "Photonic quantum technologies," *Nature Photonics* **3**, 687–695 (2009).
- [27] H. Wang, Y. He, Y.-H. Li, Z.-E. Su, B. Li, H.-L. Huang, X. Ding, M.-C. Chen, C. Liu, J. Qin, J.-P. Li, Y.-M. He, C. Schneider, M. Kamp, C.-Z. Peng, S. Höfling, C.-Y. Lu, and J.-W. Pan, "High-efficiency multiphoton boson sampling," *Nature Photonics* **11**, 361–365 (2017).
- [28] J. C. Loredó, M. A. Broome, P. Hilaire, O. Gazzano, I. Sagnes, A. Lemaitre, M. P. Almeida, P. Senellart, and A. G. White, "Boson Sampling with Single-Photon Fock States from a Bright Solid-State Source," *Physical Review Letters* **118**, 130503 (2017).
- [29] S. Fan, S. E. Kocabaş, and J.-T. Shen, "Input-output formalism for few-photon transport in one-dimensional nanophotonic waveguides coupled to a qubit," *Physical Review A* **82**, 063821 (2010).
- [30] N. H. Lindner and T. Rudolph, "Proposal for Pulsed On-Demand Sources of Photonic Cluster State Strings," *Physical Review Letters* **103**, 113602 (2009).
- [31] H. J. Kimble, "The quantum internet," *Nature* **453**, 1023–1030 (2008).
- [32] Y. Yu, F. Ma, X.-Y. Luo, B. Jing, P.-F. Sun, R.-Z. Fang, C.-W. Yang, H. Liu, M.-Y. Zheng, X.-P. Xie, W.-J. Zhang, L.-X. You, Z. Wang, T.-Y. Chen, Q. Zhang, X.-H. Bao, and J.-W. Pan, "Entanglement of two quantum memories via fibres over dozens of kilometres," *Nature* **578**, 240–245 (2020).
- [33] A. J. Shields, "Semiconductor quantum light sources," *Nature Photonics* **1**, 215–223 (2007).
- [34] C. P. Dietrich, A. Fiore, M. G. Thompson, M. Kamp and S. Höfling, "GaAs integrated quantum photonics: Towards compact and multi-functional quantum photonic integrated circuits," *Laser & Photonics Reviews* **10**, 870–894 (2016).

- [35] O. Gazzano, S. M. de Vasconcellos, C. Arnold, A. Nowak, E. Galopin, I. Sagnes, L. Lanco, A. Lemaître, and P. Senellart, "Bright solid-state sources of indistinguishable single photons," *Nature Communications* **4** (2013).
- [36] A. Dousse, J. Suffczyński, A. Beveratos, O. Krebs, A. Lemaître, I. Sagnes, J. Bloch, P. Voisin, and P. Senellart, "Ultrabright source of entangled photon pairs," *Nature* **466**, 217–220 (2010).
- [37] S. Strauf, N. G. Stoltz, M. T. Rakher, L. A. Coldren, P. M. Petroff, and D. Bouwmeester, "High-frequency single-photon source with polarization control," *Nature Photonics* **1**, 704–708 (2007).
- [38] A. I. Ekimov and A. A. Onushchenko, "Quantum size effect in three-dimensional microscopic semiconductor crystals," *Journal of Experimental and Theoretical Physics Letters* **34**, 345 (1981).
- [39] R. Rossetti, S. Nakahara, and L. E. Brus, "Quantum size effects in the redox potentials, resonance Raman spectra, and electronic spectra of CdS crystallites in aqueous solution," *The Journal of Chemical Physics* **79**, 1086–1088 (1983).
- [40] N. Koguchi, S. Takahashi, and T. Chikyow, "New MBE growth method for InSb quantum well boxes," *Journal of Crystal Growth* **111**, 688 – 692 (1991).
- [41] D. J. Eaglesham and M. Cerullo, "Dislocation-free Stranski-Krastanow growth of Ge on Si(100)," *Physical Review Letters* **64**, 1943–1946 (1990).
- [42] I. N. Stranski and L. Krastanov, *Mathematische Naturwissenschaftliche Klasse* **2B 146**, 79 (1938).
- [43] C. W. Snyder, B. G. Orr, D. Kessler, and L. M. Sander, "Effect of strain on surface morphology in highly strained InGaAs films," *Physical Review Letters* **66**, 3032–3035 (1991).
- [44] D. Leonard, M. Krishnamurthy, C. M. Reeves, S. P. Denbaars, and P. M. Petroff,

Bibliography

- “Direct formation of quantum-sized dots from uniform coherent islands of InGaAs on GaAs surfaces,” *Applied Physics Letters* **63**, 3203–3205 (1993).
- [45] J. M. Moison, F. Houzay, F. Barthe, L. Leprince, E. André, and O. Vatel, “Self-organized growth of regular nanometer-scale InAs dots on GaAs,” *Applied Physics Letters* **64**, 196–198 (1994).
- [46] P. Petroff and S. DenBaars, “MBE and MOCVD growth and properties of self-assembling quantum dot arrays in III-V semiconductor structures,” *Superlattices and Microstructures* **15**, 15 (1994).
- [47] M. Fox, *Quantum Optics : an introduction* (Oxford University Press, Oxford, 2007).
- [48] P. Petroff, “Epitaxial Growth and Electronic Structure of Self-Assembled Quantum Dots,” in “Single Quantum Dots: Fundamentals, Applications and New Concepts,” , vol. 90 of *Topics in Applied Physics*, P. Michler, ed. (Springer, Berlin, 2003), pp. 1–24.
- [49] C. Matthiesen, A. N. Vamivakas, and M. Atatüre, “Subnatural Linewidth Single Photons from a Quantum Dot,” *Physical Review Letters* **108**, 093602 (2012).
- [50] O. G. Schmidt, ed., *Lateral Alignment of Epitaxial Quantum Dots*, NanoScience and Technology (Springer-Verlag, 2007).
- [51] A. Hartmann, L. Loubies, F. Reinhardt, and E. Kapon, “Self-limiting growth of quantum dot heterostructures on nonplanar {111}B substrates,” *Applied Physics Letters* **71**, 1314–1316 (1997).
- [52] A. Hartmann, Y. Ducommun, E. Kapon, U. Hohenester, and E. Molinari, “Few-Particle Effects in Semiconductor Quantum Dots: Observation of Multicharged Excitons,” *Physical Review Letters* **84**, 5648–5651 (2000).

- [53] S. Kohmoto, H. Nakamura, T. Ishikawa, and K. Asakawa, "Site-controlled self-organization of individual InAs quantum dots by scanning tunneling probe-assisted nanolithography," *Applied Physics Letters* **75**, 3488–3490 (1999).
- [54] H. Heidemeyer, C. Müller, and O. Schmidt, "Highly ordered arrays of In(Ga)As quantum dots on patterned GaAs(001) substrates," *Journal of Crystal Growth* **261**, 444 – 449 (2004).
- [55] K. D. Jöns, P. Atkinson, M. Müller, M. Heldmaier, S. M. Ulrich, O. G. Schmidt, and P. Michler, "Triggered Indistinguishable Single Photons with Narrow Line Widths from Site-Controlled Quantum Dots," *Nano Letters* **13**, 126–130 (2013).
- [56] S. M. Thon, M. T. Rakher, H. Kim, J. Gudat, W. T. M. Irvine, P. M. Petroff, and D. Bouwmeester, "Strong coupling through optical positioning of a quantum dot in a photonic crystal cavity," *Applied Physics Letters* **94**, 111115 (2009).
- [57] T. Kojima, K. Kojima, T. Asano, and S. Noda, "Accurate alignment of a photonic crystal nanocavity with an embedded quantum dot based on optical microscopic photoluminescence imaging," *Applied Physics Letters* **102**, 011110 (2013).
- [58] L. Sapienza, M. Davanço, A. Badolato, and K. Srinivasan, "Nanoscale optical positioning of single quantum dots for bright and pure single-photon emission," *Nature Communications* **6** (2015).
- [59] J. Liu, M. I. Davanço, L. Sapienza, K. Konthasinghe, J. V. De Miranda Cardoso, J. D. Song, A. Badolato, and K. Srinivasan, "Cryogenic photoluminescence imaging system for nanoscale positioning of single quantum emitters," *Review of Scientific Instruments* **88**, 023116 (2017).
- [60] M. B. Panish and H. C. Casey, "Temperature Dependence of the Energy Gap in GaAs and GaP," *Journal of Applied Physics* **40**, 163–167 (1969).

Bibliography

- [61] W. Porod and D. K. Ferry, "Modification of the virtual-crystal approximation for ternary III-V compounds," *Physical Review B* **27**, 2587–2589 (1983).
- [62] M. I. Dyakonov, "Basics of Semiconductor and Spin Physics," in "Springer Series in Solid-State Sciences," (Springer Berlin Heidelberg, 2008), pp. 1–28.
- [63] P. Hawrylak and M. Korkusiński, "Electronic Properties of Self-Assembled Quantum Dots," in "Single Quantum Dots: Fundamentals, Applications and New Concepts," , vol. 90 of *Topics in Applied Physics*, P. Michler, ed. (Springer, Berlin, 2003), pp. 25–91.
- [64] F. Rossi, "Fundamentals of Zero-Dimensional Nanostructures," in "Semiconductor Macroatoms: Basic Physics and Quantum-Device Applications," (Imperial College Press, 2005), pp. 1–41.
- [65] R. M. Stevenson, R. J. Young, P. Atkinson, K. Cooper, D. A. Ritchie, and A. J. Shields, "A semiconductor source of triggered entangled photon pairs," *Nature* **439**, 179–182 (2006).
- [66] A. J. Brash, L. M. P. P. Martins, F. Liu, J. H. Quilter, A. J. Ramsay, M. S. Skolnick, and A. M. Fox, "High-fidelity initialization of long-lived quantum dot hole spin qubits by reduced fine-structure splitting," *Physical Review B* **92**, 121301 (2015).
- [67] M. Bayer, A. Kuther, A. Forchel, A. Gorbunov, V. B. Timofeev, F. Schäfer, J. P. Reithmaier, T. L. Reinecke, and S. N. Walck, "Electron and Hole g Factors and Exchange Interaction from Studies of the Exciton Fine Structure in $\text{In}_{0.60}\text{Ga}_{0.40}\text{As}$ Quantum Dots," *Physical Review Letters* **82**, 1748–1751 (1999).
- [68] D. Gammon, E. S. Snow, B. V. Shanabrook, D. S. Katzer, and D. Park, "Fine Structure Splitting in the Optical Spectra of Single GaAs Quantum Dots," *Physical Review Letters* **76**, 3005–3008 (1996).
- [69] K. Kowalik, O. Krebs, A. Lemaître, S. Laurent, P. Senellart, P. Voisin, and J. A.

- Gaj, "Influence of an in-plane electric field on exciton fine structure in InAs-GaAs self-assembled quantum dots," *Applied Physics Letters* **86**, 041907 (2005).
- [70] S. Seidl, M. Kroner, A. Högele, K. Karrai, R. J. Warburton, A. Badolato, and P. M. Petroff, "Effect of uniaxial stress on excitons in a self-assembled quantum dot," *Applied Physics Letters* **88**, 203113 (2006).
- [71] W. Langbein, P. Borri, U. Woggon, V. Stavarache, D. Reuter, and A. D. Wieck, "Control of fine-structure splitting and biexciton binding in $\text{In}_x\text{Ga}_{1-x}\text{As}$ quantum dots by annealing," *Physical Review B* **69**, 161301 (2004).
- [72] R. Singh and G. Bester, "Nanowire Quantum Dots as an Ideal Source of Entangled Photon Pairs," *Physical Review Letters* **103**, 063601 (2009).
- [73] P. W. Fry, I. E. Itskevich, D. J. Mowbray, M. S. Skolnick, and J. J. Finley et al., "Inverted Electron-Hole Alignment in InAs-GaAs Self-Assembled Quantum Dots," *Physical Review Letters* **84**, 733–736 (2000).
- [74] J. J. Finley, M. Sabathil, P. Vogl, G. Abstreiter, and R. Oulton et al., "Quantum-confined Stark shifts of charged exciton complexes in quantum dots," *Physical Review B* **70**, 201308 (2004).
- [75] A. J. Bennett, R. B. Patel, J. Skiba-Szymanska, C. A. Nicoll, I. Farrer, D. A. Ritchie, and A. J. Shields, "Giant Stark effect in the emission of single semiconductor quantum dots," *Applied Physics Letters* **97**, 031104 (2010).
- [76] B. Alén, F. Bickel, K. Karrai, R. J. Warburton, and P. M. Petroff, "Stark-shift modulation absorption spectroscopy of single quantum dots," *Applied Physics Letters* **83**, 2235–2237 (2003).
- [77] B. D. Gerardot, S. Seidl, P. A. Dalgarno, R. J. Warburton, D. Granados, J. M. Garcia, K. Kowalik, O. Krebs, K. Karrai, A. Badolato, and P. M. Petroff, "Manipulating exciton fine structure in quantum dots with a lateral electric field," *Applied Physics Letters* **90**, 041101 (2007).

Bibliography

- [78] M. M. Vogel, S. M. Ulrich, R. Hafenbrak, P. Michler, L. Wang, A. Rastelli, and O. G. Schmidt, "Influence of lateral electric fields on multiexcitonic transitions and fine structure of single quantum dots," *Applied Physics Letters* **91**, 051904 (2007).
- [79] T. Pregalato, "Deterministic quantum photonic devices based on self-assembled quantum dots," Ph.D. thesis, University of Copenhagen (2019).
- [80] S. H. Autler and C. H. Townes, "Stark Effect in Rapidly Varying Fields," *Physical Review* **100**, 703–722 (1955).
- [81] B. R. Mollow, "Power Spectrum of Light Scattered by Two-Level Systems," *Physical Review* **188**, 1969–1975 (1969).
- [82] S. L. Portalupi and P. Michler, "Resonantly Excited Quantum Dots: Superior Non-classical Light Sources for Quantum Information," in "Quantum Dots for Quantum Information Technologies," , P. Michler, ed. (Springer International Publishing, Cham, 2017), chap. 3, pp. 77–121.
- [83] A. J. Brash, F. Liu, and A. M. Fox, "Ultrafast Manipulation of Excitons and Spins in Quantum Dots," in "Quantum Dots for Quantum Information Technologies," , P. Michler, ed. (Springer International Publishing, Cham, 2017), chap. 10, pp. 325–357.
- [84] A. Vagov, V. M. Axt, T. Kuhn, W. Langbein, P. Borri, and U. Woggon, "Non-monotonous temperature dependence of the initial decoherence in quantum dots," *Physical Review B* **70**, 201305 (2004).
- [85] P. Borri and W. Langbein., "Dephasing Processes and Carrier Dynamics in (In, Ga)AS Quantum Dots," in "Single Quantum Dots: Fundamentals, Applications and New Concepts," , vol. 90 of *Topics in Applied Physics*, P. Michler, ed. (Springer, Berlin, 2003), pp. 1–24.

- [86] M. J. Steer, D. J. Mowbray, W. R. Tribe, M. S. Skolnick, M. D. Sturge, M. Hopkinson, A. G. Cullis, C. R. Whitehouse, and R. Murray, "Electronic energy levels and energy relaxation mechanisms in self-organized InAs/GaAs quantum dots," *Physical Review B* **54**, 17738–17744 (1996).
- [87] R. Heitz, M. Grundmann, N. N. Ledentsov, L. Eckey, M. Veit, D. Bimberg, V. M. Ustinov, A. Y. Egorov, A. E. Zhukov, P. S. Kop'ev, and Z. I. Alferov, "Multiphonon-relaxation processes in self-organized InAs/GaAs quantum dots," *Applied Physics Letters* **68**, 361–363 (1996).
- [88] R. Heitz, M. Veit, N. N. Ledentsov, A. Hoffmann, D. Bimberg, V. M. Ustinov, P. S. Kop'ev, and Z. I. Alferov, "Energy relaxation by multiphonon processes in InAs/GaAs quantum dots," *Physical Review B* **56**, 10435–10445 (1997).
- [89] E. Stock, M.-R. Dachner, T. Warming, A. Schliwa, A. Lochmann, A. Hoffmann, A. I. Toropov, A. K. Bakarov, I. A. Derebezov, M. Richter, V. A. Haisler, A. Knorr, and D. Bimberg, "Acoustic and optical phonon scattering in a single In(Ga)As quantum dot," *Physical Review B* **83**, 041304 (2011).
- [90] U. R. O. Madelung, W. von der Osten, *Landolt-Börnstein-Semiconductors: Intrinsic Properties of Group IV Elements and II-V, II-VI and I-VII Compounds*, vol. III/22a (Springer, Berlin, 1987).
- [91] T. Flissikowski, A. Hundt, M. Lowisch, M. Rabe, and F. Henneberger, "Photon Beats from a Single Semiconductor Quantum Dot," *Physical Review Letters* **86**, 3172–3175 (2001).
- [92] H. Kumano, H. Kobayashi, S. Ekuni, Y. Hayashi, M. Jo, H. Sasakura, S. Adachi, S. Muto, and I. Suemune, "Excitonic spin-state preservation mediated by optical-phonon resonant excitation in a single quantum dot," *Physical Review B* **78**, 081306 (2008).
- [93] K. H. Madsen, S. Ates, J. Liu, A. Javadi, S. M. Albrecht, I. Yeo, S. Stobbe, and

Bibliography

- P. Lodahl, "Efficient out-coupling of high-purity single photons from a coherent quantum dot in a photonic-crystal cavity," *Physical Review B* **90**, 155303 (2014).
- [94] E. V. Denning, J. Iles-Smith, N. Gregersen, and J. Mørk, "Phonon effects in quantum dot single-photon sources," *Opt. Mater. Express* **10**, 222–239 (2020).
- [95] J. Iles-Smith, D. P. S. McCutcheon, A. Nazir, and J. Mørk, "Phonon scattering inhibits simultaneous near-unity efficiency and indistinguishability in semiconductor single-photon sources," *Nature Photonics* **11**, 521 (2017).
- [96] A. J. Ramsay, A. V. Gopal, E. M. Gauger, A. Nazir, B. W. Lovett, A. M. Fox, and M. S. Skolnick, "Damping of Exciton Rabi Rotations by Acoustic Phonons in Optically Excited InGaAs/GaAs Quantum Dots," *Physical Review Letters* **104**, 017402 (2010).
- [97] J. Förstner, C. Weber, J. Danckwerts, and A. Knorr, "Phonon-Assisted Damping of Rabi Oscillations in Semiconductor Quantum Dots," *Physical Review Letters* **91**, 127401 (2003).
- [98] A. J. Ramsay, T. M. Godden, S. J. Boyle, E. M. Gauger, A. Nazir, B. W. Lovett, A. M. Fox, and M. S. Skolnick, "Phonon-Induced Rabi-Frequency Renormalization of Optically Driven Single InGaAs / GaAs Quantum Dots," *Physical Review Letters* **105**, 177402 (2010).
- [99] J. Iles-Smith, D. P. S. McCutcheon, J. Mørk, and A. Nazir, "Limits to coherent scattering and photon coalescence from solid-state quantum emitters," *Physical Review B* **95**, 201305 (2017).
- [100] T. Grange, N. Somaschi, C. Antón, L. De Santis, G. Coppola, V. Giesz, A. Lemaître, I. Sagnes, A. Auffèves, and P. Senellart, "Reducing Phonon-Induced Decoherence in Solid-State Single-Photon Sources with Cavity Quantum Electrodynamics," *Physical Review Letters* **118**, 253602 (2017).

- [101] L. Jacak, P. Machnikowski, J. Krasnyj, and P. Zoller, “Coherent and incoherent phonon processes in artificial atoms,” *The European Physical Journal D* **22**, 319–331 (2003).
- [102] J. I. Climente, A. Bertoni, G. Goldoni, and E. Molinari, “Phonon-induced electron relaxation in weakly confined single and coupled quantum dots,” *Physical Review B* **74**, 035313 (2006).
- [103] G. Bester, A. Zunger, X. Wu, and D. Vanderbilt, “Effects of linear and nonlinear piezoelectricity on the electronic properties of InAs/GaAs quantum dots,” *Physical Review B* **74**, 081305 (2006).
- [104] E. M. Purcell, H. C. Torrey, and R. V. Pound, “Resonance Absorption by Nuclear Magnetic Moments in a Solid,” *Physical Review* **69**, 37–38 (1946).
- [105] D. Englund, D. Fattal, E. Waks, G. Solomon, and B. Zhang et al., “Controlling the Spontaneous Emission Rate of Single Quantum Dots in a Two-Dimensional Photonic Crystal,” *Physical Review Letters* **95**, 013904 (2005).
- [106] F. Liu, A. J. Brash, J. O’Hara, L. M. P. P. Martins, C. L. Phillips, R. J. Coles, B. Royall, E. Clarke, C. Bentham, N. Prtljaga, I. E. Itskevich, L. R. Wilson, M. S. Skolnick, and A. M. Fox, “High Purcell factor generation of indistinguishable on-chip single photons,” *Nature Nanotechnology* **13**, 835–840 (2018).
- [107] J. P. Reithmaier, G. Sek, A. Löffler, C. Hofmann, S. Kuhn, S. Reitzenstein, L. V. Keldysh, V. D. Kulakovskii, T. L. Reinecke, and A. Forchel, “Strong coupling in a single quantum dot–semiconductor microcavity system,” *Nature* **432**, 197–200 (2004).
- [108] T. B. Norris, J.-K. Rhee, C.-Y. Sung, Y. Arakawa, M. Nishioka, and C. Weisbuch, “Time-resolved vacuum Rabi oscillations in a semiconductor quantum microcavity,” *Physical Review B* **50**, 14663–14666 (1994).

Bibliography

- [109] I. I. Rabi, "Space Quantization in a Gyating Magnetic Field," *Physical Review* **51**, 652–654 (1937).
- [110] E. T. Jaynes and F. W. Cummings, "Comparison of quantum and semiclassical radiation theories with application to the beam maser," *Proceedings of the IEEE* **51**, 89–109 (1963).
- [111] S. G. Johnson and J. D. Joannopoulos, "Block-iterative frequency-domain methods for Maxwell's equations in a planewave basis," *Optics Express* **8**, 173–190 (2001).
- [112] M. Lončar, J. Vučković, and A. Scherer, "Methods for controlling positions of guided modes of photonic-crystal waveguides," *Journal of the Optical Society of America B: Optical Physics* **18**, 1362–1368 (2001).
- [113] R. J. Coles, "Quantum Optical Circuits using III-V Nanophotonic Structures," Ph.D. thesis, University of Sheffield (2015).
- [114] E. Yablonovitch, "Inhibited Spontaneous Emission in Solid-State Physics and Electronics," *Physical Review Letters* **58**, 2059–2062 (1987).
- [115] J. D. Joannopoulos, *Photonic crystals : molding the flow of light* (Princeton University Press, Princeton, N.J. ; Chichester, 1995).
- [116] S. G. Johnson, P. R. Villeneuve, S. Fan, and J. D. Joannopoulos, "Linear waveguides in photonic-crystal slabs," *Physical Review B* **62**, 8212–8222 (2000).
- [117] T. F. Krauss, "Slow light in photonic crystal waveguides," *Journal of Physics D: Applied Physics* **40**, 2666–2670 (2007).
- [118] S. Hughes, "Enhanced single-photon emission from quantum dots in photonic crystal waveguides and nanocavities," *Optics Letters* **29**, 2659–2661 (2004).
- [119] V. S. C. Manga Rao and S. Hughes, "Single quantum-dot Purcell factor and β factor in a photonic crystal waveguide," *Physical Review B* **75**, 205437 (2007).

- [120] A. C. T. Thijssen, M. J. Cryan, J. G. Rarity, and R. Oulton, "Transfer of arbitrary quantum emitter states to near-field photon superpositions in nanocavities," *Optics Express* **20**, 22412–22428 (2012).
- [121] R. J. Coles, N. Prtljaga, B. Royall, I. J. Luxmoore, A. M. Fox, and M. S. Skolnick, "Waveguide-coupled photonic crystal cavity for quantum dot spin readout," *Optics Express* **22**, 2376–2385 (2014).
- [122] M. Shirane, S. Kono, J. Ushida, S. Ohkouchi, N. Ikeda, Y. Sugimoto, and A. Tomita, "Mode identification of high-quality-factor single-defect nanocavities in quantum dot-embedded photonic crystals," *Journal of Applied Physics* **101**, 073107 (2007).
- [123] Y. Akahane, T. Asano, B.-S. Song, and S. Noda, "High-Q photonic nanocavity in a two-dimensional photonic crystal," *Nature* **425**, 944–947 (2003).
- [124] A. Faraon, E. Waks, D. Englund, I. Fushman, and J. Vučković, "Efficient photonic crystal cavity-waveguide couplers," *Applied Physics Letters* **90**, 073102 (2007).
- [125] P. Velha, E. Picard, T. Charvolin, E. Hadji, J. C. Rodier, P. Lalanne, and D. Peyrade, "Ultra-High Q/V Fabry-Perot microcavity on SOI substrate," *Optics Express* **15**, 16090–16096 (2007).
- [126] Q. Quan, P. B. Deotare, and M. Loncar, "Photonic crystal nanobeam cavity strongly coupled to the feeding waveguide," *Applied Physics Letters* **96**, 203102 (2010).
- [127] Q. Quan and M. Loncar, "Deterministic design of wavelength scale, ultra-high Q photonic crystal nanobeam cavities," *Optics Express* **19**, 18529–18542 (2011).
- [128] A. Dousse, L. Lanco, J. Suffczyński, E. Semenova, A. Miard, A. Lemaître, I. Sagnes, C. Roblin, J. Bloch, and P. Senellart, "Controlled Light-Matter Cou-

Bibliography

- pling for a Single Quantum Dot Embedded in a Pillar Microcavity Using Far-Field Optical Lithography," *Physical Review Letters* **101**, 267404 (2008).
- [129] C. Schneider, P. Gold, S. Reitzenstein, S. Höfling, and M. Kamp, "Quantum dot micropillar cavities with quality factors exceeding 250, 000," *Applied Physics B* **122** (2016).
- [130] H. Ollivier, I. Maillette de Buy Wenniger, S. Thomas, S. C. Wein, A. Harouri, G. Coppola, P. Hilaire, C. Millet, A. Lemaître, I. Sagnes, O. Krebs, L. Lanco, J. C. Loredó, C. Antón, N. Somaschi, and P. Senellart, "Reproducibility of High-Performance Quantum Dot Single-Photon Sources," *ACS Photonics* **7**, 1050–1059 (2020).
- [131] P. Michler, A. Kiraz, C. Becher, W. V. Schoenfeld, P. M. Petroff, L. Zhang, E. Hu, and A. Imamoglu, "A Quantum Dot Single-Photon Turnstile Device," *Science* **290**, 2282–2285 (2000).
- [132] A. Kiraz, P. Michler, C. Becher, B. Gayral, A. Imamoglu, L. Zhang, E. Hu, W. V. Schoenfeld, and P. M. Petroff, "Cavity-quantum electrodynamics using a single InAs quantum dot in a microdisk structure," *Applied Physics Letters* **78**, 3932–3934 (2001).
- [133] E. Peter, P. Senellart, D. Martrou, A. Lemaître, J. Hours, J. M. Gérard, and J. Bloch, "Exciton-Photon Strong-Coupling Regime for a Single Quantum Dot Embedded in a Microcavity," *Physical Review Letters* **95**, 067401 (2005).
- [134] F. Salin, J. Squier, and M. Piché, "Mode locking of Ti:Al₂O₃ lasers and self-focusing: a Gaussian approximation," *Optics Letters* **16**, 1674–1676 (1991).
- [135] T. H. Stievater, X. Li, D. G. Steel, D. Gammon, D. S. Katzer, D. Park, C. Piermarocchi, and L. J. Sham, "Rabi Oscillations of Excitons in Single Quantum Dots," *Physical Review Letters* **87**, 133603 (2001).

- [136] H. Kamada, H. Gotoh, J. Temmyo, T. Takagahara, and H. Ando, “Exciton Rabi Oscillation in a Single Quantum Dot,” *Physical Review Letters* **87**, 246401 (2001).
- [137] H. Htoon, T. Takagahara, D. Kulik, O. Baklenov, A. L. Holmes, and C. K. Shih, “Interplay of Rabi Oscillations and Quantum Interference in Semiconductor Quantum Dots,” *Physical Review Letters* **88**, 087401 (2002).
- [138] A. Zrenner, E. Beham, S. Stufler, F. Findeis, M. Bichler, and G. Abstreiter, “Coherent properties of a two-level system based on a quantum-dot photodiode,” *Nature* **418**, 612–614 (2002).
- [139] J. O’Hara, “Quantum Light with Quantum Dots in III-V Photonic Integrated Circuits: Towards Scalable Quantum Computing Architectures,” Ph.D. thesis, University of Sheffield (2017).
- [140] K. A. Fischer, L. Hanschke, M. Kremser, J. J. Finley, K. Müller, and J. Vučković, “Pulsed Rabi oscillations in quantum two-level systems: beyond the area theorem,” *Quantum Science and Technology* **3**, 014006 (2017).
- [141] J. P. McCaffrey, M. D. Robertson, S. Fafard, Z. R. Wasilewski, E. M. Griswold, and L. D. Madsen, “Determination of the size, shape, and composition of indium-flushed self-assembled quantum dots by transmission electron microscopy,” *Journal of Applied Physics* **88**, 2272–2277 (2000).
- [142] C. Bentham, I. E. Itskevich, R. J. Coles, B. Royall, E. Clarke, J. O’Hara, N. Prtljaga, A. M. Fox, M. S. Skolnick, and L. R. Wilson, “On-chip electrically controlled routing of photons from a single quantum dot,” *Applied Physics Letters* **106**, 221101 (2015).
- [143] A. J. Brash, “Ultrafast Dynamics of Single Quantum Dots,” Ph.D. thesis, University of Sheffield (2016).

Bibliography

- [144] A. Faraon, I. Fushman, D. Englund, N. Stoltz, P. Petroff, and J. Vučković, “Dipole induced transparency in waveguide coupled photonic crystal cavities,” *Optics Express* **16**, 12154–12162 (2008).
- [145] X. Zhou, I. Kulkova, T. Lund-Hansen, S. L. Hansen, P. Lodahl, and L. Midolo, “High-efficiency shallow-etched grating on GaAs membranes for quantum photonic applications,” *Applied Physics Letters* **113**, 251103 (2018).
- [146] D. Istrati, Y. Pilnyak, J. C. Loredó, C. Antón, N. Somaschi, P. Hilaire, H. Ollivier, M. Esmann, L. Cohen, L. Vidro, C. Millet, A. Lemaître, I. Sagnes, A. Harouri, L. Lanco, P. Senellart, and H. S. Eisenberg, “Sequential generation of linear cluster states from a single photon emitter,” (2019).
- [147] R. H. Brown and R. Q. Twiss, “Correlation between Photons in two Coherent Beams of Light,” *Nature* **177**, 27–29 (1956).
- [148] C. K. Hong, Z. Y. Ou, and L. Mandel, “Measurement of subpicosecond time intervals between two photons by interference,” *Physical Review Letters* **59**, 2044–2046 (1987).
- [149] C. Santori, D. Fattal, J. Vučković, G. S. Solomon, and Y. Yamamoto, “Indistinguishable photons from a single-photon device,” *Nature* **419**, 594–597 (2002).
- [150] A. J. Bennett, D. C. Unitt, A. J. Shields, P. Atkinson, and D. A. Ritchie, “Influence of exciton dynamics on the interference of two photons from a microcavity single-photon source,” *Optics Express* **13**, 7772–7778 (2005).
- [151] S. Ates, S. M. Ulrich, S. Reitzenstein, A. Löffler, A. Forchel, and P. Michler, “Post-Selected Indistinguishable Photons from the Resonance Fluorescence of a Single Quantum Dot in a Microcavity,” *Physical Review Letters* **103**, 167402 (2009).
- [152] S. Laurent, S. Varoutsis, L. Le Gratiet, A. Lemaître, I. Sagnes, F. Raineri, A. Levenson, I. Robert-Philip, and I. Abram, “Indistinguishable single photons from

- a single-quantum dot in a two-dimensional photonic crystal cavity," *Applied Physics Letters* **87**, 163107 (2005).
- [153] H. Fearn and R. Loudon, "Theory of two-photon interference," *Journal of the Optical Society of America B: Optical Physics* **6**, 917–927 (1989).
- [154] A. M. Brańczyk, "Hong-Ou-Mandel Interference," arXiv e-prints p. arXiv:1711.00080 (2017).
- [155] N. Somaschi, V. Giesz, L. De Santis, J. C. Loredo, and M. P. Almeida et al., "Near-optimal single-photon sources in the solid state," *Nat Photon* **10**, 340–345 (2016).
- [156] C. F. Wang, A. Badolato, I. Wilson-Rae, P. M. Petroff, E. Hu, J. Urayama, and A. Imamoglu, "Optical properties of single InAs quantum dots in close proximity to surfaces," *Applied Physics Letters* **85**, 3423–3425 (2004).
- [157] A. Majumdar, E. D. Kim, and J. Vučković, "Effect of photogenerated carriers on the spectral diffusion of a quantum dot coupled to a photonic crystal cavity," *Physical Review B* **84**, 195304 (2011).
- [158] A. Thoma, P. Schnauber, M. Gschrey, M. Seifried, J. Wolters, J.-H. Schulze, A. Strittmatter, S. Rodt, A. Carmele, A. Knorr, T. Heindel, and S. Reitzenstein, "Exploring Dephasing of a Solid-State Quantum Emitter via Time- and Temperature-Dependent Hong-Ou-Mandel Experiments," *Physical Review Letters* **116**, 033601 (2016).
- [159] J. C. Loredo, N. A. Zakaria, N. Somaschi, C. Anton, L. de Santis, V. Giesz, T. Grange, M. A. Broome, O. Gazzano, G. Coppola, I. Sagnes, A. Lemaitre, A. Auffeves, P. Senellart, M. P. Almeida, and A. G. White, "Scalable performance in solid-state single-photon sources," *Optica* **3**, 433–440 (2016).
- [160] F. Y. Wu, R. E. Grove, and S. Ezekiel, "Investigation of the Spectrum of Reso-

Bibliography

- nance Fluorescence Induced by a Monochromatic Field,” *Physical Review Letters* **35**, 1426–1429 (1975).
- [161] H. Gibbs and T. Venkatesan, “Direct observation of fluorescence narrower than the natural linewidth,” *Optics Communications* **17**, 87 – 90 (1976).
- [162] J. Volz, M. Weber, D. Schlenk, W. Rosenfeld, C. Kurtsiefer, and H. Weinfurter, “An atom and a photon,” *Laser Physics* **17**, 1007–1016 (2007).
- [163] H. S. Nguyen, G. Sallen, C. Voisin, P. Roussignol, C. Diederichs, and G. Cassabois, “Ultra-coherent single photon source,” *Applied Physics Letters* **99**, 261904 (2011).
- [164] K. Konthasinghe, J. Walker, M. Peiris, C. K. Shih, Y. Yu, M. F. Li, J. F. He, L. J. Wang, H. Q. Ni, Z. C. Niu, and A. Muller, “Coherent versus incoherent light scattering from a quantum dot,” *Physical Review B* **85**, 235315 (2012).
- [165] R. Proux, M. Maragkou, E. Baudin, C. Voisin, P. Roussignol, and C. Diederichs, “Measuring the Photon Coalescence Time Window in the Continuous-Wave Regime for Resonantly Driven Semiconductor Quantum Dots,” *Physical Review Letters* **114**, 067401 (2015).
- [166] A. J. Bennett, J. P. Lee, D. J. P. Ellis, T. Meany, E. Murray, F. F. Floether, J. P. Griffiths, I. Farrer, D. A. Ritchie, and A. J. Shields, “Cavity-enhanced coherent light scattering from a quantum dot,” *Science Advances* **2**, e1501256–e1501256 (2016).
- [167] C. Cohen-Tannoudji, J. Dupont-Roc, and G. Grynberg, *Atom—Photon Interactions: Basic Processes and Applications* (Wiley, 1998).
- [168] C. Matthiesen, M. Geller, C. H. H. Schulte, C. Le Gall, J. Hansom, Z. Li, M. Hugues, E. Clarke, and M. Atatüre, “Phase-locked indistinguishable photons with synthesized waveforms from a solid-state source,” *Nature Communications* **4**, 1600 (2013).

- [169] Y. He, Y.-M. He, Y.-J. Wei, X. Jiang, M.-C. Chen, F.-L. Xiong, Y. Zhao, C. Schneider, M. Kamp, S. Höfling, C.-Y. Lu, and J.-W. Pan, “Indistinguishable Tunable Single Photons Emitted by Spin-Flip Raman Transitions in InGaAs Quantum Dots,” *Physical Review Letters* **111**, 237403 (2013).
- [170] T. M. Sweeney, S. G. Carter, A. S. Bracker, M. Kim, C. S. Kim, L. Yang, P. M. Vora, P. G. Brereton, E. R. Cleveland, and D. Gammon, “Cavity-stimulated Raman emission from a single quantum dot spin,” *Nature Photonics* **8**, 442–447 (2014).
- [171] E. V. Denning, J. Iles-Smith, D. P. S. McCutcheon, and J. Mork, “Protocol for generating multiphoton entangled states from quantum dots in the presence of nuclear spin fluctuations,” *Physical Review A* **96**, 062329 (2017).
- [172] D. Scerri, R. N. E. Malein, B. D. Gerardot, and E. M. Gauger, “Frequency-encoded linear cluster states with coherent Raman photons,” *Physical Review A* **98**, 022318 (2018).
- [173] A. Javadi, I. Söllner, M. Arcari, S. L. Hansen, L. Midolo, S. Mahmoodian, G. Kiršanskė, T. Pregnolato, E. H. Lee, J. D. Song, S. Stobbe, and P. Lodahl, “Single-photon non-linear optics with a quantum dot in a waveguide,” *Nature Communications* **6** (2015).
- [174] A. Sipahigil, R. E. Evans, D. D. Sukachev, M. J. Burek, J. Borregaard, M. K. Bhaskar, C. T. Nguyen, J. L. Pacheco, H. A. Atikian, C. Meuwly, R. M. Camacho, F. Jelezko, E. Bielejec, H. Park, M. Lončar, and M. D. Lukin, “An integrated diamond nanophotonics platform for quantum-optical networks,” *Science* **354**, 847–850 (2016).
- [175] D. Hallett, A. P. Foster, D. L. Hurst, B. Royall, P. Kok, E. Clarke, I. E. Itskevich, A. M. Fox, M. S. Skolnick, and L. R. Wilson, “Electrical control of nonlinear quantum optics in a nano-photonic waveguide,” *Optica* **5**, 644–650 (2018).
- [176] A. Delteil, Z. Sun, W. bo Gao, E. Togan, S. Faelt, and A. Imamoglu, “Generation

Bibliography

- of heralded entanglement between distant hole spins,” *Nature Physics* **12**, 218–223 (2015).
- [177] R. Stockill, M. J. Stanley, L. Huthmacher, E. Clarke, M. Hugues, A. J. Miller, C. Matthiesen, C. Le Gall, and M. Atatüre, “Phase-Tuned Entangled State Generation between Distant Spin Qubits,” *Physical Review Letters* **119**, 010503 (2017).
- [178] J. Houel, A. V. Kuhlmann, L. Greuter, F. Xue, M. Poggio, B. D. Gerardot, P. A. Dalgarno, A. Badolato, P. M. Petroff, A. Ludwig, D. Reuter, A. D. Wieck, and R. J. Warburton, “Probing Single-Charge Fluctuations at a GaAs/AlAs Interface Using Laser Spectroscopy on a Nearby InGaAs Quantum Dot,” *Physical Review Letters* **108**, 107401 (2012).
- [179] A. V. Kuhlmann, J. Houel, A. Ludwig, L. Greuter, D. Reuter, A. D. Wieck, M. Poggio, and R. J. Warburton, “Charge noise and spin noise in a semiconductor quantum device,” *Nature Physics* **9**, 570–575 (2013).
- [180] E. A. Muljarov and R. Zimmermann, “Dephasing in Quantum Dots: Quadratic Coupling to Acoustic Phonons,” *Physical Review Letters* **93**, 237401 (2004).
- [181] A. Reigue, J. Iles-Smith, F. Lux, L. Monniello, M. Bernard, F. Margailan, A. Lemaitre, A. Martinez, D. P. S. McCutcheon, J. Mørk, R. Hostein, and V. Voliotis, “Probing Electron-Phonon Interaction through Two-Photon Interference in Resonantly Driven Semiconductor Quantum Dots,” *Physical Review Letters* **118**, 233602 (2017).
- [182] H. Wang, Z.-C. Duan, Y.-H. Li, S. Chen, J.-P. Li, Y.-M. He, M.-C. Chen, Y. He, X. Ding, C.-Z. Peng, C. Schneider, M. Kamp, S. Höfling, C.-Y. Lu, and J.-W. Pan, “Near-Transform-Limited Single Photons from an Efficient Solid-State Quantum Emitter,” *Physical Review Letters* **116**, 213601 (2016).
- [183] L. Monniello, C. Tonin, R. Hostein, A. Lemaitre, A. Martinez, V. Voliotis, and

- R. Grousson, "Excitation-induced dephasing in a resonantly driven InAs/GaAs quantum dot," *Physical Review Letters* **111**, 026403 (2013).
- [184] B. Krummheuer, V. M. Axt, and T. Kuhn, "Theory of pure dephasing and the resulting absorption line shape in semiconductor quantum dots," *Physical Review B* **65**, 195313 (2002).
- [185] P. Kaer and J. Mørk, "Decoherence in semiconductor cavity QED systems due to phonon couplings," *Physical Review B* **90**, 035312 (2014).
- [186] D. P. S. McCutcheon, "Optical signatures of non-Markovian behavior in open quantum systems," *Physical Review A* **93**, 022119 (2016).
- [187] L. Besombes, K. Kheng, L. Marsal, and H. Mariette, "Acoustic phonon broadening mechanism in single quantum dot emission," *Physical Review B* **63**, 155307 (2001).
- [188] N. R. Jungwirth and G. D. Fuchs, "Optical Absorption and Emission Mechanisms of Single Defects in Hexagonal Boron Nitride," *Physical Review Letters* **119**, 057401 (2017).
- [189] E. Neu, D. Steinmetz, J. Riedrich-Möller, S. Gsell, M. Fischer, M. Schreck, and C. Becher, "Single photon emission from silicon-vacancy colour centres in chemical vapour deposition nano-diamonds on iridium," *New Journal of Physics* **13**, 025012 (2011).
- [190] A. Jeantet, Y. Chassagneux, C. Raynaud, P. Roussignol, J. S. Lauret, B. Besga, J. Estève, J. Reichel, and C. Voisin, "Widely Tunable Single-Photon Source from a Carbon Nanotube in the Purcell Regime," *Physical Review Letters* **116**, 247402 (2016).
- [191] D. Christiansen, M. Selig, G. Berghäuser, R. Schmidt, I. Niehues, R. Schneider, A. Arora, S. M. de Vasconcellos, R. Bratschitsch, E. Malic, and A. Knorr,

Bibliography

- “Phonon Sidebands in Monolayer Transition Metal Dichalcogenides,” *Physical Review Letters* **119**, 187402 (2017).
- [192] C. Clear, R. C. Schofield, K. D. Major, J. Iles-Smith, A. S. Clark, and D. P. S. McCutcheon, “Phonon-induced optical dephasing in single organic molecules,” *Physical Review Letters* **124**, 153602 (2020).
- [193] P. Kaer, N. Gregersen, and J. Mork, “The role of phonon scattering in the indistinguishability of photons emitted from semiconductor cavity QED systems,” *New Journal of Physics* **15**, 035027 (2013).
- [194] P. Borri, W. Langbein, U. Woggon, V. Stavarache, D. Reuter, and A. D. Wieck, “Exciton dephasing via phonon interactions in InAs quantum dots: Dependence on quantum confinement,” *Physical Review B* **71**, 115328 (2005).
- [195] T. Jakubczyk, V. Delmonte, S. Fischbach, D. Wigger, D. E. Reiter, Q. Mermillod, P. Schnauber, A. Kaganskiy, J.-H. Schulze, A. Strittmatter, S. Rodt, W. Langbein, T. Kuhn, S. Reitzenstein, and J. Kasprzak, “Impact of Phonons on Dephasing of Individual Excitons in Deterministic Quantum Dot Microlenses,” *ACS Photonics* **3**, 2461–2466 (2016).
- [196] A. Nazir and D. P. S. McCutcheon, “Modelling exciton–phonon interactions in optically driven quantum dots,” *Journal of Physics: Condensed Matter* **28**, 103002 (2016).
- [197] D. P. S. McCutcheon and A. Nazir, “Quantum dot Rabi rotations beyond the weak exciton–phonon coupling regime,” *New Journal of Physics* **12**, 113042 (2010).
- [198] H.-P. Breuer and F. Petruccione, *The Theory of Open Quantum Systems* (Oxford University Press on Demand, New York, 2002).
- [199] C. Roy and S. Hughes, “Phonon-Dressed Mollow Triplet in the Regime of Cav-

- ity Quantum Electrodynamics: Excitation-Induced Dephasing and Nonperturbative Cavity Feeding Effects,” *Physical Review Letters* **106**, 247403 (2011).
- [200] A. J. Brash, J. Iles-Smith, C. L. Phillips, D. P. S. McCutcheon, J. O’Hara, E. Clarke, B. Royall, L. R. Wilson, J. Mørk, M. S. Skolnick, A. M. Fox, and A. Nazir, “Light Scattering from Solid-State Quantum Emitters: Beyond the Atomic Picture,” *Physical Review Letters* **123**, 167403 (2019).
- [201] M. Glässl, M. D. Croitoru, A. Vagov, V. M. Axt, and T. Kuhn, “Influence of the pulse shape and the dot size on the decay and reappearance of Rabi rotations in laser driven quantum dots,” *Physical Review B* **84**, 125304 (2011).
- [202] T. Calarco, A. Datta, P. Fedichev, E. Pazy, and P. Zoller, “Spin-based all-optical quantum computation with quantum dots: Understanding and suppressing decoherence,” *Physical Review A* **68**, 012310 (2003).
- [203] K. Roy-Choudhury and S. Hughes, “Quantum theory of the emission spectrum from quantum dots coupled to structured photonic reservoirs and acoustic phonons,” *Physical Review B* **92**, 205406 (2015).
- [204] E. V. Denning, J. Iles-Smith, A. D. Osterkryger, N. Gregersen, and J. Mork, “Cavity-waveguide interplay in optical resonators and its role in optimal single-photon sources,” *Physical Review B* **98**, 121306 (2018).
- [205] J. H. Quilter, A. J. Brash, F. Liu, M. Glässl, A. M. Barth, V. M. Axt, A. J. Ramsay, M. S. Skolnick, and A. M. Fox, “Phonon-Assisted Population Inversion of a Single InGaAs/GaAs Quantum Dot by Pulsed Laser Excitation,” *Physical Review Letters* **114**, 137401 (2015).
- [206] A. Ulhaq, S. Weiler, C. Roy, S. M. Ulrich, M. Jetter, S. Hughes, and P. Michler, “Detuning-dependent Mollow triplet of a coherently-driven single quantum dot,” *Optics Express* **21**, 4382 (2013).

Bibliography

- [207] F. Liu, L. M. P. Martins, A. J. Brash, A. M. Barth, J. H. Quilter, V. M. Axt, M. S. Skolnick, and A. M. Fox, "Ultrafast depopulation of a quantum dot by LA-phonon-assisted stimulated emission," *Physical Review B* **93**, 161407 (2016).
- [208] A. J. Brash, L. M. P. P. Martins, A. M. Barth, F. Liu, J. H. Quilter, M. Glässl, V. M. Axt, A. J. Ramsay, M. S. Skolnick, and A. M. Fox, "Dynamic vibronic coupling in InGaAs quantum dots [Invited]," *Journal of the Optical Society of America B: Optical Physics* **33**, C115–C122 (2016).
- [209] H. C. Casey, D. D. Sell, and K. W. Wecht, "Concentration dependence of the absorption coefficient for n- and p-type GaAs between 1.3 and 1.6 eV," *Journal of Applied Physics* **46**, 250–257 (1975).
- [210] A. Aspuru-Guzik and P. Walther, "Photonic quantum simulators," *Nature Physics* **8**, 285–291 (2012).
- [211] M. Varnava, D. E. Browne, and T. Rudolph, "How Good Must Single Photon Sources and Detectors Be for Efficient Linear Optical Quantum Computation?" *Physical Review Letters* **100**, 060502 (2008).
- [212] H.-J. Briegel, W. Dür, J. I. Cirac, and P. Zoller, "Quantum repeaters: The role of imperfect local operations in quantum communication," *Physical Review Letters* **81**, 5932–5935 (1998).
- [213] E. Schöll, L. Hanschke, L. Schweickert, K. D. Zeuner, M. Reindl, S. F. Covre da Silva, T. Lettner, R. Trotta, J. J. Finley, K. Müller, A. Rastelli, V. Zwiller, and K. D. Jöns, "Resonance Fluorescence of GaAs Quantum Dots with Near-Unity Photon Indistinguishability," *Nano Letters* **19**, 2404–2410 (2019).
- [214] G. Kiršanskė, H. Thyrrerstrup, R. S. Daveau, C. L. Dreeßen, T. Pregnolato, L. Midolo, P. Tighineanu, A. Javadi, S. Stobbe, R. Schott, A. Ludwig, A. D. Wieck, S. I. Park, J. D. Song, A. V. Kuhlmann, I. Söllner, M. C. Löbl, R. J. Warburton, and P. Lodahl, "Indistinguishable and efficient single photons from a quantum dot in a planar nanobeam waveguide," *Physical Review B* **96**, 165306 (2017).

- [215] L. Dusanowski, S.-H. Kwon, C. Schneider, and S. Höfling, “Near-Unity Indistinguishability Single Photon Source for Large-Scale Integrated Quantum Optics,” *Physical Review Letters* **122**, 173602 (2019).
- [216] J. C. L. Carreño, E. Z. Casalengua, F. P. Laussy, and E. del Valle, “Joint subnatural-linewidth and single-photon emission from resonance fluorescence,” *Quantum Science and Technology* **3**, 045001 (2018).
- [217] E. Zubizarreta Casalengua, J. López Carreño, F. Laussy, and E. del Valle, “Conventional and unconventional photon statistics,” arXiv e-prints p. arXiv:1901.09030 (2019).
- [218] A. Gonzalez-Tudela, F. P. Laussy, C. Tejedor, M. J. Hartmann, and E. del Valle, “Two-photon spectra of quantum emitters,” *New Journal of Physics* **15**, 033036 (2013).
- [219] W. Heitler, *The Quantum Theory of Radiation* (Oxford University Press, Oxford, 1954).
- [220] E. del Valle, A. Gonzalez-Tudela, F. P. Laussy, C. Tejedor, and M. J. Hartmann, “Theory of Frequency-Filtered and Time-Resolved N -Photon Correlations,” *Physical Review Letters* **109**, 183601 (2012).
- [221] C. L. Phillips, A. J. Brash, D. P. S. McCutcheon, J. Iles-Smith, E. Clarke, B. Royall, M. S. Skolnick, A. M. Fox, and A. Nazir, “Photon Statistics of Filtered Resonance Fluorescence,” *Physical Review Letters* **125**, 043603 (2020).
- [222] E. del Valle, A. Gonzalez-Tudela, F. P. Laussy, C. Tejedor, and M. J. Hartmann, “Erratum: Theory of frequency-filtered and time-resolved n -photon correlations [phys. rev. lett. 109, 183601 (2012)],” *Physical Review Letters* **116**, 249902 (2016).
- [223] Dalibard, J. and Reynaud, S., “Correlation signals in resonance fluorescence :

Bibliography

- interpretation via photon scattering amplitudes,” *Journal de Physique. France* **44**, 1337–1343 (1983).
- [224] W. Heisenberg, “Über den anschaulichen Inhalt der quantentheoretischen Kinematik und Mechanik,” *Zeitschrift für Physik* **43**, 172–198 (1927).
- [225] D. P. S. McCutcheon and A. Nazir, “Model of the Optical Emission of a Driven Semiconductor Quantum Dot: Phonon-Enhanced Coherent Scattering and Off-Resonant Sideband Narrowing,” *Physical Review Letters* **110**, 217401 (2013).
- [226] C. A. Schrama, G. Nienhuis, H. A. Dijkerman, C. Steijsiger, and H. G. M. Heide-
deman, “Intensity correlations between the components of the resonance fluo-
rescence triplet,” *Physical Review A* **45**, 8045–8055 (1992).
- [227] A. Ulhaq, S. Weiler, S. M. Ulrich, R. Roßbach, M. Jetter, and P. Michler, “Cas-
caded single-photon emission from the Mollow triplet sidebands of a quantum
dot,” *Nature Photonics* **6**, 238–242 (2012).
- [228] S. Weiler, D. Stojanovic, S. M. Ulrich, M. Jetter, and P. Michler, “Postselected
indistinguishable single-photon emission from the Mollow triplet sidebands of
a resonantly excited quantum dot,” *Physical Review B* **87**, 241302 (2013).
- [229] C. A. Schrama, G. Nienhuis, H. A. Dijkerman, C. Steijsiger, and H. G. M. Heide-
deman, “Destructive interference between opposite time orders of photon emis-
sion,” *Physical Review Letters* **67**, 2443–2445 (1991).
- [230] A. Aspect, G. Roger, S. Reynaud, J. Dalibard, and C. Cohen-Tannoudji,
“Time Correlations between the Two Sidebands of the Resonance Fluorescence
Triplet,” *Physical Review Letters* **45**, 617–620 (1980).
- [231] M. Peiris, B. Petrak, K. Konthasinghe, Y. Yu, Z. C. Niu, and A. Muller, “Two-
color photon correlations of the light scattered by a quantum dot,” *Physical
Review B* **91** (2015).

- [232] Y. Nieves and A. Muller, “Third-order frequency-resolved photon correlations in resonance fluorescence,” *Physical Review B* **98**, 165432 (2018).
- [233] J. A. Armstrong, “Theory of Interferometric Analysis of Laser Phase Noise*,” *Journal of the Optical Society of America* **56**, 1024–1031 (1966).
- [234] L. Knöll, W. Vogel, and D.-G. Welsch, “Quantum noise in spectral filtering of light,” *Journal of the Optical Society of America B: Optical Physics* **3**, 1315–1318 (1986).
- [235] R. C. Neelen, D. M. Boersma, M. P. van Exter, G. Nienhuis, and J. P. Woerdman, “Spectral filtering within the Schawlow-Townes linewidth as a diagnostic tool for studying laser phase noise,” *Optics Communications* **100**, 289–302 (1993).
- [236] M. Fox, *Optical Properties of Solids* (Oxford University Press, Oxford, 2013), 2nd ed.
- [237] O. Martinez, “Design of high-power ultrashort pulse amplifiers by expansion and recompression,” *IEEE Journal of Quantum Electronics* **23**, 1385–1387 (1987).
- [238] A. Kiraz, M. Atatüre, and A. Imamoglu, “Quantum-dot single-photon sources: Prospects for applications in linear optics quantum-information processing,” *Physical Review A* **69**, 032305 (2004).
- [239] I. J. Luxmoore, E. D. Ahmadi, A. M. Fox, M. Hugues, and M. S. Skolnick, “Unpolarized H1 photonic crystal nanocavities fabricated by stretched lattice design,” *Applied Physics Letters* **98**, 041101 (2011).
- [240] M. Minkov and V. Savona, “Automated optimization of photonic crystal slab cavities,” *Scientific Reports* **4** (2014).
- [241] L. Hanschke, L. Schweickert, J. C. L. Carreño, E. Schöll, K. D. Zeuner, T. Lettner, E. Z. Casalengua, M. Reindl, S. F. C. da Silva, R. Trotta, J. J. Finley, A. Rastelli,

Bibliography

- E. del Valle, F. P. Laussy, V. Zwiller, K. Müller, and K. D. Jöns, “Origin of Antibunching in Resonance Fluorescence,” *Physical Review Letters* **125**, 170402 (2020).
- [242] M. Anderson, T. Müller, J. Huwer, J. Skiba-Szymanska, A. B. Krysa, R. M. Stevenson, J. Heffernan, D. A. Ritchie, and A. J. Shields, “Quantum teleportation using highly coherent emission from telecom c-band quantum dots,” *npj Quantum Information* **6** (2020).
- [243] T. Miya, Y. Terunuma, T. Hosaka, and T. Miyashita, “Ultimate low-loss single-mode fibre at 1.55 μm ,” *Electronics Letters* **15**, 106–108(2) (1979).
- [244] W. A. Gambling, “The rise and rise of optical fibers,” *IEEE Journal of Selected Topics in Quantum Electronics* **6**, 1084–1093 (2000).
- [245] S.-K. Liao, H.-L. Yong, C. Liu, G.-L. Shentu, D.-D. Li, J. Lin, H. Dai, S.-Q. Zhao, B. Li, J.-Y. Guan, W. Chen, Y.-H. Gong, Y. Li, Z.-H. Lin, G.-S. Pan, J. S. Pelc, M. M. Fejer, W.-Z. Zhang, W.-Y. Liu, J. Yin, J.-G. Ren, X.-B. Wang, Q. Zhang, C.-Z. Peng, and J.-W. Pan, “Long-distance free-space quantum key distribution in daylight towards inter-satellite communication,” *Nature Photonics* **11**, 509–513 (2017).
- [246] T. Müller, J. Skiba-Szymanska, A. B. Krysa, J. Huwer, M. Felle, M. Anderson, R. M. Stevenson, J. Heffernan, D. A. Ritchie, and A. J. Shields, “A quantum light-emitting diode for the standard telecom window around 1,550 nm,” *Nature Communications* **9** (2018).
- [247] M. Benyoucef, M. Yacob, J. P. Reithmaier, J. Kettler, and P. Michler, “Telecom-wavelength (1.5 μm) single-photon emission from InP-based quantum dots,” *Applied Physics Letters* **103**, 162101 (2013).
- [248] M. Paul, F. Olbrich, J. Höschel, S. Schreier, J. Kettler, S. L. Portalupi, M. Jetter, and P. Michler, “Single-photon emission at 1.55 μm from MOVPE-grown

- InAs quantum dots on InGaAs/GaAs metamorphic buffers," *Applied Physics Letters* **111**, 033102 (2017).
- [249] C. Nawrath, F. Olbrich, M. Paul, S. L. Portalupi, M. Jetter, and P. Michler, "Coherence and indistinguishability of highly pure single photons from non-resonantly and resonantly excited telecom c-band quantum dots," *Applied Physics Letters* **115**, 023103 (2019).
- [250] A. Kors, K. Fuchs, M. Yacob, J. P. Reithmaier, and M. Benyoucef, "Telecom wavelength emitting single quantum dots coupled to InP-based photonic crystal microcavities," *Applied Physics Letters* **110**, 031101 (2017).
- [251] K. Tiurev, M. H. Appel, P. L. Mirambell, M. B. Lauritzen, A. Tiranov, P. Lodahl, and A. S. Sørensen, "High-fidelity multi-photon-entangled cluster state with solid-state quantum emitters in photonic nanostructures," arXiv e-prints p. arXiv:2007.09295 (2020).
- [252] J. P. Lee, B. Villa, A. J. Bennett, R. M. Stevenson, D. J. P. Ellis, I. Farrer, D. A. Ritchie, and A. J. Shields, "A quantum dot as a source of time-bin entangled multi-photon states," *Quantum Science and Technology* **4**, 025011 (2019).